

NORTHWESTERN UNIVERSITY

Probing the Hydrogen-Bonding Network at Soft Matter and  
Metal:Metal:Oxide:Water Interfaces

A DISSERTATION

SUBMITTED TO THE GRADUATE SCHOOL  
IN PARTIAL FULFILLMENT OF THE REQUIREMENTS

for the degree

DOCTOR OF PHILOSOPHY

Field of Chemistry

By

Naomi Dalchand

EVANSTON, ILLINOIS

September 2021

© Copyright by Naomi Dalchand 2021

All Rights Reserved

## Abstract

Probing the Hydrogen-Bonding Network at Soft Matter and  
Metal:Metal:Oxide:Water Interfaces

Naomi Dalchand

The ubiquitous role of water in biochemical, electrochemical, and geochemical systems has driven scientific interest in studying the fundamental hydrogen-bonding interactions that water molecules exhibit in the presence of different materials. Specifically, we focus on the interactions characterizing water at the interface between two bulk media, as these are essential to numerous chemical processes, including protein folding, corrosion, dissolution, and mineralization. To this end, this thesis seeks to provide insight on the structure of interfacial water molecules at the surface of both biological and inorganic materials using a surface-selective technique called vibrational sum frequency generation (SFG) spectroscopy.

To study the nature of water at biological interfaces, the polycation, poly(allylamine hydrochloride) (PAH), is introduced to an idealized model of cell membranes known as supported lipid bilayers (SLBs). Perturbations to the interfacial water structure are assessed as a function of polycation concentration and lipid headgroup charge. The experimental results from this study are discussed in detail and placed within a much larger analysis that includes work that has been previously done in our group studying the electrostatics, thermodynamics, and molecular structure at the polycation:lipid membrane interface.

To obtain insight into the structure of water at inorganic interfaces, the hydrogen-bonding network of interfacial water molecules is probed at the Ni:NiOx:water interface

using SFG spectroscopy. Interpretation of the SFG signals at this interface is made notoriously difficult due to the overwhelming presence of spectral artifacts arising from Fresnel factors. This thesis includes a detailed discussion of the efforts made to overcome this challenge, including the optimal nickel film thickness, and it also discusses how hydrogen-bonding changes with pH and ionic strength. Lastly, this thesis discusses preliminary and future experiments directed towards studying the nanolayer nickel film surface at a high relative humidity to elucidate surface hydroxyl groups.

Despite their apparent differences, both studies outlined in this thesis resulted in one main takeaway: hydrogen-bonding of water molecules at the interface is complex, however, fundamental studies such as those carried out here are necessary to begin understanding the mechanisms associated with the function of new or existing materials.

## Acknowledgements

Five years ago, I embarked on a journey with one goal in mind: to become the best scientist I could be. During this time, I have been lucky enough to meet some inspiring individuals that have not only helped me achieve this goal but have also helped me discover the best version of myself. First and foremost, I would like to thank my advisor, Prof. Franz M. Geiger, for his continued support throughout this journey. Although he was on sabbatical my first year, he made every effort during that year (and subsequent years) to support my scientific interests and long-term careers goals, even from the first day I met him and for that, I am extremely thankful. I would also like to thank my past and present committee members, Prof. Teri Odom, Prof. Will Dichtel, Prof. George Schatz, and Prof. Toru Shiozaki, for stimulating productive scientific conversations throughout every checkpoint of my graduate school career.

I have also been extremely lucky to have worked with a group that continually aims to have challenging and interesting discussions in and out of the lab. To my mentors, Dr. Alicia C. McGeachy and Dr. Merve Doğangün, you have both been instrumental in my development as a scientist in graduate school. Thank you both for your patience with me in the lab and your friendship outside of it. I would also like to thank the other past and present members of the group, Ariana, Paul, Mavis, Tian, Laura, Dawning, Johnny, HanByul, Emily, Emilie, Aleia, Jana, Rico, Cat, and Catherine. Dawning, I could not have imagined anyone better to have gone through graduate school with. Thank you for being there and motivating me every step of the way. Rico, I've learned so much from you in these past two years and I can't wait to see what you do next. Can't wait to visit you in Shanghai. Ariana, I've missed going to Starbucks with you every day, but I'm happy

I get to see you from time to time when we video chat. Johnny, thank you for the coffee walks, life chats, and music recs. And Emily, thank you for having such open and difficult conversations with me. I will miss them so much.

During the first half of my graduate school career, I met many outstanding scientists through my involvement with the Center for Sustainable Nanotechnology (CSN). I would like to thank all the students and PIs I interfaced with as part of the CSN for their scientific insight and feedback. I especially want to thank Dr. Schwartz and Dr. Krause for their support in developing webinars and blog posts for the professional development of the students therein. At Northwestern, I have also been lucky enough to have been involved with Northwestern University Building on Diversity (NU BonD) and the Center for the Integration of Research, Teaching, and Learning (CIRTL). I would like to thank all the members of NU BonD, past and present, for creating a space where we could talk about the issues of diversity within STEM as we worked to develop a more inclusive environment in our own department. Thank you to Ollie, Ariana, Andrea, Nic, Zack, Jeremy, Aidan, Waleed, Qining, Emily, and Cat for having these discussions. Throughout my involvement with CIRTL, I was lucky enough to have continuous feedback on my teaching practices from Dr. Lauren Woods. I am thankful for all of her advice. I would also like to thank Dr. Stephanie Knezz for allowing me to implement my STAR project in her class during such an unprecedented time.

My interest in scientific research would not have been possible without my undergraduate research advisors from Barnard, Prof. Marisa C. Buzzeo and Prof. John S. Magyar. Prof. Magyar, your last lecture in my first year general chemistry course that focused on your research is something I will never forget. It made me realize I wanted to be in the

lab. Prof. Buzzeo, you are who I aspire to be as a scientist. Thank you for helping me make the decision to come to Northwestern.

Lastly, I would like to thank my friends and family for their support throughout this journey. To the members of my cohort, Justin, Nate, Dawning, Elamar, Riki, Sarah, Henrique, Shawn, Austin, Matt, Jake, Nic, Ollie, and Daylan, thank you for all the good times and memories we made outside of the lab. To my amazing friends, Xinni, Sadia, Doris, and Vivian, thank you so much for all the Facetimes, the visits to Chicago, and the hangouts when I'm home. I've missed you all so much and words can't describe how happy I am to be coming back to see you all more frequently. To Mouri and Gurvir, thank you for every phone call, every text. Your advice has helped me throughout some of the most difficult times of graduate school. To Gissel, Edra, Isabelle, Nadia, Alexandria, and Karen, thank you for all the laughs and good times. You all hold a special place in my heart.

To my family, leaving home has always made me think of that one Winnie the Pooh quote,

*"How lucky I am to have something that makes saying goodbye so hard."*

Leaving was the hardest decision I have ever made. I've missed you all too much. To Sam, Tina, and my soon to be brother-in-law James, I don't think there are enough words to describe the amount of support you've provided me with during my time at Northwestern. Thank you for all the laughs, the random texts and videos, the fun conversations, and the life advice. To my parents, thank you so much for supporting my dreams. You have both worked so hard to give my sisters and I the world, and I am grateful for every little thing you have provided us with. To Karthik, I don't know where to begin. Thank

you for singing along to every song with me, especially the Soca ones (we can't forget Kes now). If all I did for the rest of my life was drink wine and listen to music with you, I'd still be the happiest person on this planet. There's no one else I'd want to share my culture and my life with.



*To my parents and my sisters.*

## Table of Contents

|  |    |
|--|----|
| Abstract   | 3  |
| Acknowledgements   | 5  |
| List of Figures  | 14 |
| Chapter 1. Introduction: Chemistry of Aqueous Interfaces                               | 24 |
| 1.1. Basics of Aqueous Interfaces  | 24 |
| 1.2. Assessing Interfacial Water Structure: The Nano-Bio Interface                     | 26 |
| 1.3. Assessing Interfacial Water Structure: The Metal:Metal:Oxide-Aqueous<br>Interface | 28 |
| 1.4. Scope and Organization of Thesis  | 30 |
| Chapter 2. Nonlinear Optics and Sum Frequency Generation Spectroscopy                  | 32 |
| 2.1. Introduction to Vibrational Sum Frequency Generation (SFG) Spectroscopy           | 32 |
| 2.2. Nonlinear Optics and Sum Frequency Generation (SFG) Theory                        | 35 |
| 2.3. Fresnel Factors   | 37 |
| 2.4. Sum Frequency Generation (SFG) Set-Up   | 42 |
| 2.5. Optical Window Preparation  | 46 |
| 2.6. Summary   | 46 |

|  |    |
|--|----|
| Chapter 3. Perturbation of Hydrogen-Bonding Networks Over Supported Lipid Bilayers by Poly (allylamine hydrochloride)                              | 47 |
| 3.1. Introduction  | 48 |
| 3.2. Methods   | 52 |
| 3.3. Results and Discussion  | 57 |
| 3.4. Conclusion  | 66 |
| Chapter 4. Summary and Future Work: Electrostatics, Hydrogen-Bonding, and Molecular Structure at Polycation and Peptide: Lipid Membrane Interfaces | 68 |
| 4.1. Introduction to Chapter 4   | 69 |
| 4.2. Background  | 69 |
| 4.3. The Optical Voltmeter   | 73 |
| 4.4. Atomistic and Coarse-Grained simulations  | 75 |
| 4.5. Sub-Charging at High Surface Densities of Polycations   | 76 |
| 4.6. Contact-Ion Pair Formation  | 81 |
| 4.7. Perturbation of the Hydrogen-Bonding Network with Added Polycations   | 83 |
| 4.8. Cationic Polymers at Lipid Bilayer Surfaces   | 85 |
| 4.9. Polycations Bind to Bilayers with Comparable $\Delta G_{\text{ads}}$  | 90 |
| 4.10. Conclusion and Outlook   | 94 |
| 4.11. Future Work: Gramicidin A (gA) containing Supported Lipid Bilayers (SLBs)  | 96 |

|   |     |
|---|-----|
|   | 12  |
| Chapter 5. Beyond Fresnel Factors: Probing the Interfacial Water Structure at<br>Nickel:Nickel:Oxide:Water Interfaces with Sum Frequency Generation<br>(SFG) Spectroscopy | 98  |
| 5.1. Introduction   | 99  |
| 5.2. Methods  | 102 |
| 5.3. Results and Discussion   | 107 |
| 5.4. Conclusion   | 122 |
| Chapter 6. Summary and Future Work: Investigating the Presence of Surface<br>Hydroxyl Groups on the Nickel Surface  | 124 |
| 6.1. Introduction to Chapter 6  | 124 |
| 6.2. Background   | 124 |
| 6.3. Methods  | 125 |
| 6.4. Preliminary Results and Discussion   | 133 |
| 6.5. Conclusions and Future Work  | 138 |
| REFERENCES  | 139 |
| References for Chapter 1  | 139 |
| References for Chapter 2  | 149 |
| References for Chapter 3  | 156 |
| References for Chapter 4  | 164 |
| References for Chapter 5  | 174 |
| References for Chapter 6  | 179 |
| Appendix A. Fresnel Coefficients for a Single Interface   | 183 |

|   |     |
|---|-----|
|   | 13  |
| A.1. Fresnel coefficients for <i>s</i> -polarization        | 186 |
| A.2. Fresnel coefficients for <i>p</i> -polarization        | 188 |
| A.3. Fresnel Local Field Factors                            | 190 |
| Appendix B. Original Research Proposal                      | 192 |
| B.1. Introduction, Background, and Significance of Research | 193 |
| B.2. Scientific Objectives                                  | 195 |
| B.3. Previous Work  | 195 |
| B.4. Proposed Research                                      | 197 |
| B.5. ATP Quantification                                     | 202 |
| B.6. Complementary Solvation Environment Studies            | 203 |
| B.7. Summary and Conclusion                                 | 206 |
| References for Appendix A                                   | 207 |
| References for Appendix B                                   | 208 |
| Curriculum Vitae  | 214 |

## List of Figures

|     |   |    |
|-----|---|----|
| 2.1 | Introduction to SFG   | 34 |
| 2.2 | The reflection and transmission contributions from interface I and II used in the calculation of $L_{xx}$ . Figure adapted from ref. [41]   | 41 |
| 2.3 | A detailed schematic of the sum frequency generation set-up used in both Chapters 3 and 5.  | 44 |
| 2.4 | A control experiment where the polarizer was rotated every $15^\circ$ and the power (green) and sum frequency intensity (purple) on gold was recorded   | 45 |
| 3.1 | The structure of (A) cationic polymer, poly (allylamine) hydrochloride (PAH, blue), (B) zwitterionic lipid, 1,2-dimyristoyl-sn-glycero-3-phosphocholine (DMPC, green), (C) negatively charged lipid, 1,2-dimyristoyl-sn-glycero-3-phospho-(1-rac-glycerol) (DMPG, orange), and (D) negatively charged lipid. 1,2-dimyristoyl-sn-glycero-3-phospho-L-serine (DMPS, red). | 51 |
| 3.2 | A comparison of gold on two substrates. The above plot shows the gold profile for the sum of DFG's taken for a gold $\text{CaF}_2$ substrate (red) and a gold 25 nm ALD $\text{SiO}_2$ coated $\text{CaF}_2$ window (blue).   | 55 |

- 3.3 The home-built teflon flow-cell used to prepare supported lipid bilayers (SLBs). The same flow-cell was then used to monitor the interaction of the SLBs with poly (allylamine hydrochloride) (PAH). 56
- 3.4 Representative SSP-polarized SFG spectra for a bilayer formed from (A) a 9:1 mixture of DMPC:DMPG lipids (orange) and (B) a 9:1 mixture of DMPC:DMPS lipids (red) in buffer solution composed of 0.01 M Tris and 0.1 M NaCl, adjusted to pH 7.4 before interaction with PAH and after the interaction of the SLB with PAH in increasing concentrations: 1  $\mu\text{M}$  (light blue), 10  $\mu\text{M}$  (blue), and 0.1 mM (dark blue). All spectra in (B) have been binned over three points in  $x$  and  $y$  between  $3,000\text{ cm}^{-1}$  —  $3,600\text{ cm}^{-1}$  for clearer S/N resolution. 59
- 3.5 SSP-polarized SFG spectra for (A) major and (B) minor responses for the interaction of PAH with a bilayer formed from 100% DMPC lipids in buffer solution composed of 0.01 M Tris and 0.1 M NaCl, adjusted to pH 7.4 before interaction with PAH (green). The spectra taken after the interaction of the SLB with PAH in increasing concentrations: 1  $\mu\text{M}$  (light blue), 10  $\mu\text{M}$  (blue), 0.1 mM (dark blue), and 1 mM (navy). The spectra for (B) have been binned over three points in  $x$  and  $y$  between  $3,000\text{ cm}^{-1}$  —  $3,600\text{ cm}^{-1}$  for clearer S/N resolution and comparison with the major response. 62
- 3.6 Interaction of a bilayer formed from (A) a 9:1 mixture of DMPC:DMPG lipids (orange) and (B) a 9:1 mixture of DMPC:DMPS lipids (red) with the highest concentration of PAH studied, 0.1 mM (dark blue),

and after rinsing with 20 mL of PAH-free buffer solution (dotted blue line). The spectra for (B) have been binned over three points in  $x$  and  $y$  between  $3,000\text{ cm}^{-1}$  --  $3,600\text{ cm}^{-1}$  for clearer S/N resolution and comparison with other reversibility traces. (C) Interaction of a bilayer formed from 100% DMPC lipids (green) with the highest concentration of PAH studied, 1 mM (navy), and after rinsing with 20 mL of PAH-free buffer solution (dotted blue line). (D) A bilayer formed from 100% DMPC lipids (green) after rinsing with buffer solution composed of 0.01 M Tris and 0.3 M NaCl, adjusted to pH 7.4. 65

4.1 A compilation of the structures of the polycations used in our work: (A) poly(allylamine hydrochloride) (PAH), (B) poly(vinylamine hydrochloride) (PVAm), (C) poly(diallyldimethylammonium chloride) (PDADMAC), (D) poly-L-lysine (PLL), and (E) poly-L-arginine (PLR). The molecular weight of each polycation used is listed under the corresponding structure. The peptides surveyed, Lys<sub>8</sub> and Arg<sub>8</sub>, have the same functional groups as their polycation counterparts in (D) and (E) respectively. 72

4.2 SHG adsorption isotherms for (A) PAH (●) at 0.1 M NaCl and (B) AH (○) at 0.1 M NaCl. (B) also shows PAH (■) and AH (□) at low ionic strength conditions, 0 M NaCl. All solutions were prepared to produce a buffer solution containing 0.01 M Tris at a pH 7.4. The black lines in (A) and (B) represent the data that was fit to the double



layer model. Reprinted with permission from ref 50. Copyright 2017 ACS Publications.

79

4.3 The top (A) and side view (B) of the surface-packing model for PAH<sub>10</sub> at the lipid bilayer surface. Here, only one AH monomer is in direct contact with the surface. The following MCCE calculations in (C) show a computed titration curve for different surface binding densities, where there is a notable decrease in protonated surface sites as more PAH<sub>10</sub> is added on the bilayer surface. Reprinted with permission from ref 50. Copyright 2017 ACS Publications.

80

4.4 Atomistic simulation of AH monomers (320) interacting with a bilayer formed from a 9:1 mixture of DMPC: DMPG lipids. (A) Significant undulation to the molecular surface of the bilayer (gray) is shown upon AH (blue) binding. The phosphate moieties of the lipid head groups are also shown (red) to highlight where bonding is taking place. (B) shows a 90° rotation of (A) about the *z*-axis and (C) presents an atomistic view of (A). (D) represents the hydrogen-bonding interactions (green dotted lines) between an AH monomer with the negatively charged portions of adjacent lipids, the phosphate and glycerol groups. Adapted with permission from ref 50. Copyright 2017 ACS Publications.

82

4.5 The MD simulations show the interaction of Arg<sub>8</sub> (left column) and Lys<sub>8</sub> (right column) with a bilayer formed from a 9:1 mixture of DMPC: DMPG lipids. In the top two panels, the difference in

preferred binding between the peptides is seen. Arg<sub>8</sub> prefers to interact with the bilayer, interacting with up to 6 side chains. Lys<sub>8</sub> prefers interacting with the solution, adopting a “stand-up” conformation and interacting with the bilayer with only 1 or 2 side chains. The lower panels show a close up view of the side chains interacting with the phosphate moieties on the lipid headgroup, with Lys<sub>8</sub> interacting with less phosphate moieties than Arg<sub>8</sub>. Reproduced from ref. 34 with permission from the Royal Society of Chemistry (RSC). 88

- 4.6 Integrated charge density (total, right, and from different components, left),  $\sigma(z)$ , as a function of  $z$  from MD simulations for Arg<sub>8</sub> on a 9:1 DMPC:DMPG bilayer 89
- 4.7 Normalized SHG E-field as a function of positive charge for PDADMAC<sub>400</sub>, PDADMAC<sub>100</sub>, PLL, PLR, and PVAm. The concentration of positive charge was determined by multiplying the number of repeat units of each respective polycation by the concentration of the polycation added to the 9:1 DMPC: DMPG bilayer. Adapted from ref. 64 by permission of the Royal Society of Chemistry (RSC) from the PCCP Owner Societies. 92
- 4.8 Reversibility of adsorption of 50 nM PDADMAC<sub>400</sub> (dark purple), 50 nM PDADMAC<sub>100</sub> (light purple), 500 nM PLL (green), 500 nM PLR (red), and 50 nM PVAm (teal) to a bilayer formed from a 9:1 mixture of DMPC: DMPG lipids. The chosen concentrations represent high surface coverage as determined from their respective adsorption

isotherms. At  $t = 43$  min, the polycation solutions are introduced to the bilayer and left to equilibrate until  $t = 112$  min, where the bilayer is then rinsed with polycation-free buffer solution (10 mM Tris, 100 mM NaCl, at pH 7.4). Adapted from ref. 64 by permission of the Royal Society of Chemistry (RSC) from the PCCP Owner Societies. 93

5.1 Side view (left) of the experimental geometry and a zoom-in (right) on the 3-layered  $\text{CaF}_2$ /nickel:water interface. Dark blue and dark grey represent the water layer and the metal:metal:oxide layer. 105

5.2 Contact angles increase substantially over time for 5 nm nickel films (green) when compared to plain glass slides (black) left out in ambient laboratory air (a) due to the presence of hydrocarbons. (b) SFG spectroscopy is sensitive enough to detect the presence of hydrocarbons in the span of 24 hours. 111

5.3 The uniformity of the  $\sim 5$  nm nickel film is shown in (a) from an SEM image where the field of view is the approximately the same as the visible beam diameter. IR absorbance of films with thicknesses between  $\sim 2$ – $5$  nanometers was taken using FTIR. The absorbance is shown to be highest for films  $\sim 5$  nm at  $\sim 60\%$  (b). Due to the thin nature of the films, it is possible the  $\text{CaF}_2$  substrate may interfere with the response from the nickel:nickel:oxide:water interface. XPS reveals metal-fluorine bonds at the sample surface (c). However, SFG spectroscopy of plain  $\text{CaF}_2$  at two different values of pH does not

result in any signal. Therefore, it is likely the SFG response we collect is not from the CaF<sub>2</sub>-water interface. 112

5.4 Corresponding FTIR (recorded in % transmission), Ellipsometry, and SFG spectra for films of different thicknesses. The thickest film is shown in purple with the lowest % IR transmitted. The thinnest film is shown in green and corresponds to the highest % transmittance of the films shown in this data set. 113

5.5 Calculations of the spectral coefficients represented by Equations 5.2.2–5.2.5 are shown with comparison to experimental results for the interaction of water with a Ni:NiOx film. Interface I is denoted by the dashed lines in each respective plot. Interface II is shown by the solid ( $\chi_{\text{water}}^{(2)} > \chi_{\text{Ni}}^{(2)}$ ) and dotted ( $\chi_{\text{Ni}}^{(2)} > \chi_{\text{water}}^{(2)}$ ) lines. The representative experimental SFG spectrum here (grey) is taken in PPP-polarization. 117

5.6 The subsurface XPS data reveals differences in a nickel film (a) that has been prepared more recently and exposed to less salt water than a film in (b). SFG spectra are binned during the acquisitions and taken in PPP-polarization. Films exposed to water and subsequently 100 mM NaCl at pH 5.8 and 8.5 are shown for a new film (c and e respectively) and an older film that has been introduced to salt several times (d and f respectively). 121

6.1 The ~10 nm nickel films burn when exposed to high IR powers and tight visible focus as was mentioned for the ~5 nm films in Chapter

5. The line between spots shows burning from simply moving the film from one spot to another using the sample stage. 128
- 6.2 The red dot shown here represents the loosely focused visible beam with a diameter  $\sim 4$  mm. The small transparent white circles represent the IR beam moving across the spot from one edge to the other (from 1 to 5). The spectra taken in the C–H stretching region (1 DFG position) with PPP-polarization corresponds to each respective overlap position and is labeled for each position. 129
- 6.3 A control experiment in which the visible power is tuned to determine whether spectra taken at intermediate ( $1 \mu\text{J}$ ) and low ( $0.5 \mu\text{J}$ ) visible powers resolve all spectral features from the case of high ( $2 \mu\text{J}$ ) visible power. 130
- 6.4 The above diagram details the flow-cell set-up used in the relative humidity experiments presented in this chapter. A helium tank is connected to allow the flow of helium through a dry (left) and wet (right) path. The flow rates are controlled with mass flow controllers (MFCs). Water vapor (or dry helium) enters the sample cell through one piece of tubing and exits through another. The RH sensor measures the RH of the sample chamber in real time and is sealed tightly. The sample sits in the cell in external geometry for the SFG experiments. 132
- 6.5 Representative Raman spectra of a  $\sim 10$  nm nickel film in the regions of interest for (a) nickel oxide and (b) nickel hydroxides. 135

- 6.6 Representative SFG spectra of a 10 nm nickel film (on  $\text{CaF}_2$ ) taken in PPP-polarization at three different spots (a). The spots are averaged and shown by the black trace in (a). It is enlarged in (b) to showcase the 3 possible surface hydroxyl groups denoted by the blue dotted lines. 136
- 6.7 Representative relative humidity experiments conducted in (a) PPP- and (b) SSP-polarization. 137
- A.1 Diagrams showing the geometries of light scattering off of an interface for (a) *s*- and (b) *p*-polarized light. In both diagrams, the blue represents the electric field and the red denotes the magnetic field. The cross-hatched circle represents a field vector pointing into the page in the  $-y$ -direction. 185
- B.1 **The effects of C-peptide on circulation.** C-peptide can increase eNOS activity and therefore, increase the production of NO by stimulating  $\text{Ca}^{2+}$  uptake by endothelial cells (cells that line the blood vessels). In erythrocytes, C-peptide can also increase glucose uptake, resulting in increased ATP production and therefore, also increase the production of NO. Lastly, C-peptide has been shown to stimulate  $\text{Na}^+$ ,  $\text{K}^+$ -ATPase activity.<sup>8</sup> 193
- B.2 **Peptide structure.** The primary structure of C-peptide is shown in (a), where the acidic residues E1, E3, D4, E11, and E27 are

highlighted in yellow. The structure of E and D amino acids are presented in (b). 197

B.3 **Detailed schematic of the HSA protein.** The 6 subdomains are shown above in different colors: Ia (yellow), Ib (green), IIa (red), IIb (pink), IIIa (blue), and IIIb (cyan).<sup>20</sup> 198

B.4 CD spectra of (1) HSA ( $0.75 \times 10^{-6}$  M) (2) kaempferol-HSA with a drug/protein (d/p) ratio of 1 (3) d/p ratio of 3 (4) d/p ratio of 6 and (5) kaempferol ( $3.3 \times 10^{-6}$  M). These experiments were conducted at a pH of 7.4.<sup>31</sup> 202

B.5 The above figure shows the 2D-IR spectra of the K38Aha labeled PDZ2 domain (a) without ligand binding, (b) with binding to peptide RWAKSEAKENEQVSAV, and (c) with binding to the peptide mentioned in (b) mutated with an apolar azobenzene moiety.<sup>38</sup> 205

## CHAPTER 1

**Introduction: Chemistry of Aqueous Interfaces****1.1. Basics of Aqueous Interfaces**

The universal presence of water and its unique properties make it a substance that has attracted a vast amount of interest from the scientific community for many decades.<sup>1,2</sup> Specifically, the fascinating properties of water molecules that exist at an interface, a region where two immiscible bulk phases come into contact, has accounted for insight into numerous fields such as geochemistry,<sup>3-5</sup> atmospheric chemistry,<sup>6,7</sup> environmental science,<sup>8-10</sup> electrochemistry,<sup>11-14</sup> and biochemistry<sup>15-17</sup> to name a few. Descriptions of studies focused on the relevance of interfacial water molecules as it relates to biological and energy producing materials are provided in Sections 1.2 and 1.3.

At the macroscopic level, the differences in the properties of water molecules that exist at the interface versus those within the bulk are apparent even in everyday life, for instance, upon inspecting the air-water interface<sup>18</sup> in a glass of water. Water molecules that compose the bulk deep within the glass are largely only subjected to forces from neighboring water molecules, known as cohesive forces. The layer of water molecules at the interface, however, are subjected to forces not only due to the water molecules in the bulk, but also forces from molecules that exist in air, known as adhesive forces. Because cohesive forces are stronger than adhesive forces, the topmost layer of water molecules are pulled inwards and parallel to the surface. This creates a phenomenon known as surface



tension.<sup>18,19</sup> It is the reason objects with a higher density, such as paper clips, can float in a glass of water.

At a more fundamental level, analysis of the physiochemical composition of bulk material surfaces can inform on large scale processes such as mineralization and dissolution.<sup>20-22</sup> In particular, at the solid-aqueous interface, properties of the solid surface such as its charge, roughness, and degree of hydrophilicity can influence the arrangement of water molecules at the interface.<sup>23-26</sup> A charged surface, for instance, exerts electrostatic forces that can align water molecules and strongly alter their ordering at the interface ( $\sim 1-10$  nm from the surface) from that found in the bulk, several Debye lengths (the length scale over which these electrostatic effects persist) away.<sup>27</sup> This strongly suggests that the ordering of interfacial water molecules is more structured at the interface than in the bulk. Similarly, the chemistry characterizing the aqueous solution, such as its pH and ionic strength, can influence the surface chemistry of the solid and, hence, also affect the arrangement and orientation of water molecules at the surface.<sup>24,28,29</sup> As an example, consider the effect of pH on the arrangement of water at the silica-aqueous interface. At a neutral pH of 7, the silica surface is negatively charged<sup>29</sup> and the interfacial water molecules are found in an aligned structure influenced by the electrostatic forces of the charged interface. In contrast, the silica surface is electrostatically neutral at a pH of 2.3, called the point of zero charge (PZC), and the resulting arrangement of water molecules at the mineral surface is less structured.<sup>29-31</sup>

Through the examples listed above, it is clear that understanding the interactions within aqueous interfaces is essential to many chemical processes. The description of the relevant aqueous interfaces mentioned in this introduction is provided as context and this

thesis delves further into the specificities of interfacial water structuring in two specific frameworks, namely, at the nano-bio interface and the metal:metal:oxide:aqueous interface. Using vibrational non-linear optical spectroscopy, the structure of interfacial water molecules is assessed in detail with this work contributing to our broader understanding of aqueous interfaces.

## **1.2. Assessing Interfacial Water Structure: The Nano-Bio Interface**

The nano-bio interface is complex and encompasses three different components.<sup>32</sup> The first two include the surface composition of the nanoparticle and its response to contact with a liquid medium. Metal nanoparticles have been widely studied for the development of electrochemical and biological sensors<sup>33-36</sup> due to their high active surface areas and tunable size. These nanoparticles, however, tend to aggregate, leading to a decreased surface area per particle. To mitigate this structural instability and further optimize their function, various modifications to the nanoparticle surface have been investigated using ligands, polymers, and surfactants.<sup>37,38</sup> In the literature, it has been found that, depending on the method in which the nanoparticles are purified, there exists not only functionalized nanoparticles, but also a mixture of functionalized nanoparticles and free ligand in solution.<sup>39</sup> Therefore, understanding the role of the unbound ligand can be as important as the modified nanoparticle itself. To this end, we study the behavior of the polymer, poly (allylamine hydrochloride) (PAH), a commonly used nanoparticle functionalizing agent,<sup>35,40,41</sup> as a free ligand in this thesis.

The final component of the nano-bio interface concerns the interaction of the nanoparticle-aqueous interface with the biological substituent. With the emerging usage of nanomaterials in agricultural and commercial applications, the likelihood of these materials coming into contact with biological systems is high.<sup>42,43</sup> Therefore, it is vital to understand whether or not there exist adverse effects associated with the release of these materials into the environment. Herein, the interaction of PAH with supported lipid bilayers (SLBs) is analyzed. Specifically, changes to the interfacial water structure at the bilayer surface with the addition of PAH is studied using vibrational non-linear optical techniques (Section 1.2.1).

Membrane hydration is extremely important in driving the assembly of biological membranes.<sup>44</sup> It is also essential for membrane function as many biochemical processes involve water, including processes such as the disposal of cellular waste, cell-to-cell signaling, and diffusion.<sup>45</sup> Water molecules can directly hydrogen-bond to the lipid head groups to form this layer of hydration. They can also penetrate into the bilayer, existing in interchain hydrogen bonds with the lipid fatty acyl chains.<sup>46,47</sup> Thus, the formation and disruption of the interfacial hydrogen-bonding network should inform on the presence of these water molecules.

### **1.2.1. Probing the Interfacial Water Structure: Vibrational Sum Frequency Generation (SFG) Spectroscopy**

Several different methods exist for studying the hydrogen-bonding network at lipid bilayer surfaces. Neutron diffraction has been used to determine the degree of hydration around lipid headgroups using H<sub>2</sub>O/D<sub>2</sub>O exchange.<sup>48,49</sup> Although powerful, this technique

is hindered by the poor stability of the lipid films and the need for a neutron source.<sup>50</sup> Fluorescence spectroscopy is an alternative, less destructive technique that has been used to study lipid hydration, however, it requires the use of fluorescent probes (PRODAN, for example).<sup>51,52</sup> The interaction of these probes with the neighboring lipid and water molecules is often unreported and can change depending on the location and orientation in which the probe was inserted. Therefore, as a label-free, interface-selective method to study the nano-bio interface, vibrational sum frequency generation (SFG) spectroscopy<sup>53-56</sup> is employed. Using SFG spectroscopy, the structure and orientation of interfacial water molecules above lipid membranes can be assessed.<sup>53,57,58</sup> The formation of supported lipid bilayers through the vesicle fusion method has also been studied thoroughly in the literature and has been widely utilized to produce lipid bilayers that are stable and uniform on surfaces such as silica and mica.<sup>59,60</sup> The use of SFG spectroscopy in this thesis to probe the interaction mentioned in Section 1.2 is complemented with computational studies found in the literature that shed light on the hydration of bilayers composed of different lipids. The numerical simulations have contributed to our understanding of the structure and dynamics of hydrogen-bonding occurring at lipid-aqueous interfaces.<sup>61,62</sup>

### **1.3. Assessing Interfacial Water Structure: The Metal:Metal:Oxide-Aqueous Interface**

Less straightforward to address than the structure of interfacial water at biological surfaces is the structure of such water molecules at metal:metal:oxide interfaces. Recently, it has been reported that thin nanolayers of Earth-abundant metals such as nickel, iron, and vanadium have been shown to produce current densities of a few  $\mu\text{A}/\text{cm}^2$  when in

contact with ionic water droplets. Due to the presence of multiple metal oxidation states in the passive oxide nano-overlayer, which forms spontaneously in air,<sup>63,64</sup> the electrostatic potential at the metal:oxide-water interface can polarize the underlying metal, thus promoting intra-oxide electron transfer when an ionic droplet is moved across the film surface.<sup>65</sup> When compared to other promising energy conversion devices such as graphene, the current and voltage values are similar.<sup>66-68</sup> The metal nanolayers, however, can be synthesized in a more efficient way as it requires only a single-step deposition process and is relatively inexpensive to produce at scale.

The influence of aqueous solutions on the electrical activity of the metal nanolayers is clear from the mechanism detailed above and understanding the interfacial water structure at such surfaces is vital to our understanding of the electrochemical prospects and corrosion processes therein. In the literature, the structure of water on single-crystal transition metal surfaces have been studied using scanning tunneling microscopy (STM) and density functional theory (DFT) calculations.<sup>1,69-71</sup> However, STM is limited as it cannot inform on entire hydrogen-bonding networks very easily, as it is typically used to identify surface water on metals with single-molecule resolution.<sup>72</sup> Furthermore, the STM probe can perturb the water structure due to tip-water forces. The gap in understanding the hydrogen-bonding network at metal:metal:oxide:aqueous interfaces has been acknowledged by the scientific community with the limitations of many techniques addressed in detail. For example, one study that applied SFG spectroscopy to study interfacial water on nanolayer thin films of gold and titanium showed that complications due to Fresnel factors can interfere with the lineshapes obtained at such interfaces.<sup>73</sup> A detailed description of Fresnel factors is presented in Chapter 2. Since this study, we have taken into

consideration many of the challenges that plague the use of SFG spectroscopy to probe the metal:metal:oxide:aqueous interface and have achieved significant progress.

This work is detailed in Chapter 5 in which we study the structure of interfacial water at the nickel:nickel:oxide surface using SFG spectroscopy supplemented with calculations used to help separate the signals due to vibrations of water from artifacts arising from Fresnel factors. In this study, nickel is chosen due to its ability to convert mechanical energy to gravitational energy by the mechanism outlined above.<sup>65</sup>

#### 1.4. Scope and Organization of Thesis

The background presented in this chapter was meant to define the interfaces of interest that will be discussed further in this thesis. As mentioned, we aim to understand the interfacial water structure associated with both biological and electrochemical systems using nonlinear optical spectroscopy. In Chapter 2, a brief theory of nonlinear optics and sum frequency generation (SFG) spectroscopy is detailed. Within that chapter, the optical set-up is also described.

Chapter 3 focuses on understanding perturbations to the interfacial hydrogen-bonding network above supported lipid bilayers (SLBs) when the polycation, poly (allylamine hydrochloride) (PAH) is introduced into the system at various concentrations. In this chapter, the electrostatics involved in this interaction is explored by experimenting with lipids that possess different headgroups. Further insight into this interaction is provided by simulations that have been done in the literature that explore lipid hydration.

Chapter 4 provides a summary of the experiments done in Chapter 3 as well as the connection of this work to previous work done in the lab that focused on studying polymer

and peptide:lipid membrane interfaces. A review of this work highlights the multifaceted approach used in our group combining nonlinear optical spectroscopy, SFG spectroscopy as well as second harmonic generation (SHG) spectroscopy (described further in Chapter 4), with atomistic and coarse-grained simulations and quartz crystal microbalance with dissipation monitoring (QCM-D). Future work studying the interfacial hydrogen-bonding network above model lipid membranes integrated with the peptide gramicidin A is also discussed in this chapter.

In Chapter 5, the hydrogen-bonding network at the nickel:nickel:oxide:aqueous interface is explored. This chapter aims to characterize the surface of 3–4 nm thick nickel films using contact angle goniometry, scanning electron microscopy (SEM), Fourier transform infrared spectroscopy (FTIR), X-ray photoelectron spectroscopy (XPS), and SFG spectroscopy. The details of each technique used is mentioned in Chapter 5 as well. This chapter also discusses the changes to the interfacial water structure as a function of pH and ionic strength.

As Chapter 5 will describe in detail, elucidating dangling –OH bonds in the geometry used (internal) could not be done due to interference from Fresnel factors. Therefore, Chapter 6 describes future work that can be done to probe these weak hydrogen-bonding interactions in a different geometry (external) by introducing water vapor to the nickel:nickel:oxide films.

## CHAPTER 2

**Nonlinear Optics and Sum Frequency Generation Spectroscopy****2.1. Introduction to Vibrational Sum Frequency Generation (SFG) Spectroscopy**

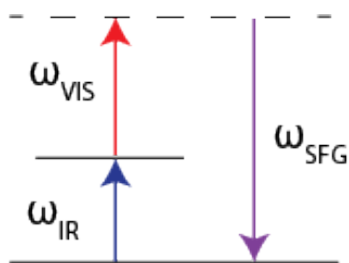
Vibrational sum frequency generation (SFG) spectroscopy is a second-order nonlinear optical technique that is interface-selective due to symmetry constraints.<sup>1-3</sup> Under the electric dipole approximation, the second-order susceptibility is a third-rank tensor, which formally vanishes for systems with an inversion center, as in bulk media.<sup>2,4,5</sup> At an interface (described in Chapter 1), this symmetry is broken, giving rise to three-wave mixing processes, including sum frequency generation (SFG), different frequency generation (DFG), and second harmonic generation (SHG). The SFG process utilized in this thesis results from the spatial and temporal overlap of two pulsed laser beams, namely, a fixed visible beam, and a tunable IR beam. The light emitted from this process is at the sum of the two input frequencies as shown in Figure 2.1a. Vibrational spectra of interfacial molecules can then be obtained if the vibrational modes of the molecules coincide with the frequency of the IR beam (resonant enhancement).

Polarization allows for the selection of a specific orientation of molecules at the interface.<sup>6-8</sup> The two linear polarizations are called  $p$  and  $s$ , where  $p$ -polarized light lies within the plane of incidence and  $s$ -polarized light is normal to the plane of incidence. This is shown in Figure 2.1b. The polarization sequence characterizing the SFG measurement

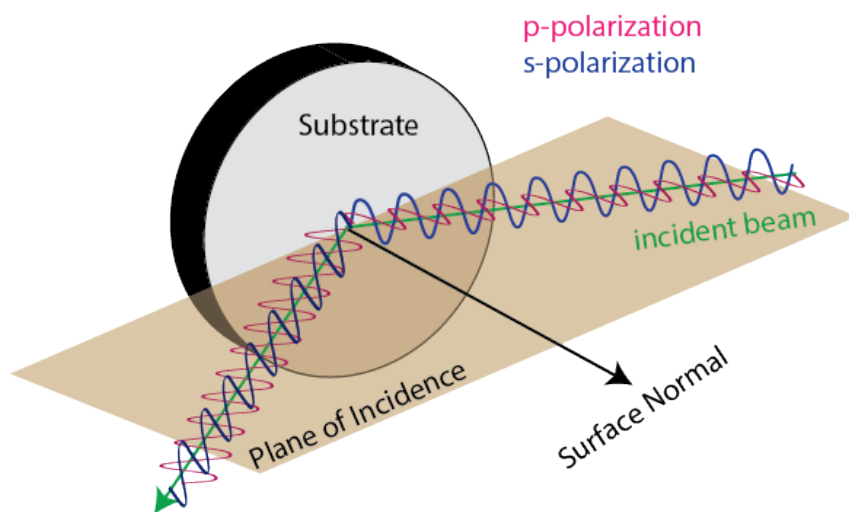


is usually written as a combination of the SFG, visible, and IR light, for example PPP-polarization stands for *p*-polarized SFG light (*p*-SFG), *p*-polarized visible light (*p*-VIS), and *p*-polarized IR light (*p*-IR). This notation is used throughout this thesis.

SFG spectroscopy has been applied to a variety of different interfaces and systems. It has been used to study polymers such as polystyrene (PS) and poly (methyl methacrylate) (PMMA), due to the impact surface properties such as wettability and adhesion have on their function as coating materials.<sup>9-11</sup> It has also been applied to several geochemical,<sup>5,12</sup> electrochemical,<sup>13-16</sup> atmospheric,<sup>17-20</sup> and biological<sup>21-26</sup> systems at relevant respective interfaces. Our group has previously studied the nano-bio interface, focusing on two specific vibrational regions: the C–H (2,700–3,000 cm<sup>-1</sup>) and O–H (3,000–3,800 cm<sup>-1</sup>) stretching regions.<sup>23,24,27</sup> The use of this approach to study not only the nano-bio interface, but also the metal:metal:oxide-water interface, is expanded on further in this thesis.



(a) Energy level diagram of the sum frequency generation process



(b) Directionality of the *s*- and *p*-polarized light relative to the plane of incidence

Figure 2.1. Introduction to SFG

## 2.2. Nonlinear Optics and Sum Frequency Generation (SFG) Theory

Under the application of an external electric field,  $\mathbf{E}(t)$ , polarizable materials will acquire an induced dipole moment. The sum of dipole moments per unit volume is defined as the polarization,  $\mathbf{P}(t)$ . Formally, the induced dipole acts as a source for the radiation field that is the detected spectroscopic signal, however, one can show that  $\mathbf{E}_{\text{signal}}(t) \propto i\mathbf{P}(t)$ , therefore, to interpret the emitted field, it suffices to understand the form of the induced polarization. In the case of linear optics, the induced polarization is simply proportional to the applied electric field. This is often described by the relationship shown in Equation 2.2.1.<sup>2</sup>

$$(2.2.1) \quad \mathbf{P}(t) = \epsilon_0 \chi^{(1)} \mathbf{E}(t)$$

Here,  $\chi^{(1)}$  is the linear susceptibility matrix, describing the strength of the induced polarization response, and  $\epsilon_0$  is the permittivity of free space. The optical response in nonlinear optics is more complicated. For weak fields (weak compared to the strength of molecular bonding), the induced polarization may be described by expanding  $\mathbf{P}(t)$  in a power series of the applied field<sup>2,28</sup>

$$(2.2.2) \quad \begin{aligned} \mathbf{P}(t) &= \epsilon_0 [\chi^{(1)} \mathbf{E}(t) + \chi^{(2)} \mathbf{E}^2(t) + \chi^{(3)} \mathbf{E}^3(t) + \dots] \\ &\equiv \mathbf{P}^{(1)}(t) + \mathbf{P}^{(2)}(t) + \mathbf{P}^{(3)}(t) + \dots, \end{aligned}$$

where  $\chi^{(2)}$  and  $\chi^{(3)}$  are the second- and third-order nonlinear susceptibility tensors, respectively. For SFG, the electric field  $\mathbf{E}(t)$  is represented by the two beams of light impinging upon the surface, denoted by the associated electric fields  $\mathbf{E}_1$  and  $\mathbf{E}_2$ , and their respective

oscillation frequencies,  $\omega_1$  and  $\omega_2$ .

$$(2.2.3) \quad \mathbf{E}(t) = \mathbf{E}_1 \cos(\omega_1 t) + \mathbf{E}_2 \cos(\omega_2 t)$$

Therefore, inserting Equation 2.2.3 into Equation 2.2.2, we can obtain the second-order polarization response as:

$$(2.2.4) \quad \begin{aligned} \mathbf{P}^{(2)}(t) &= \epsilon_0 \chi^{(2)} (\mathbf{E}_1 \cos(\omega_1 t) + \mathbf{E}_2 \cos(\omega_2 t))^2 \\ &= \epsilon_0 \chi^{(2)} [|\mathbf{E}_1|^2 \cos^2(\omega_1 t) + |\mathbf{E}_2|^2 \cos^2(\omega_2 t) + 2\mathbf{E}_1 \cdot \mathbf{E}_2 \cos(\omega_1 t) \cos(\omega_2 t)] \end{aligned}$$

and using the well-known product-to-sum trigonometric identity

$$(2.2.5) \quad \cos(x) \cos(y) = \frac{1}{2} (\cos(x + y) + \cos(x - y))$$

on each term in Equation 2.2.4, we obtain the following expression for the second-order induced polarization

$$(2.2.6) \quad \begin{aligned} \mathbf{P}^{(2)}(t) &= \frac{1}{2} \epsilon_0 \chi^{(2)} (|\mathbf{E}_1|^2 + |\mathbf{E}_2|^2) \\ &+ \frac{1}{2} \epsilon_0 \chi^{(2)} |\mathbf{E}_1|^2 \cos(2\omega_1 t) + \frac{1}{2} \epsilon_0 \chi^{(2)} |\mathbf{E}_2|^2 \cos(2\omega_2 t) \\ &+ \epsilon_0 \chi^{(2)} \mathbf{E}_1 \cdot \mathbf{E}_2 \cos[(\omega_1 - \omega_2)t] \\ &+ \epsilon_0 \chi^{(2)} \mathbf{E}_1 \cdot \mathbf{E}_2 \cos[(\omega_1 + \omega_2)t] \end{aligned}$$

which contains nonlinear optical signals corresponding to the DC field, second harmonic generation (SHG), difference frequency generation (DFG), and sum frequency generation (SFG). For most of this thesis, we focus on the sum frequency portion of Equation 2.2.6,

given by<sup>29,30</sup>

$$(2.2.7) \quad \mathbf{P}_{\text{SFG}}^{(2)} = \epsilon_0 \chi^{(2)} \mathbf{E}_1 \cdot \mathbf{E}_2 \cos[(\omega_1 + \omega_2)t]$$

In our experiments, as mentioned, we overlap both a visible beam oscillating at fixed frequency  $\omega_{\text{VIS}}$  and IR beam oscillating at tunable frequencies  $\omega_{\text{IR}}$  to produce a beam at the sum of both frequencies  $\omega_{\text{VIS}} + \omega_{\text{IR}}$ . Therefore, Equation 2.2.7 can be rewritten as:

$$(2.2.8) \quad \mathbf{P}^{(2)} = \epsilon_0 \chi^{(2)} \mathbf{E}_{\text{IR}} \cdot \mathbf{E}_{\text{VIS}} \cos[(\omega_{\text{VIS}} + \omega_{\text{IR}})t]$$

The relationship between the second-order polarization and sum frequency signal  $I_{\text{SFG}}$  can then be related by the following<sup>16</sup>

$$(2.2.9) \quad |\mathbf{P}_{\text{SFG}}^{(2)}| \propto I_{\text{SFG}} \propto |\chi_{\text{eff}}^{(2)}|^2$$

$\chi_{\text{eff}}^{(2)}$  can be further expanded to reveal both resonant  $\chi_{\text{surface}}^{(2)}$  and nonresonant  $\chi_{\text{NR}}^{(2)}$  contributions to the sum frequency signal.<sup>23,31-35</sup>

$$(2.2.10) \quad \chi_{\text{eff}}^{(2)} = \chi_{\text{NR}}^{(2)} + \chi_{\text{surface}}^{(2)} + \frac{\kappa}{\sqrt{\kappa^2 + \Delta k_z^2}} e^{i \arctan(\frac{\Delta k_z}{\kappa})} \Phi(0) \chi^{(3)}$$

where  $\kappa$  is the inverse Debye screening length,  $\Delta k_z$  is the inverse coherence length of the sum frequency process, and  $\Phi(0)$  is the interfacial potential.

### 2.3. Fresnel Factors

Fresnel factors describe the reflection of light on a surface as a function of angle of incidence and wavelength of light. Calculations regarding these Fresnel factors are evaluated

in Chapter 5 to present a correct interpretation of our SFG spectra. In our experiments, we use a three-layer system, composed of the substrate ( $\text{CaF}_2$ ), the nickel:nickel:oxide nanolayer, and water. The spectra are taken in PPP-polarization. For an in-plane isotropic surface, according to symmetry rules, the  $x$  and  $z$  components at the surface (where  $xyz$  are Cartesian coordinates in the lab frame described in Figure 2.2) can be resolved with  $p$ -polarization, therefore,  $zzz$ ,  $xzx$ ,  $zxx$ , and  $xzx$  contribute to the acquired PPP sum frequency spectra.<sup>6,36</sup> Here,  $z$  is taken to be surface normal. The following relationships then result:<sup>37–40</sup>

$$(2.3.1) \quad \chi_{\text{eff,ppp}}^{(2)} = A\chi_{zzz}^{(2)} - B\chi_{xzx}^{(2)} + C\chi_{zxx}^{(2)} - D\chi_{xzx}^{(2)}$$

$$(2.3.2) \quad A = L_{zz}(\omega_{\text{SFG}})L_{zz}(\omega_{\text{VIS}})L_{zz}(\omega_{\text{IR}}) \sin \theta_{\text{SFG}} \sin \theta_{\text{VIS}} \sin \theta_{\text{IR}}$$

$$(2.3.3) \quad B = L_{xx}(\omega_{\text{SFG}})L_{xx}(\omega_{\text{VIS}})L_{zz}(\omega_{\text{IR}}) \cos \theta_{\text{SFG}} \cos \theta_{\text{VIS}} \sin \theta_{\text{IR}}$$

$$(2.3.4) \quad C = L_{zz}(\omega_{\text{SFG}})L_{xx}(\omega_{\text{VIS}})L_{xx}(\omega_{\text{IR}}) \sin \theta_{\text{SFG}} \cos \theta_{\text{VIS}} \cos \theta_{\text{IR}}$$

$$(2.3.5) \quad D = L_{xx}(\omega_{\text{SFG}})L_{zz}(\omega_{\text{VIS}})L_{xx}(\omega_{\text{IR}}) \cos \theta_{\text{SFG}} \sin \theta_{\text{VIS}} \cos \theta_{\text{IR}}$$

Depending on the interface, the Fresnel factors ( $L_{xx}$ ,  $L_{yy}$ ,  $L_{zz}$ ) can then be calculated. As an example, Figure 2.2 details the main reflection and transmission contributors for an incoming beam for  $L_{xx}$ . Transmission across the first interface ( $t_{12}^p$ ) is denoted by (a) in Figure 2.2. There is then reflection in the opposite direction (sign change) as well as a phase shift (b). There is a propagation of that reflection at the interface bound by medium 1 and 2 (c), again resulting in a sign change. This response can then be written as a power series, resulting in the equation shown by Equations 2.3.6 and 2.3.7.<sup>41</sup> All Fresnel factors at interface I ( $\text{CaF}_2$ :nickel:nickel:oxide) for PPP-polarization are evaluated based

on the following expressions:<sup>38,42</sup>

$$(2.3.6) \quad L_{xx}^I(\omega) = \frac{t_{12}^p}{1 + r_{12}^p r_{23}^p e^{2i\beta}} (1 - r_{23}^p e^{2i\beta}) \frac{\cos \theta_2}{\cos \theta_1}$$

$$(2.3.7) \quad L_{zz}^I(\omega) = \frac{t_{12}^p}{1 + r_{12}^p r_{23}^p e^{2i\beta}} (1 + r_{23}^p e^{2i\beta}) \frac{n_1 n_2}{n_{\text{interface,I}}^2}$$

Here,  $r_{ij}^p$ ,  $r_{ij}^s$ ,  $t_{ij}^p$ , and  $t_{ij}^s$  are the reflection and transmission coefficients for specific interfaces bound between medium  $i$  and medium  $j$  for either  $s$ - or  $p$ -polarized light. In the above equations,  $n_{1(2)}$  and  $\theta_{1(2)}$  are the refractive indices and angles of incidence for the beam in CaF<sub>2</sub> (nickel), respectively. Here,  $\beta$  accounts for the geometric path difference between successively reflected/transmitted light rays when there are multiple reflections and is defined as  $\beta = 2\pi n_2 d \cos \theta_2 / \lambda$ , where  $d$  is the thickness of the nickel:nickel:oxide film and  $\lambda$  is the wavelength of the beam. The quantities  $r_{ij}^p$ ,  $r_{ij}^s$ ,  $t_{ij}^p$ , and  $t_{ij}^s$  are calculated using the following expressions,<sup>4,38,43</sup> which are derived in detail in Appendix A.

$$(2.3.8) \quad r_{ij}^p = \frac{n_j \cos \theta_i - n_i \cos \theta_j}{n_j \cos \theta_i + n_i \cos \theta_j}$$

$$(2.3.9) \quad r_{ij}^s = \frac{n_i \cos \theta_i - n_j \cos \theta_j}{n_i \cos \theta_i + n_j \cos \theta_j}$$

$$(2.3.10) \quad t_{ij}^p = \frac{2n_i \cos \theta_i}{n_j \cos \theta_i + n_i \cos \theta_j}$$

$$(2.3.11) \quad t_{ij}^s = \frac{2n_i \cos \theta_i}{n_i \cos \theta_i + n_j \cos \theta_j}$$

For a three-layer system, such as that used in Chapter 5, the Fresnel factors for interface II (nickel:nickel:oxide:water) also need to be considered. (Note: the former sentence represents medium 3 as water, however, deuterium oxide was also used as medium 3 to

correct for the frequency-dependent IR profile before each experiment). The pertinent Fresnel factors for interface II (PPP-polarization) are represented here:<sup>38</sup>

$$(2.3.12) \quad L_{xx}^{II}(\omega) = e^{i\Delta} \frac{t_{12}^p}{1 + r_{12}^p r_{23}^p e^{2i\beta}} (1 - r_{23}^p) \frac{\cos \theta_2}{\cos \theta_1}$$

$$(2.3.13) \quad L_{zz}^{II}(\omega) = e^{i\Delta} \frac{t_{12}^p}{1 + r_{23}^p r_{23}^p e^{2i\beta}} \frac{n_1 n_2}{n_{\text{interface,II}}^2}$$

Here,  $e^{i\Delta}$  is a phase factor that accounts for the phase differences in sum frequency signal generated by both interfaces (I and II) with  $\Delta$  expressed for each of the three beams as follows:<sup>38,43</sup>

$$(2.3.14) \quad \Delta_{\text{SFG}} = \frac{2\pi n_{2,\text{SFG}} d}{\lambda_{\text{SFG}}} \cos \theta_{2,\text{SFG}}$$

$$(2.3.15) \quad \Delta_{\text{VIS}} = \frac{2\pi n_{2,\text{VIS}} d}{\lambda_{\text{VIS}}} \cos \theta_{2,\text{VIS}} - \frac{2\pi n_{1,\text{VIS}} d}{\lambda_{\text{VIS}}} (\tan \theta_{2,\text{VIS}} + \tan \theta_{2,\text{SFG}}) \sin \theta_{1,\text{VIS}}$$

$$(2.3.16) \quad \Delta_{\text{IR}} = \frac{2\pi n_{2,\text{IR}} d}{\lambda_{\text{IR}} \cos \theta_{2,\text{IR}}} - \frac{2\pi n_{1,\text{IR}} d}{\lambda_{\text{VIS}}} (\tan \theta_{2,\text{IR}} + \tan \theta_{2,\text{SFG}}) \sin \theta_{1,\text{IR}}$$



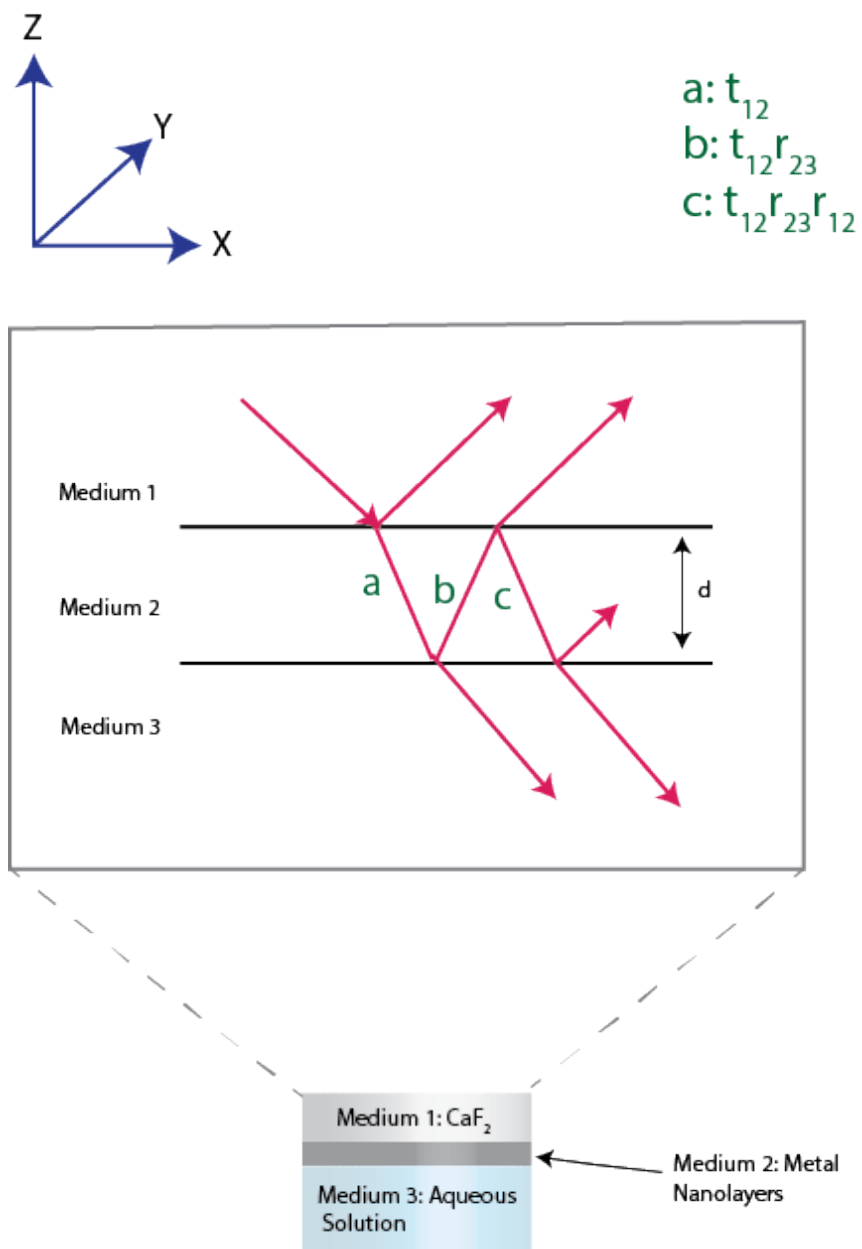


Figure 2.2. The reflection and transmission contributions from interface I and II used in the calculation of  $L_{xx}$ . Figure adapted from ref. [41]

## 2.4. Sum Frequency Generation (SFG) Set-Up

The optical set-up used in both Chapters 3 and 5 is briefly explained here and is shown in Figure 2.3. A Ti:Sapphire laser system (Spectra Physics Solstice) producing 795 nm pulses with a 120 fs pulse duration was split by a 90:10 beam splitter, where 90% of the beam is used to pump a tunable optical parametric amplifier (TOPAS) in order to generate a broadband IR beam. The remaining 10% is used as the visible upconverter beam. The TOPAS output was directed through a longpass IR filter and polarized using a holographic wire grid polarizer (Thorlabs; BaF<sub>2</sub>, 25 mm). This polarizer was used for the experiments in Chapter 5 to attenuate the IR power of the beam and was not present for the experiments done in Chapter 3. As mentioned in Section 2.1 and shown by Figure 2.1b, the polarizer can select for either *s*- or *p*- polarization from already linearly polarized light. The maximum power and sum frequency signal should be apparent when the polarizer is set to *p*- and the minimum power and sum frequency signal should be apparent when the polarizer is set to *s*-. The change from *p*- to *s*- polarization ideally occurs within a 90° rotation of the polarizer. However, a control experiment done for our system (Figure 2.4) shows that there are points at maximum and minimum power that do not yield the respective maximum and minimum sum frequency signal intensity (for example at  $\sim 120^\circ$ ). This was found to be the case when the polarizer was rotated counterclockwise. The extinction ratio, which is a measure of the ability of a polarizer to attenuate a polarized beam, for this wire grid polarizer is  $>150:1$ .<sup>44</sup> This number can be greater than 40,000:1 when two polarizers are used in series. The lower extinction ratio could be the cause for the discrepancy in obtaining maximum signal at maximum power and vice versa. Therefore, we are currently rotating the polarizer clockwise to obtain

signal intensities that coincide correctly with the input IR power. In the future, another wire grid polarizer can be bought to possibly fix this issue.

After the wire grid polarizer, the IR beam was focused onto the sample using a  $\text{CaF}_2$  focusing lens. The 10% of the 795 nm pulse used for the visible beam was directed through a variable density filter for power attenuation. The visible power stayed between 1.0–1.7  $\mu\text{J}$  at the sample stage for the duration of the experiments mentioned in Chapters 3 and 5 (with the visible power being closer to 1.0  $\mu\text{J}$  for the experiments done in Chapter 5). After the variable density filter, the beam was directed to a delay stage composed of two gold mirrors (3 mm thick). This was used to achieve temporal overlap with the IR beam at the sample stage. The beam was then sent through a band pass filter to obtain good spectral resolution and a half-waveplate to control the polarization of the visible beam. The beam was then focused onto the sample using a focusing lens.

The output SFG beam was recollimated and passed through a polarizer and half-waveplate. Lastly, the beam was directed through a focusing lens, a shortpass filter, and a notch filter. The notch filter was used to remove any stray light not associated with the sum frequency process. The SFG signal was then detected by a charged coupled device (CCD) camera. The CCD camera was cooled with liquid nitrogen each morning.

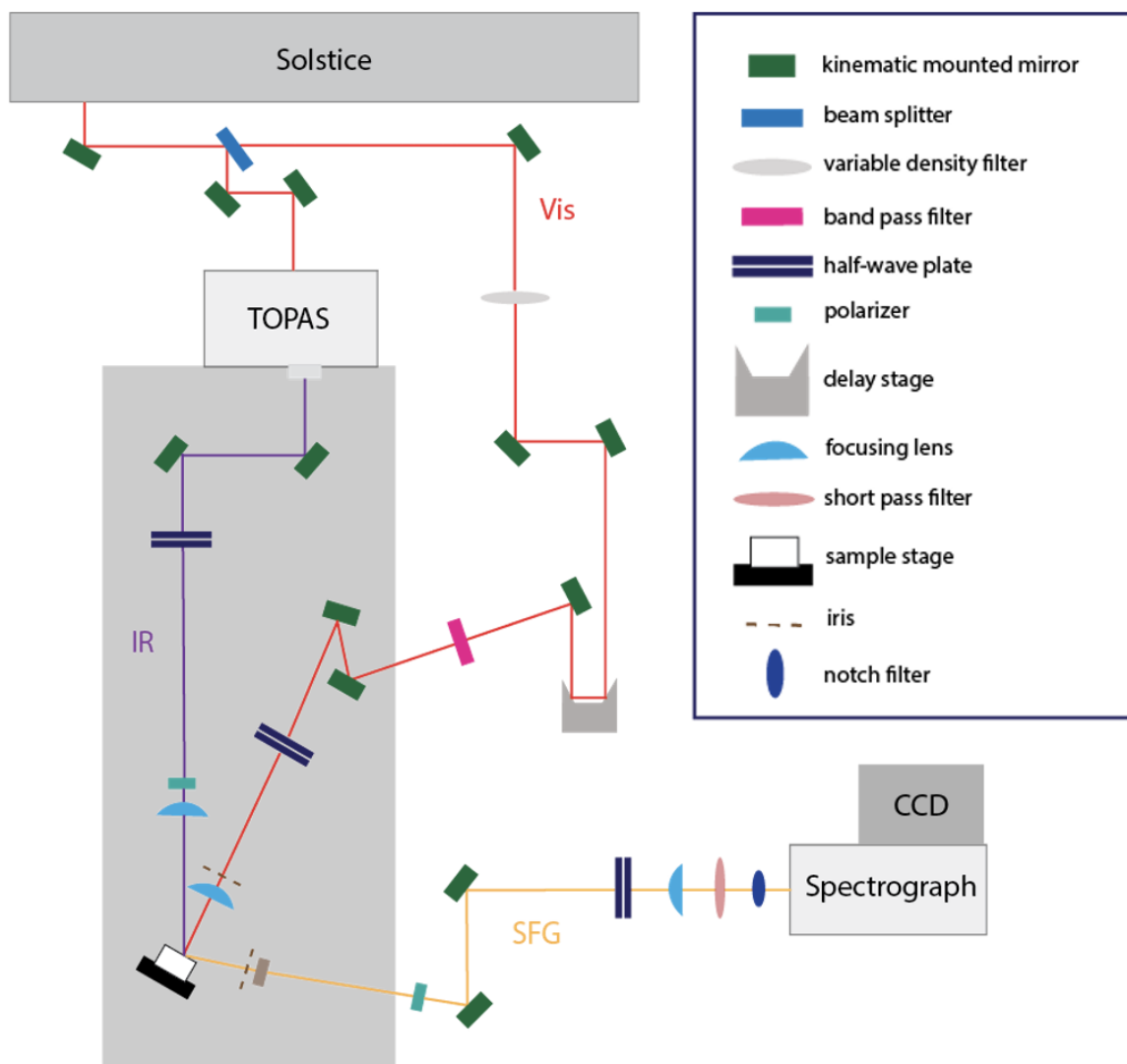


Figure 2.3. A detailed schematic of the sum frequency generation set-up used in both Chapters 3 and 5.

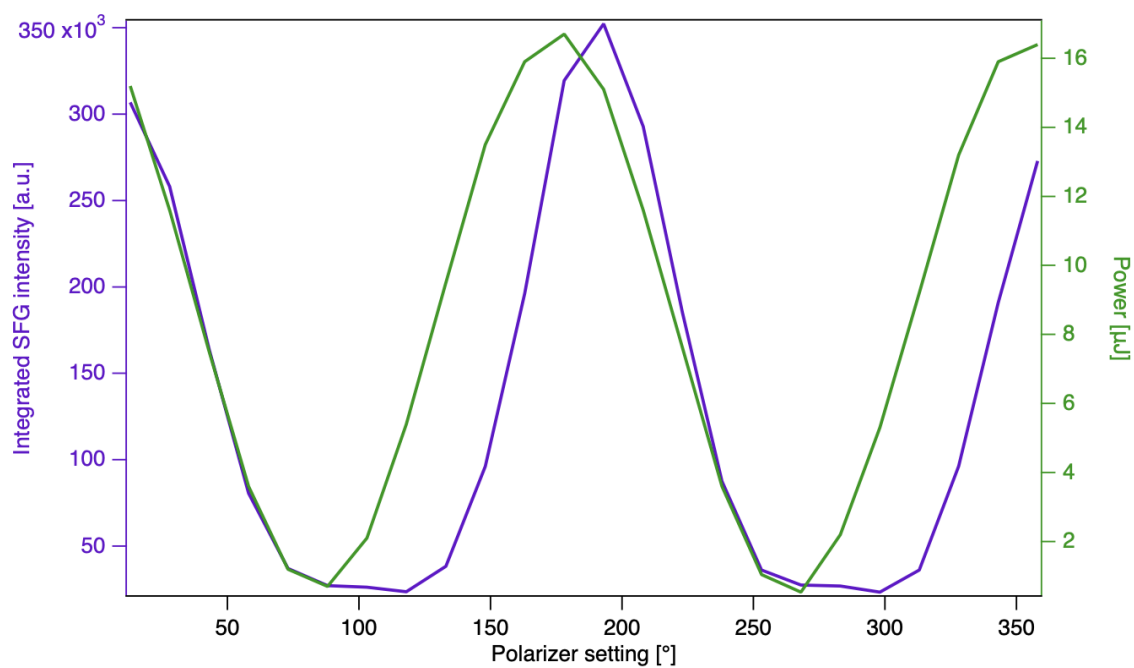


Figure 2.4. A control experiment where the polarizer was rotated every 15° and the power (green) and sum frequency intensity (purple) on gold was recorded

## 2.5. Optical Window Preparation

The substrates used in Chapter 3 were ALD  $\text{SiO}_2$  (25 nm) coated  $\text{CaF}_2$  windows (3 mm thick, 25.4 mm diameter from ISP Optics). Due to the high concentration (1 mM) and stickiness of the polycation used in these experiments, these substrates were only used a maximum of 4 times. These windows were cleaned by first sonicating them in methanol for 15 mins. They were then dried with nitrogen and plasma cleaned (Harrick Plasma Cleaner, 300–500 Torr) for approximately 10 minutes. The substrates used in Chapter 5 were solely  $\text{CaF}_2$  windows. They were cleaned in the same way as the ALD substrates.

## 2.6. Summary

Vibration sum frequency generation spectroscopy has been instrumental in both studies of the nano-bio and metal:metal:oxide interfaces in this thesis. The brief account of nonlinear optics theory and Fresnel factor calculations discussed here is further expanded on and applied in Chapter 5. Supporting information regarding any experimental sample set-ups and supplementary techniques are mentioned in each respective chapter.

## CHAPTER 3

**Perturbation of Hydrogen-Bonding Networks Over Supported  
Lipid Bilayers by Poly (allylamine hydrochloride)**

**Portions of this chapter are reproduced in part with permission from the  
American Chemical Society:**

Dalchand, N.; Doğangün, M.; Ohno, P.E.; Ma, E.; Martinson A.B.F.; Geiger, F. M.,  
Perturbation of Hydrogen-Bonding Networks over Supported Lipid Bilayers by Poly  
(allylamine hydrochloride). *J. Phys. Chem. B* **2019**, 123, 4251–4257.

### 3.1. Introduction

As mentioned in Chapter 1, nanoparticles can be functionalized with ligands and polymers to control their surface chemistry. The cationic polymer, poly (allylamine hydrochloride) (PAH, Figure 3.1A), is widely used as a coating for nanoparticles<sup>1-3</sup> and exists in substantial amounts as free PAH in equilibrium with bound PAH in nanoparticle solutions, even after purification. Given the toxicity of PAH to bacteria,<sup>4</sup> it is of interest to analyze free PAH with lipid membranes so as to further understand its lysing action. While our prior studies of free-PAH characterized the thermodynamic and structural changes to SLBs upon PAH adsorption by monitoring structural changes to the lipids in the C–H stretching region,<sup>5,6</sup> we now focus specifically on probing how the H-bond network of the water molecules that constitute the electrical double layer over the membrane varies during interaction with the polycations.

Maintenance of a homeostatic aqueous environment on both sides of a cell membrane is crucial as this aqueous medium is where vital biochemical processes occur.<sup>7-9</sup> The cell membrane is a key component to sustaining this homeostasis as it acts as a selective barrier to control the movement of ions and small molecules into and out of the cell.<sup>10,11</sup> Therefore, unanticipated changes to the cell membrane can also alter its surrounding environment, ultimately disrupting important biological pathways. It has been reported that ions, polycations, and nanomaterials are prone to perturb supported lipid bilayers (SLBs), idealized model cell membranes,<sup>7,12</sup> and cause physical changes such as lipid asymmetry<sup>13-16</sup> and the formation of lipid coronas.<sup>5,17-19</sup> While informative, these results are specific to the SLBs and not their surrounding aqueous environment. Thus, further analysis of the aqueous surroundings is an important factor in obtaining a complete and



fundamental understanding of the molecular mechanisms associated with membrane interactions. Moreover, water at biologically relevant membranes exhibit properties that are still under debate, including those influencing structural networks resembling ice vs water<sup>10,20</sup> or bulk-like vs considerably reduced relative permittivity.<sup>21</sup>

Given their importance in biological membranes, we study lipids terminated with the zwitterionic phosphocholine (PC) headgroup as well as the anionic phospho-(1-*rac*-glycerol) and phospho-L-serine (PG and PS) headgroups (Figures 3.1B–D). Here, we monitor the interfacial hydrogen-bonding (H-bonding) network above membranes formed from zwitterionic and anionic lipids as we add varying concentrations of PAH.

To probe the very initial stages of membrane disruption by PAH, which presumably involves PAH interactions with the membrane-bound water molecules, we employ  $\mu\text{M}$  polycation concentrations but also employ higher polycation concentrations, which disrupt the bilayers permanently, as demonstrated in detail in our prior work.<sup>5</sup> We now probe the water O–H stretching region and do so with vibrational sum frequency generation (SFG) spectroscopy. This technique is a naturally appropriate for studying aqueous interfaces, as it is inherently surface sensitive,<sup>22–27</sup> allowing us to probe a thin interfacial region of water above the membrane while providing detailed molecular information about the strength of the hydrogen bond network through a detailed analysis of the second-order spectral lineshapes.<sup>28–30</sup> Prior work has shown that the membrane/water interface is a challenge to probe directly using SFG spectroscopy due to the symmetric constraints that govern the sum frequency process. To offset these constraints, past studies have employed asymmetric, chemically modified bilayers by deuteration of one of the bilayer leaflets. Our recent work using a commercially available broadband laser system at kHz repetition rates

has shown to overcome these restrictions and provide spectra with relatively good S/N after short acquisition times for unlabeled, symmetric bilayers.<sup>31</sup>

We find evidence for the displacement of interfacial water molecules for lipid bilayers formed from zwitterionic and negatively charged lipids in a fashion that impacts both strong and weak H-bond interactions. Rinsing does not lead to SFG signal recovery from the C–H and O–H oscillators, indicating that the irreversibility of PAH interaction with membranes rich in lipids such as those studied here may be detrimental to membrane function and cellular integrity. As PAH attachment blocks solvated ions and water molecules at the membrane surface, irregular diffusion and cell lysis is expected.<sup>32,33</sup>

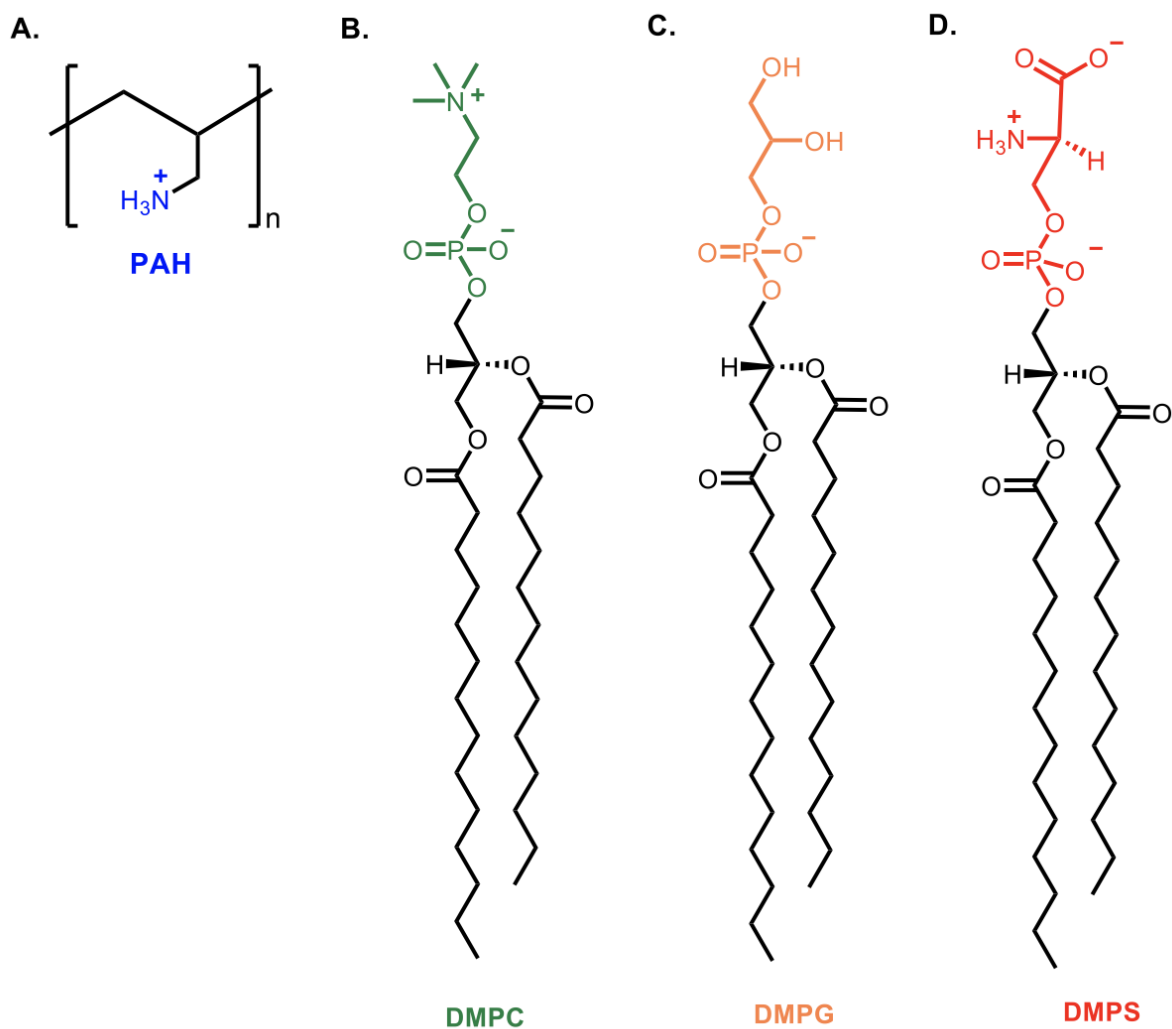


Figure 3.1. The structure of (A) cationic polymer, poly (allylamine) hydrochloride (PAH, blue), (B) zwitterionic lipid, 1,2-dimyristoyl-sn-glycero-3-phosphocholine (DMPC, green), (C) negatively charged lipid, 1,2-dimyristoyl-sn-glycero-3-phospho-(1-rac-glycerol) (DMPG, orange), and (D) negatively charged lipid, 1,2-dimyristoyl-sn-glycero-3-phospho-L-serine (DMPS, red).

## 3.2. Methods

Unless indicated otherwise, we follow our previously published methods.<sup>1,5,6,14,15,34</sup> The sections below briefly summarize the approach for the reader's convenience.

### 3.2.1. Polymer and Vesicle Preparation

Poly (allylamine hydrochloride) (PAH, 17.5 kDa) was purchased from Sigma-Aldrich and used without further purification. All stock solutions of PAH were made and stored in 0.001 M NaCl. These solutions were then diluted with buffer composed of 0.01 M Tris and 0.1 M NaCl to the final PAH concentrations used for the experiments shown in sections 3.3.1. – 3.3.3. The buffer was corrected to a final pH of  $7.40 \pm 0.5$  using dilute amounts of NaOH and HCl.

The lipids 1,2-Dimyristoyl-sn-glycero-3-phosphocholine (DMPC), 1,2-dimyristoyl-sn-glycero-3-phospho-(1-rac-glycerol) (DMPG), and 1,2-dimyristoyl-sn-glycero-3-phospho-L-serine (DMPS) were purchased from Avanti Polar Lipids. Small unilamellar vesicles were prepared from 2 mg suspensions of the following lipid combinations: 100 mol % DMPC, 90 mol % DMPC and 10 mol % DMPG, and 90 mol % DMPC and 10 mol % DMPS. The vesicle solutions were dried with N<sub>2</sub> and left in the desiccator overnight to remove any excess chloroform. The dried vesicle films were then resuspended in 0.01 M Tris and 0.1 M NaCl buffer containing 0.005 M CaCl<sub>2</sub> and extruded using a mini-extruder kit as we have shown previously.<sup>31,35</sup> SLBs are then formed using the vesicle fusion method<sup>36,37</sup> on 3 mm CaF<sub>2</sub> windows (ISP-Optics) coated with 25 nm of SiO<sub>2</sub> by atomic layer deposition (ALD). Calcium-free 0.01 M Tris and 0.1 M NaCl buffer (pH 7.4) was used for bilayer formation. Our SLBs have previously been well characterized.<sup>35</sup>

### 3.2.2. Substrate Preparation with Atomic Layer Deposition (ALD)

To avoid spurious optical contributions to the detected SFG signal from color centers that are present to varying extent within commercially available fused silica windows, we coated CaF<sub>2</sub> windows, which are free of such centers, with a thin ALD silica overlayer processed in a 125°C reactor under Argon flow in which 3DMAS [Tris (dimethylamino) silane] was added for 0.4 s, followed by a 10 s purge. O<sub>2</sub> plasma was then introduced for 20 s, followed by a 12 s purge. To yield a SiO<sub>2</sub> film of 25 nm thickness, this process was repeated for ~300 cycles. The final thickness of SiO<sub>2</sub> on the CaF<sub>2</sub> windows was then estimated from modeling the thickness deposited on witness Si substrates with variable angle spectroscopic ellipsometry.<sup>38</sup> For clarity, these windows will be referred to as 25 nm ALD SiO<sub>2</sub> substrates.

### 3.2.3. Vibrational Sum Frequency Generation Spectroscopy

SFG experiments were conducted using a Ti:Sapphire laser system (Solstice, Spectra Physics, 795 nm, 3 mJ/pulse, 1 kHz repetition rate, 120 fs pulse duration). Details of our experimental set-up have been previously reported.<sup>34</sup> Briefly, we monitored changes in the C–H (2,800 – 3,000 cm<sup>-1</sup>) and O–H (3,000 – 3,600 cm<sup>-1</sup>) stretching regions. All experiments were carried out in triplicate and conducted using internal reflection geometry. Multiple individual spectra were taken at different center IR wavelengths and different detector positions prior to being compiled together following the procedure discussed in our previous work.<sup>34</sup> All spectra were taken in SSP-polarization (*s*-polarized SFG, *s*-polarized 795 nm light, and *p*-polarized IR light) and normalized to spectra from gold coated on a CaF<sub>2</sub> window in PPP-polarization to account for the IR spectral profile. Typically, the

incident IR profile is taken using gold on  $\text{CaF}_2$  and divided by our truncated sample spectra. Because of substrate limitations in the beginning of these experiments, with the 25 nm ALD  $\text{SiO}_2$  substrates, we started normalization with a purely  $\text{CaF}_2$  substrate. After obtaining more 25 nm ALD  $\text{SiO}_2$  substrates, we coated one with gold and compared the summed gold spectrum on both substrates. Figure 3.2 shows very little difference between the two profiles. This is likely due to the layer of  $\text{SiO}_2$  being nanometers thin. Therefore, to keep the normalization process consistent, all spectra were normalized to  $\text{CaF}_2$ .

#### **3.2.4. PAH-Membrane Interaction Experiments**

Following bilayer formation, PAH was introduced into a home-built Teflon flow-cell (Figure 3.3) at a starting concentration of 1  $\mu\text{M}$ . Two acquisitions were taken in the frequency range of interest, 2,800 – 3,600  $\text{cm}^{-1}$ , before the next concentration was introduced and averaged to produce a representative spectrum for each concentration. PAH addition was stopped after the SLBs had undergone substantial perturbation. After the highest concentration of PAH was introduced, the SLBs were rinsed with 20 mL of PAH-free buffer in order to determine if changes to the SLBs were reversible.

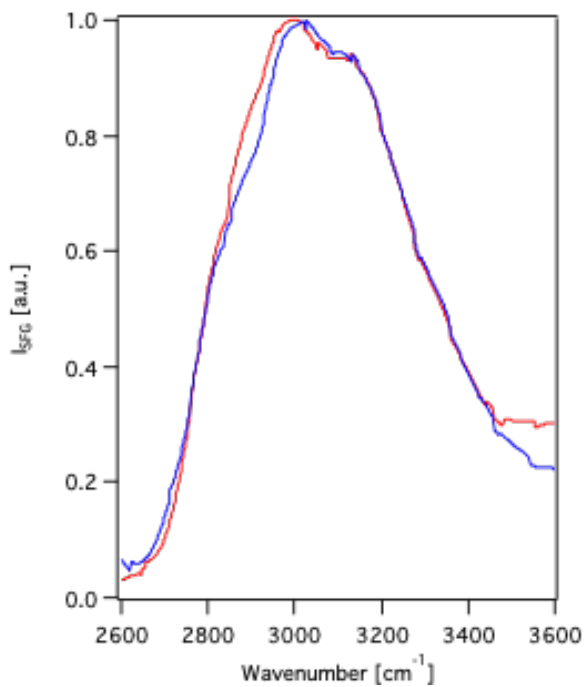


Figure 3.2. A comparison of gold on two substrates. The above plot shows the gold profile for the sum of DFG's taken for a gold  $\text{CaF}_2$  substrate (red) and a gold 25 nm ALD  $\text{SiO}_2$  coated  $\text{CaF}_2$  window (blue).

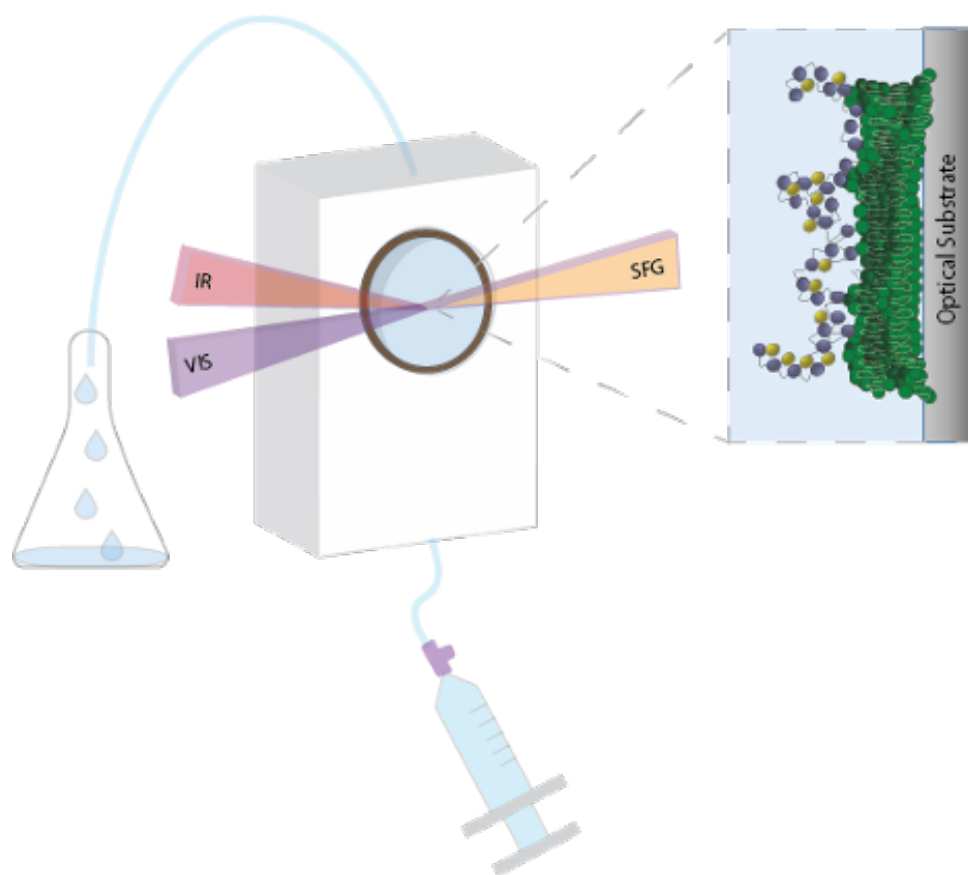


Figure 3.3. The home-built teflon flow-cell used to prepare supported lipid bilayers (SLBs). The same flow-cell was then used to monitor the interaction of the SLBs with poly (allylamine hydrochloride) (PAH).



### 3.3. Results and Discussion

#### 3.3.1. PAH Displaces Interfacial Water from Negatively Charged Membranes

Figure 3.4A shows the SSP-polarized spectrum of a SLB formed from a mixture of 9:1 DMPC:DMPG lipids exposed to varying PAH concentrations. Our prior work shows the PAH surface coverage for a bilayer formed from a 9:1 mix of DMPC:DMPG to be dense, consistent with the monolayer limit.<sup>6</sup> PAH attaches to the membrane through electrostatic interactions and not only changes the surface charge and the lipid order<sup>6,39–43</sup> but is shown here to also displace interfacial water molecules. In the C–H stretching region, Figure 3.4A shows what we had reported earlier for the C–H stretching region, namely peaks at  $\sim 2,880$   $\text{cm}^{-1}$ ,  $\sim 2,900$   $\text{cm}^{-1}$ , and  $\sim 2,950$   $\text{cm}^{-1}$  characteristic of lipids in a well-formed bilayer.<sup>14,15,35</sup> The peak at  $\sim 2,880$   $\text{cm}^{-1}$  is attributable to the symmetric  $\text{CH}_3$  stretches of the lipid alkyl tails while the SFG intensity of the other two peaks is due to spectral interference from the water molecules, as demonstrated recently using  $\text{D}_2\text{O}$  and spectral lineshape modeling.<sup>73</sup> Adding PAH to the bilayer leads to SFG intensity decreases, indicating a clear perturbation in the lipid structure with the addition of the polycations. Note that our previously reported loss of spectrally resolved peaks in the C–H stretching region at 1  $\mu\text{M}$  PAH<sup>5</sup> is somewhat at variance with our current observations, which we attribute to the differences in substrates used for experiments (25 nm ALD  $\text{SiO}_2$  on  $\text{CaF}_2$  in the present experiments vs. fused  $\text{SiO}_2$  in our previous experiments).

In the O–H stretching region, the broad peak centered  $\sim 3,200$   $\text{cm}^{-1}$  signifies the presence of strong hydrogen bonds (H-bonds) between water molecules and appears in the frequency region where the O–H stretches of the water molecules in solid ice show their

infrared transitions.<sup>44</sup> Earlier dilution work with PC/PG lipids identified SFG signal contributions at  $\sim 3,100\text{ cm}^{-1}$  to be specific to PC...H<sub>2</sub>O interactions.<sup>34</sup> A smaller peak, at  $\sim 3,400\text{ cm}^{-1}$  is also observed in the spectrum and is attributed to the weakly bonded water molecules above the 9:1 DMPC: DMPG bilayer.<sup>45-47</sup> Figure 3.4A shows that adding PAH results in a signal intensity decrease across the O-H stretching region probed here. At 0.1 mM PAH this loss is  $\geq 70\%$  of the original SFG signal intensity. As the stronger H-bond network, observed at  $\sim 3,200\text{ cm}^{-1}$ , is seemingly disrupted by PAH, one may expect an increase in the weaker H-bonding region ( $\sim 3,400\text{ cm}^{-1}$ ), however, this is not the case. Instead, the decrease in intensity in the  $3,200\text{ cm}^{-1}$  and the  $3,400\text{ cm}^{-1}$  regions suggests a direct displacement of the water molecules by PAH. The same trend is also seen in Figure 3.4B for another negatively charged bilayer composed of a 9:1 mix of DMPC:DMPS lipids, in which the PS headgroup is less shielded than in PG.

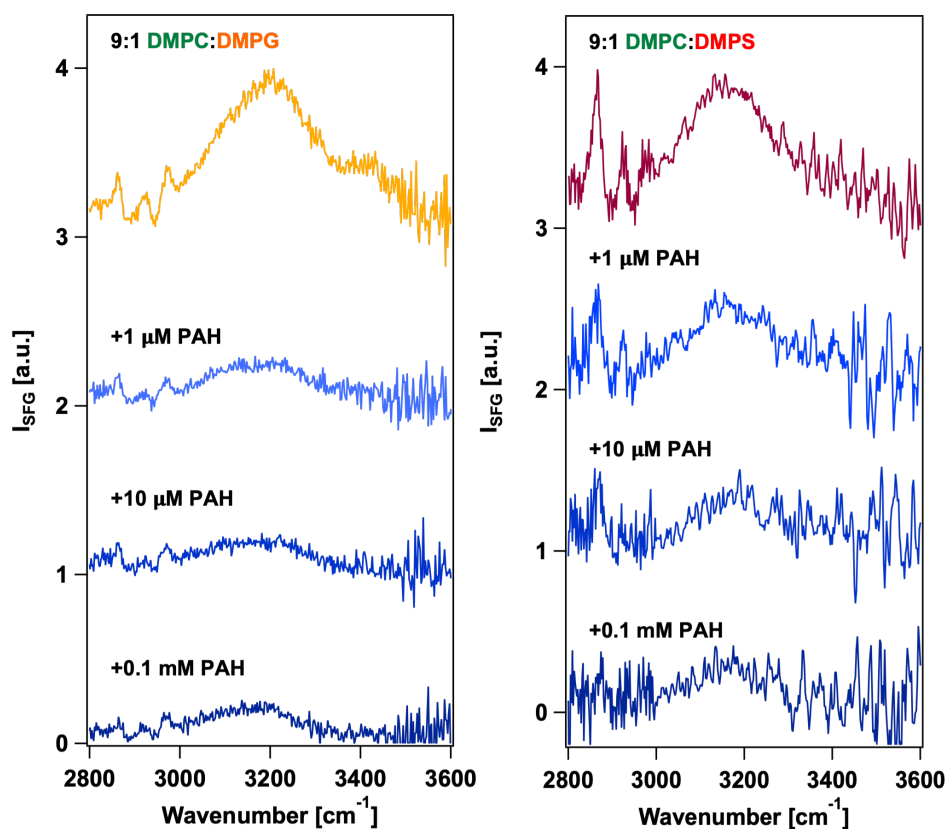


Figure 3.4. Representative SSP-polarized SFG spectra for a bilayer formed from (A) a 9:1 mixture of DMPC:DMPG lipids (orange) and (B) a 9:1 mixture of DMPC:DMPS lipids (red) in buffer solution composed of 0.01 M Tris and 0.1 M NaCl, adjusted to pH 7.4 before interaction with PAH and after the interaction of the SLB with PAH in increasing concentrations: 1 μM (light blue), 10 μM (blue), and 0.1 mM (dark blue). All spectra in (B) have been binned over three points in x and y between 3,000 cm<sup>-1</sup> — 3,600 cm<sup>-1</sup> for clearer S/N resolution.

### 3.3.2. Membranes Formed from Zwitterionic Lipids Show Slight Displacement of Interfacial Water

Adding PAH to a bilayer formed from purely zwitterionic DMPC elicits two types of outcomes that fall into a majority category showing little ( $\leq 30\%$ ) to no change to the lipid or water signals upon addition of up to 0.1 mM PAH after which signal intensities drop mainly in the C–H stretching region and to some degree in the O–H stretching region at 1 mM PAH (Figure 3.5A, observed 4 out of 6 times). These changes in the SFG lineshapes at high PAH concentration are likely due to specific water/ion interactions with the lipids, as controls carried out at 300 mM [salt], which corresponds to the total ionic strength at 1 mM PAH ( $\sim 160$   $-\text{NH}_3^+$  repeat units) in 100 mM NaCl is  $\sim 300$  mM (*vide infra*) (Figure 3.6D). The minority response (Figure 3.5B, observed 2 out of 6 times) is characterized by noticeable SFG intensity reduction/elimination in the C–H stretching region at PAH concentrations as low as 10  $\mu\text{M}$ , along with considerable signal reductions around  $3,200\text{ cm}^{-1}$ , albeit to a lesser extent when compared to the negatively charged bilayers (Figure 3.4).

We attribute the differences we observe in the PAH-membrane interactions described here to how strongly water molecules are bound to the lipid headgroup and to the strength of the electrostatic PAH-membrane interactions. First, the cationic nature of PAH favors interactions with the overall negatively charged membranes, as is indeed observed here in our majority responses. The carboxylate moiety in the PS headgroup is likely parallel to the other lipids comprising the membrane and is therefore readily accessible to cationic PAH (this is also likely for the PG headgroup due to the condensing effect, described

below).<sup>48</sup> Moreover, water is also expected to bind more strongly to the amine and carboxylate groups on PS when compared to the more shielded, less accessible, negatively charged phosphate moiety, where most H-bonding occurs for PC lipids.<sup>49</sup> Regarding the strength with which water molecules are bound to the lipids, we refer to computer simulations by Berkowitz and coworkers<sup>50,51</sup> showing that the area per headgroup is smaller for PS lipids than for PC due to intermolecular H-bonding of the amine and carboxylate moieties (Figure 3.1B, known as the “condensing effect”).<sup>48,49</sup> Intermolecular lipid-lipid interactions are also possible for PG bilayers, in which the glycerol moieties H-bond with the ester carbonyl group, likely decreasing the available area per headgroup and thus the number of bound water molecules.<sup>52,53</sup> Conversely, more water molecules surround PC headgroups than PG or PS.

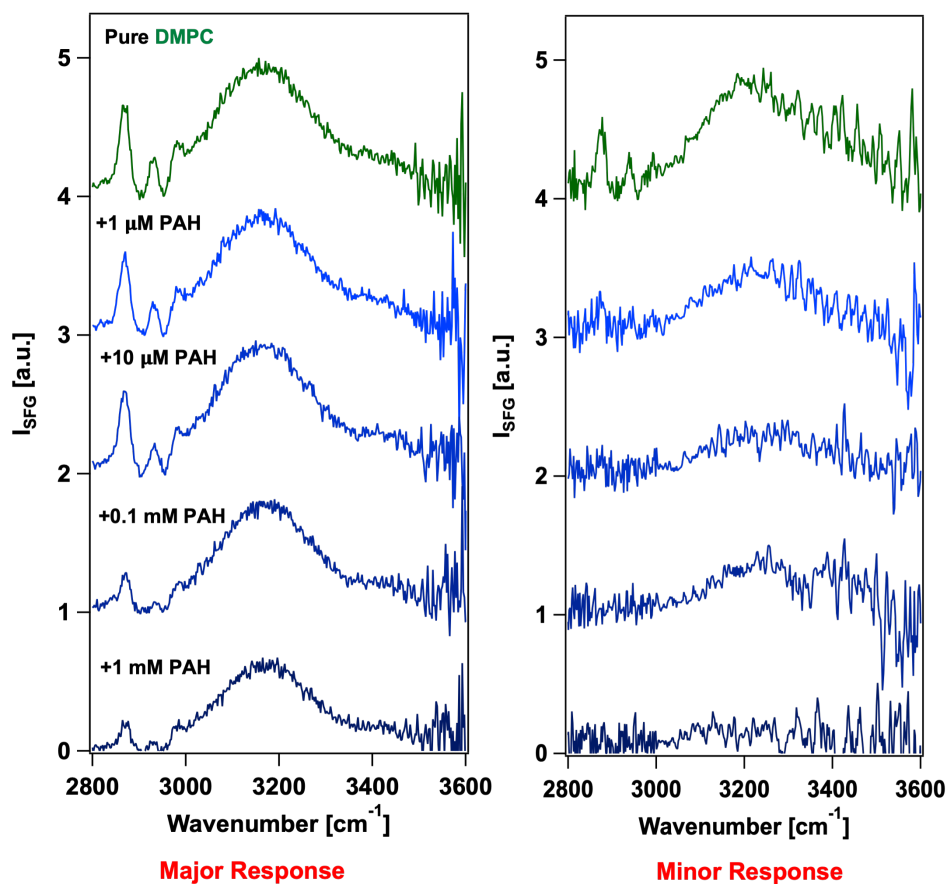


Figure 3.5. SSP-polarized SFG spectra for (A) major and (B) minor responses for the interaction of PAH with a bilayer formed from 100% DMPC lipids in buffer solution composed of 0.01 M Tris and 0.1 M NaCl, adjusted to pH 7.4 before interaction with PAH (green). The spectra taken after the interaction of the SLB with PAH in increasing concentrations: 1  $\mu\text{M}$  (light blue), 10  $\mu\text{M}$  (blue), 0.1 mM (dark blue), and 1 mM (navy). The spectra for (B) have been binned over three points in  $x$  and  $y$  between  $3,000\text{ cm}^{-1}$  –  $3,600\text{ cm}^{-1}$  for clearer S/N resolution and comparison with the major response.

### 3.3.3. Membrane Water is Irreversibly Displaced by PAH

Rinsing the PAH-exposed membranes with calcium-free buffer showed no signal intensity recovery in the H-bonding network or the C–H oscillators (Figures 3.6A–C). While irreversibility is only shown for the major response for the pure DMPC bilayer, it was also observed for the minority response. These results support the notion that the PAH polycations have irreversibly displaced the interfacial water molecules.<sup>42</sup>

Because the ionic strength of 1 mM PAH (0.3 M) is approximately  $3\times$  higher than our original buffer solution (0.1 M), a control experiment was carried out to determine whether the changes in the H-bonding network was due to the PAH interaction or ionic strength. Figure 3.6D shows only negligible changes in the O–H stretching region when the salt concentration is raised from 0.1 to 0.3 M. This outcome is consistent with negligible absorptive-dispersive mixing between the second-order ( $\chi^{(2)}$ ) and the surface potential-dependent third-order contribution ( $\chi^{(3)}\Phi(0)$ ) to the SFG signal generation process, according to<sup>28,29,34,54–56</sup>

$$(3.3.1) \quad \chi_{\text{total}}^{(2)} = \chi^{(2)} + \cos(\varphi_{\text{DC}})e^{i\varphi_{\text{DC}}}\chi^{(2)}\Phi(0)$$

Here,  $\varphi_{\text{DC}}$  is the optical phase angle (the “DC phase angle”)<sup>56</sup> associated with the electrostatic potential produced by the interfacial charges. For electrical double layer model in which the surface potential decays exponentially into the bulk aqueous phase,  $\varphi_{\text{DC}} = \arctan(\Delta k_z \lambda_D)$ , where  $\Delta k_z$  is the wave vector mismatch ( $\sim 1.1 \times 10^{-7} \text{ m}^{-1}$  in our experimental setup)  $\lambda_D$  is the Debye length in the diffuse layer, which depends on the ionic strength. At  $>100 \text{ mM}$  [salt],  $\varphi_{\text{DC}}$  is  $\sim 0^\circ$ <sup>34</sup> and model (1) becomes purely additive

in  $(\chi^{(2)})$  and  $(\chi^{(3)}\Phi(0))$ . Figure 3.6D is consistent with this model. While we observe no significant change in O–H stretching region as [salt] goes from 0.1 to 0.3 M, we observe an SFG signal intensity decrease in the C–H stretching region, which we attribute to the onset of specific binding of  $\text{Na}^+$  to the oxygen atoms in the lipid headgroups at these high salt concentrations, as shown by Cordomi et al. at 0.2 M NaCl.<sup>57</sup>



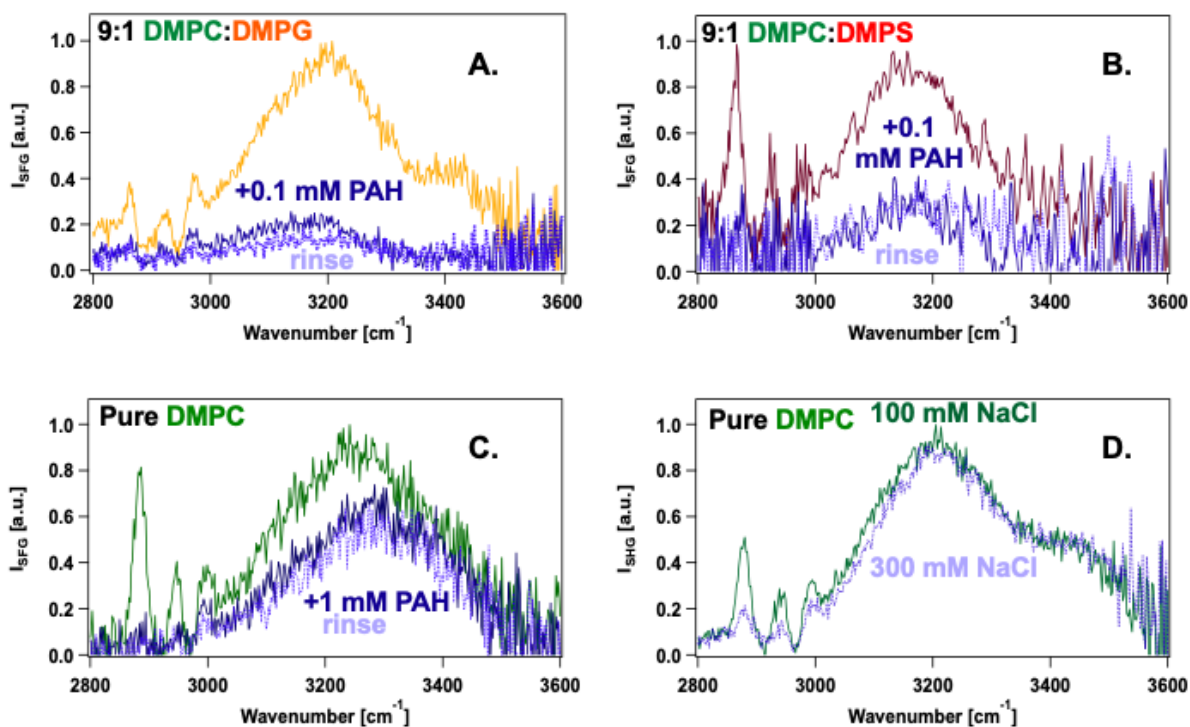


Figure 3.6. Interaction of a bilayer formed from (A) a 9:1 mixture of DMPC:DMPG lipids (orange) and (B) a 9:1 mixture of DMPC:DMPS lipids (red) with the highest concentration of PAH studied, 0.1 mM (dark blue), and after rinsing with 20 mL of PAH-free buffer solution (dotted blue line). The spectra for (B) have been binned over three points in  $x$  and  $y$  between  $3,000\text{ cm}^{-1}$  –  $3,600\text{ cm}^{-1}$  for clearer S/N resolution and comparison with other reversibility traces. (C) Interaction of a bilayer formed from 100% DMPC lipids (green) with the highest concentration of PAH studied, 1 mM (navy), and after rinsing with 20 mL of PAH-free buffer solution (dotted blue line). (D) A bilayer formed from 100% DMPC lipids (green) after rinsing with buffer solution composed of 0.01 M Tris and 0.3 M NaCl, adjusted to pH 7.4.

### 3.3.4. Contact-Ion Pair Formation

Prior work has shown that only a small number of monomeric units of PAH, allylamine hydrochloride (AH), directly interact with the 9:1 DMPC:DMPG bilayer surface. Therefore, PAH likely adopts a loosely bound vertical “loop-like” conformation which could lead to the drawing in of counterions to lower charge-charge repulsion between the neighboring positively charged subunits. This binding mode, as commonly seen for polymers at surfaces, allows the polymer to adopt multiple configurations and therefore is entropically more favorable than the binding mode in which the polymer remains flat on the membrane surface. Atomistic simulations indicate that the interaction involves direct amine-phosphate interaction rather than indirect hydrogen-bonding mediated by water molecules. Therefore, the displacement of water molecules mentioned above could possibly be due to new hydrogen-bond formation via contact-ion pair formation. This is expanded upon in Chapter 4.

## 3.4. Conclusion

We have shown the perturbation of the H-bonding network of bilayers formed from 100% zwitterionic DMPC as well as from 9:1 mixes of DMPC:DMPG and DMPC:DMPS with the addition of the common cationic polymer PAH in 100 mM NaCl. At 0.1 mM, PAH binds irreversibly to the bilayers that contain the negatively charged PG and PS lipids and displace interfacial water molecules, as revealed by vibrational sum frequency generation spectroscopy. 10 times higher PAH concentrations are required to displace water molecules from the purely zwitterionic bilayer. This outcome is likely due to difference in (1) the energy with which water molecules are bound to the lipid headgroups,

(2) the number of water molecules bound to the headgroups, which is related to the headgroup area, and (3) the electrostatic interactions between the PAH molecules and the negatively charged lipids that are favored when compared to the zwitterionic lipid headgroups. The interactions between the polycations and the membranes were further analyzed in reversibility studies that revealed no SFG signal intensity recovery upon rinsing for all PAH-exposed membranes surveyed. The irreversibility of PAH attachment can have significant effects on cell function, as osmosis and membrane diffusion are expected to be altered without access to membrane water molecules or solvated ions. As PAH is continued to be used in nanomaterials and as thin films for biomaterials, it is important to note the toxic outcomes large quantities of PAH can have on biological systems. Taken together, then, it is our hope that our insights will help establishing causal relationships in nanotoxicology, and contribute to understanding, controlling, and predicting the initial steps that lead to the lysis of cells exposed to membrane disrupting polycations.

## CHAPTER 4

**Summary and Future Work: Electrostatics, Hydrogen-Bonding,  
and Molecular Structure at Polycation and Peptide: Lipid  
Membrane Interfaces**

Portions of this chapter are reproduced in part with permission from the  
American Chemical Society:

Dalchand, N.; Cui, Q.; Geiger, F. M., Electrostatics, Hydrogen Bonding, and Molecular  
Structure at Polycation and Peptide: Lipid Membrane Interfaces. *ACS Appl. Mater.*

*Interfaces* **2019**, 12, 21149–21158.

## 4.1. Introduction to Chapter 4

In Chapter 3, the dehydration of supported lipid bilayers (SLBs) with the addition of poly(allylamine hydrochloride) (PAH) was determined for both zwitterionic and negatively charged bilayers. The conclusions drawn in this work build on the previous conclusions from work done in our group. To this end, a summary and review of the work done in our group exploring the electrostatics, hydrogen-bonding, and molecular structure at polycation and peptide:lipid membrane interfaces is provided in this chapter. Future experiments exploring membranes integrated with model ion channels such as gramicidin A are also proposed.

## 4.2. Background

The significance of positive charges of polymers, peptides, and surfactants for biocidal uses is well-known.<sup>1-4</sup> When in contact with a surface modified with these cationic species, the plasma membrane of bacteria and other microorganisms can rupture due to the resulting disorder of the membrane in a series of processes that are only now beginning to be understood on the molecular level. Moreover, membrane penetration by polycations is key to various biological processes such as transfection of small molecules and DNA into cells for applications such as drug and gene delivery.<sup>5</sup> For instance, compounds possessing quaternary ammonium groups exhibit charge-density thresholds for optimal biocidal function, as reported by Kügler et al.<sup>3</sup> Surpassing or, alternatively, staying below this threshold requires reliable estimates of polycation surface coverage and charge density and well as information regarding molecular structure at the polycation:lipid membrane

interface. This information is not straightforward to obtain, as the charge state of interfacial peptides and polycations can differ considerably from the one they assume in bulk water. As we will show herein, interfacial structure and molecular environment at the polycation and peptide:membrane interface are the key determinants for this difference. Access to such information opens possibilities to control, understand, and optimize the polycation-surface interaction to desired performance levels without perhaps having to rely on costly chemical library screens.

Here, we highlight our recently developed approach to quantify the charge density of a suite of polycations and peptides shown in Figure 4.1 at the interface of aqueous solutions and supported lipid bilayers (SLBs). Furthermore, we assess changes to the hydrogen bonding network due to polycation addition as water is an essential component of bacterial media and biochemical systems and reactions. We combine the second-order nonlinear spectroscopic technique second harmonic generation (SHG) with mass estimates from quartz crystal microbalance measurements with dissipation monitoring (QCM-D) in order to determine the charge per adsorbate on the membrane surface. These experiments are interpreted using atomistic simulations and followed by vibrational sum frequency generation (SFG) spectroscopy to assess the perturbation of the hydrogen bonding network above our membrane system with the addition of polycations.

The combination of the various techniques mentioned is necessary, highlighting that determining surface charge density is not trivial, especially for soft matter aqueous interfaces like the ones investigated here. Methods for determining electrostatics at aqueous interfaces in a single step do exist in the form of electrokinetic measurements,<sup>6-10</sup> but the task of connecting the electrostatic potential at the  $\zeta$ -plane (“slipping-plane”) with

that at the zero plane (e.g.  $\phi_0$ ) and the electrical dipole potential<sup>11,12</sup> to inform on interfacial charge densities remains a major challenge.<sup>6,7,13</sup> This latter potential is important for many uncharged (neutral, zwitterionic) interfacial systems and can be on the order of several 100 mV at lipid monolayers.<sup>14</sup> Compounding the problem is that additional unknowns exist regarding the microscopic structure, including wide ranges of the relative permittivity in the interfacial region<sup>15-22</sup> of the Electrical Double Layer (EDL).

Finally, conversion from  $\zeta$ -potential to interfacial charge density at the zero plane requires several approximations that may not be appropriate for soft interfaces with a significant degree of spatial heterogeneity at the molecular scale.<sup>23</sup> Another useful technique in determining surface charge, scanning probe microscopy,<sup>24</sup> has been successfully paired with finite-difference analysis<sup>25</sup> and extended to individual molecules<sup>26</sup> to obtain estimates for  $\Phi(0)$  and  $\sigma$ , but this approach requires the presence of a possibly perturbative measuring probe and only provides the interfacial electrostatic parameters at specific  $x$ - $y$  coordinates one force-distance curve at a time, resulting in lengthy data acquisitions. Our approach circumvents these limitations, as SHG and SFG spectroscopies are non-destructive and do not require the use of fluorescent probes or other surface modifications.

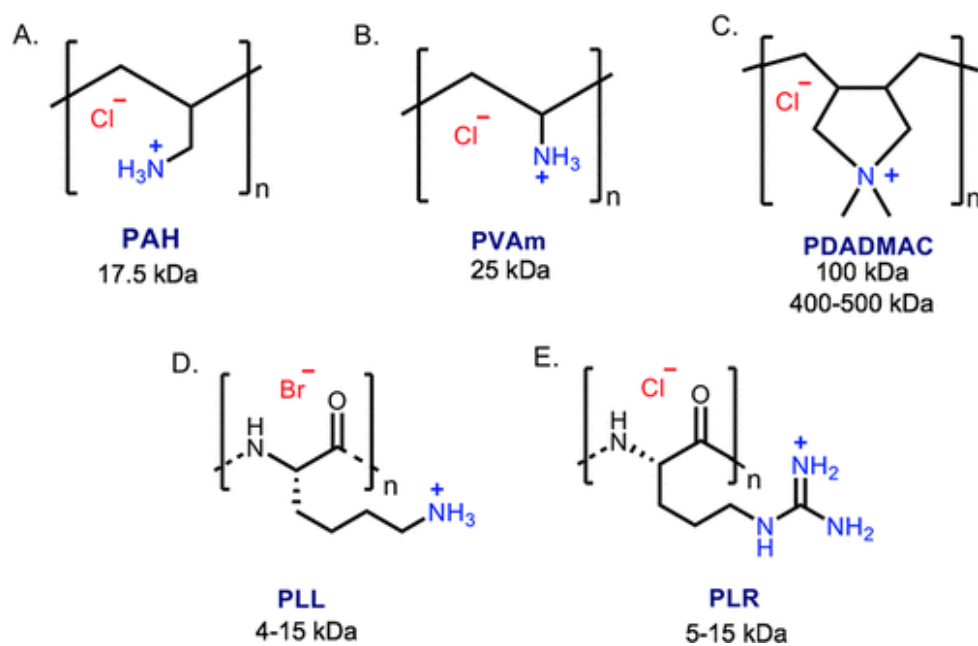


Figure 4.1. A compilation of the structures of the polycations used in our work: (A) poly(allylamine hydrochloride) (PAH), (B) poly(vinylamine hydrochloride) (PVAm), (C) poly(diallyldimethylammonium chloride) (PDADMAC), (D) poly-L-lysine (PLL), and (E) poly-L-arginine (PLR). The molecular weight of each polycation used is listed under the corresponding structure. The peptides surveyed,  $\text{Lys}_8$  and  $\text{Arg}_8$ , have the same functional groups as their polycation counterparts in (D) and (E) respectively.



### 4.3. The Optical Voltmeter

SHG spectroscopy is a process in which two photons of the same frequency combine to produce a beam that is twice the frequency.<sup>27,28</sup> It is surface selective and is forbidden in centrosymmetric media and thus only reports on regions where symmetry is broke, i.e., at the interface. For surfaces carrying an electrostatic potential, equation 4.3.1 expresses the overall signal intensity,  $I_{\text{SHG}}$ , as<sup>29-31</sup>

$$(4.3.1) \quad \sqrt{I_{\text{SHG}}} \propto \chi^{(2)} E_{\omega} E_{\omega} + \chi^{(3)} E_{\omega} E_{\omega} \int_0^{\infty} E_{\text{DC}}(z) e^{i\Delta k_z z} dz$$

Here,  $\chi^{(2)}$  and  $\chi^{(3)}$  are teh second- and third-order nonlinear susceptibility tensors,  $E_{\omega}$  is the incident electric field,  $E_{\text{DC}}$  is the electrical field produced by charges at the interface, where  $E_{\text{DC}} = -\nabla_z \Phi$ , with  $\Phi(z)$  being the electrostatic potential falling off with distance,  $z$ , and  $\Delta k_z$  is the wavevector mismatch, which depends on the optical geometry, wavelengths, and bulk dielectric constants. Note that  $\Phi(0)$  is the total surface potential given by the sum of the Coulomb and dipole potential terms. Equation 4.3.1 can be simplified by approximating  $\chi^{(2)}$ ,  $\chi^{(3)}$ , and  $E_{\omega}$  to be constants so that one finds

$$(4.3.2) \quad E_{\text{SHG}} = A + B\Phi(0) \frac{\kappa}{\kappa - i\Delta k_z}$$

Here,  $\kappa$  is the inverse screening length, which is determined by the ionic strength in the bulk aqueous solution. Equation 4.3.2 directly relates the interfacial potential,  $\Phi(0)$ , to the SHG response, rendering the method an "optical voltmeter." In the Outlook section, we will show how a recently developed approach using hetrodyne detection directly yields the phase and amplitude of the SHG response, which is then used to obtain the second-order

nonlinear susceptibility tensor and the surface potential, including its sign, directly and without further simplifying assumptions or prior knowledge of interfacial electrostatics at the membrane.

Our experiments are carried out at 0.1 M [NaCl], for which the value of the phase-matching term,  $\frac{\kappa}{\kappa - i\Delta k_z}$ , approaches unity.<sup>29–32</sup> At low [NaCl] (< 0.1 M), this term must be accounted for due to absorptive-dispersive mixing between the second-order ( $\chi^{(2)}$ ) and the surface potential-dependent third-order contributions ( $\chi^{(3)}\Phi(0)$ ). The assumptions underlying this technique are as follows: (a) the nonlinear optical signal recorded at the detector consists of only 2<sup>nd</sup> and 3<sup>rd</sup> order terms, (b) the surface potential decays somehow with distance, and (c) the Debye–Hückel theory is applicable for the bulk aqueous phase, which is a reasonable assumption below  $\sim 0.1$  M ionic strength. Our recent work also evaluates linearly decaying potentials,<sup>33</sup> which may be of interest in crowded environments, such as mitochondria.

To determine surface charge densities,  $K_{\text{ads}}$  and  $\Delta G_{\text{ads}}$ , a combined electrostatic model (Gouy–Chapman) and adsorption model (Langmuir) is substituted for the interfacial potential in Equation 4.3.2 to produce

$$(4.3.3) \quad \sqrt{I_{\text{SHG}}} \propto A + B \sinh^{-1} \left( \sigma_0 + \frac{\sigma_{\text{ads}} K_{\text{ads}}}{1 + K_{\text{ads}}} \right) \times \frac{8.44 (\text{mol } l^{-1})^{-\frac{1}{2}} m^2 C^{-1}}{\sqrt{M + C_{\text{elec}}}}$$

Here, the total surface charge density is described by  $\sigma_0 + \sigma_{\text{ads}}$ , where  $\sigma_0$  is the surface charge density of the bare bilayer used, in this case,  $-0.1 \text{ C/m}^2$  for a bilayer prepared from a 9:1 mix of 1,2-Dimyristoyl-*sn*-glycero-3-phosphocholine (DMPC, zwitterionic) and 1,2-dimyristoyl-*sn*-glycero-3-phospho-(1-*rac*-glycerol) (DMPG, negatively charged), and  $\sigma_{\text{ads}}$  is the surface charge density of the layer of adsorbed species, in this case the polycations

or peptides.  $K_{\text{ads}}$  is the equilibrium binding constant for polycation or peptide adsorption in units of  $1 \text{ mol}^{-1}$ , and  $C_{\text{elec}}$  is the bulk electrolyte concentration ( $0.1 \text{ mol l}^{-1}$ ). The units in the numerator of the right-most factor ensure that surface charge density estimates are provided in  $\text{C m}^{-2}$ . The Hill adsorption model is an extension of the Langmuir model and can be substituted into the Gouy–Chapman expression as well. It is well written as  $\theta = K_{\text{ads}}^n M^n / (1 + K_{\text{ads}}^n M^n)$ . The Hill coefficient,  $n$ , describes the extent of cooperativity of binding, where  $n > 1$  means that increasing the concentration of the adsorbate also increases the affinity of binding. In this scenario, binding is cooperative.<sup>34</sup> When  $n < 1$ , anti-cooperative behavior is observed, meaning the affinity for binding decreases with an increasing concentration of adsorbate. Alternatively, adsorption to structurally or chemically heterogeneous surfaces can also result in artificially low  $n$  values,<sup>35,36</sup> while electrostatics and reductions in dimensionality can explain high values of  $n$ .<sup>37</sup> In the work discussed here, the combined Gouy–Chapman/Langmuir and the Gouy–Chapman/Hill models were used to extract the equilibrium binding constant, the free energy of adsorption, and the interfacial charge density and charge per adsorbed polycation or peptide.

#### 4.4. Atomistic and Coarse-Grained simulations

With molecular simulations, it is relatively straightforward to simulate the binding mode(s) of short peptides and oligomers to lipid membrane surfaces, providing information regarding their conformational distributions, hydration state, and interactions with lipid molecules and salt ions at the interface.<sup>38–40</sup> More quantitative computations of binding, such as binding free energy and actual spectroscopic parameters, remain limited to

relatively simple cases;<sup>40,41</sup> this is because quantitative free energy and spectroscopic computations are more sensitive to technical details such as electronic polarization and the degree of conformational sampling. For the binding of polymers of higher molecular weights, atomistic simulations remain challenging due to the difficulty of adequately sampling the conformational space of the polymer, especially at the membrane/water interface. Moreover, the titration state of the polymer may change upon binding, a phenomenon that has been noted yet not extensively explored for non-biological polymers.<sup>42–44</sup> Therefore, coarse-grained simulations are often needed for probing the interaction between polymers and lipid membranes, for which calibration is essential but not always straightforward.<sup>45–47</sup> Nevertheless, in general, atomistic and coarse-grained simulations can provide molecular level information that is valuable to the interpretation of the spectroscopic (SFG, SHG) and QCM-D data, as we discuss below. In addition, the microscopic information for the interface from molecular simulations enables one to test the validity of approximations in commonly used models for the extraction of molecular-level parameters, such as the Gouy–Chapman model<sup>48</sup> for converting measured surface potential to an apparent surface charge (*vide infra*).

#### 4.5. Sub-Charging at High Surface Densities of Polycations

Our first studies assessed the adsorption of the polycation poly(allylamine) hydrochloride (PAH) to a supported lipid bilayer (SLB) formed from a 9:1 mixture of zwitterionic DMPC and negatively charged DMPG lipids. SLB’s are formed using the vesicle fusion method on fused silica substrates.<sup>49–52</sup> In this planar, flat geometry, out of plane deformations (bending/curling) by electrostatic forces, which would distort the interface, are

unlikely to be probed by our methods, and require, for instance, scanning probes instead. At the ionic strength of the experiment (0.1 M salt), the free energy of binding estimated from fitting a combined Gouy–Chapman/Langmuir model to the isotherm was  $-52.7 \pm 0.6$  kJ/mol shown in Figure 4.2A. Under salt-free conditions, the estimated free energy of binding is  $-50$  kJ/mol as shown by Figure 4.2B. Figure 4.2B also shows that under the same salt-free conditions, the adsorption of the monomeric unit of PAH, allylamine hydrochloride (AH), on a 9:1 DMPC: DMPG bilayer showed a clear shift in the inflection point, with an extracted free energy of only  $-14.6 \pm 0.4$  kJ/mol,<sup>50</sup> a mere 3 times less than that observed for PAH. If the values of  $\Delta G_{\text{ads}}$  of the monomers were additive, we would expect a  $\sim 100$  times greater adsorption free energy for PAH, considering it has 190 charged units (n.b.: our SHG and QCM-D measurements indicate that only 70% of the 190 units are charged and even then,  $\Delta G_{\text{ads}}$  for the PAH is much lower than expected). To explore this result further, we carried out coarse grain simulations of PAH<sub>10–160</sub> interacting with the bilayer and gained qualitative insight on the mechanisms of binding occurring at the surface. These simulations indicate that PAH prefers a loosely bound conformation in which only a small number of the AH monomeric units directly interact with the bilayer surface (Figure 4.3A–B). This binding mode, as commonly seen for polymers at surfaces,<sup>53</sup> allows the polymer to adopt multiple configurations and therefore is entropically more favorable than the binding mode in which the polymer remains flat on the membrane surface. Furthermore, the simulated titration curve (Figure 4.3C) shows that as the amount of PAH present at the bilayer surface increases to high coverage (as shown schematically with a packing model based on the surface density observed experimentally in Figures 4.3A–B), the pKa of the amine groups along the polymer shifts due

to increased crowding to lower charge-charge repulsion. This interpretation is suggested by the change in the fraction of protonated amine groups at different polycation densities. For example, at high surface densities of PAH, the fraction of protonated amine groups is 20% at a pH of 7, however, at moderate coverage the fraction of protonated amine groups is 50% (Figure 4.3C). The estimated fraction of protonated amine groups is substantially lower than the experimental observation due in part to the simplicity of the packing model; moreover, the QCM-D data included contributions from interfacial water molecules and counterions and therefore likely overestimated the binding density of the PAH at the membrane surface.

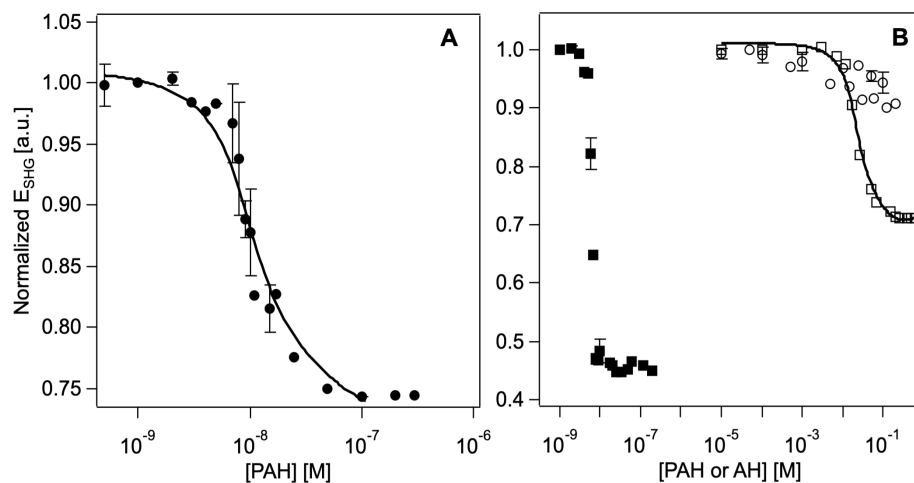


Figure 4.2. SHG adsorption isotherms for (A) PAH (●) at 0.1 M NaCl and (B) AH (○) at 0.1 M NaCl. (B) also shows PAH (■) and AH (□) at low ionic strength conditions, 0 M NaCl. All solutions were prepared to produce a buffer solution containing 0.01 M Tris at a pH 7.4. The black lines in (A) and (B) represent the data that was fit to the double layer model. Reprinted with permission from ref 50. Copyright 2017 ACS Publications.

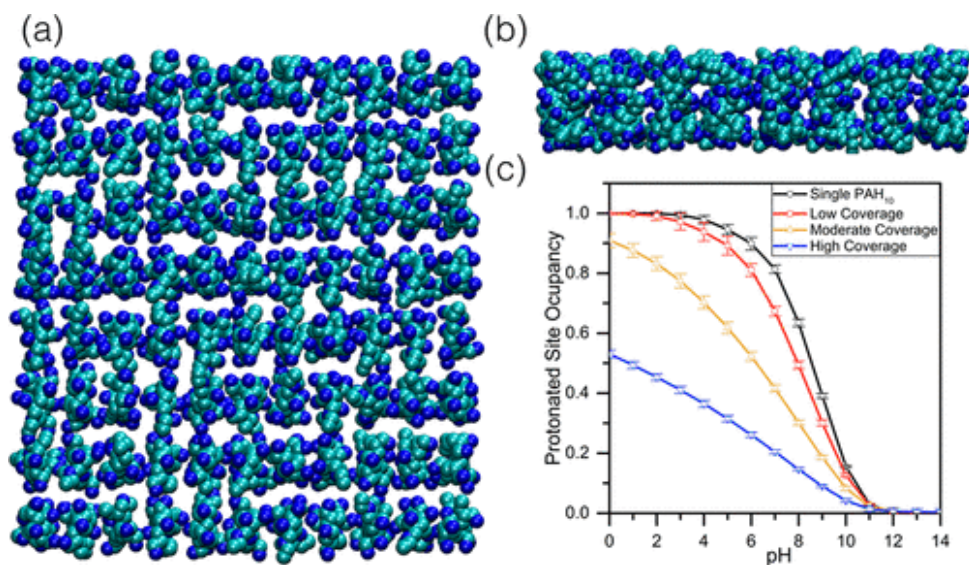


Figure 4.3. The top (A) and side view (B) of the surface-packing model for PAH<sub>10</sub> at the lipid bilayer surface. Here, only one AH monomer is in direct contact with the surface. The following MCCE calculations in (C) show a computed titration curve for different surface binding densities, where there is a notable decrease in protonated surface sites as more PAH<sub>10</sub> is added on the bilayer surface. Reprinted with permission from ref 50. Copyright 2017 ACS Publications.



#### 4.6. Contact-Ion Pair Formation

In addition to pKa shifts, the difference in charge state of the monomers vs. the polymers may also be due to contact-ion pair formation between the protonated amine groups and the phosphate moieties on the lipid headgroup shown in Figure 4.4. Our atomistic simulations indicate that the interaction involves direct amine-phosphate interaction rather than indirect hydrogen-bonding mediated by water molecules. The size of the polycation and configurational entropy considerations<sup>53</sup> indicate that the formation of loops may be important, which could lead to the drawing in of counterions to lower charge-charge repulsion between the neighboring positively charged subunits. In this scenario, few protonated amine groups come into contact with the lipid headgroups, whereas more than one AH monomer can bind to each lipid headgroup when considering the AH monomer alone.

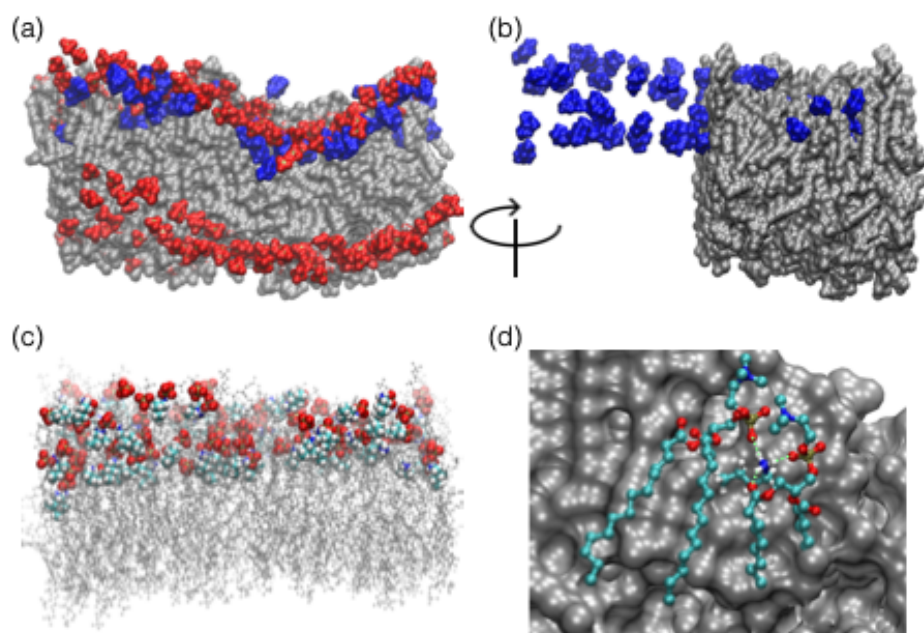


Figure 4.4. Atomistic simulation of AH monomers (320) interacting with a bilayer formed from a 9:1 mixture of DMPC: DMPG lipids. (A) Significant undulation to the molecular surface of the bilayer (gray) is shown upon AH (blue) binding. The phosphate moieties of the lipid head groups are also shown (red) to highlight where bonding is taking place. (B) shows a  $90^\circ$  rotation of (A) about the  $z$ -axis and (C) presents an atomistic view of (A). (D) represents the hydrogen-bonding interactions (green dotted lines) between an AH monomer with the negatively charged portions of adjacent lipids, the phosphate and glycerol groups. Adapted with permission from ref 50. Copyright 2017 ACS Publications.

## 4.7. Perturbation of the Hydrogen-Bonding Network with Added Polycations

### 4.7.1. Vibrational Sum Frequency Generation Spectroscopy

SFG spectroscopy, like SHG spectroscopy, is a nonlinear optical technique. It combines a tunable infrared and fixed visible beam temporally and spatially to produce a beam at the sum of the two frequencies. This technique has been used extensively to identify bilayer structure<sup>49,54</sup> and structural changes to lipid bilayers such as lipid asymmetry<sup>55–57</sup> as well as the kinetics and thermodynamics of processes such as lipid flip-flop,<sup>58,59</sup> pioneered by Conboy and co-workers. SFG spectroscopy also provides information about the interfacial hydrogen bond network<sup>52,60–62</sup> above the bilayer surface, which is important for garnering a complete understanding of the mechanism associated with peptide or polycation:membrane interactions.

Our initial efforts in probing this region involved understanding the water structure above the EDL under conditions of high and low ionic strength. We found that increasing the ionic strength from 10  $\mu\text{M}$  to 0.1 M results in SFG signal intensity reductions. Yet, atomistic simulations carried out at 0 M and 0.15 M salt concentration tracking the O $\cdots$ O distances between neighboring water molecules as well as dipole moment orientation distributions showed no significant changes in the hydrogen-bonding network.<sup>52</sup> Therefore, we concluded the changes in the SFG spectral lineshape due to ionic strength are indicative of absorptive-dispersive mixing between  $\chi^{(2)}$  and  $\chi^{(3)}$  contributions at the charged interface. This type of optical mixing has only been considered recently in regards to the SFG community.<sup>29–32</sup> As our experiments are largely carried out at high ionic strength

(0.1 M NaCl), where the addition of polycations (PAH in this case) does not change the ionic strength considerably, we conclude that any changes to the SFG spectral lineshape due to PAH adsorption can be interpreted to report on changes in the hydrogen-bonding network that directly result from polycation:membrane interactions and not changes in ionic strength, as the next section will further elaborate.

#### 4.7.2. Water Expulsion Upon Polycation Absorption

At high densities of PAH at the bilayer surface, we saw changes in pKa of the primary amine group due to crowding. To lower charge-charge repulsion, PAH draws in counterions and adopts “vertical packing”, as mentioned. In order to gain further insight into the mechanisms of PAH binding to the bilayer surface, our most recent work considered the role of the interfacial water molecules present at the bilayer surface. To summarize, in Chapter 3 we saw that after 1  $\mu$ M PAH is added to the 9:1 DMPC: DMPG bilayer, the SFG signal intensity decreases near  $3,200\text{ cm}^{-1}$  and  $3,400\text{ cm}^{-1}$ , which are assigned to strongly and weakly bonded hydrogen bonds networks respectively.<sup>63</sup> With the breaking of strong hydrogen bonds, we would perhaps expect an increase in the weaker ones, but an increase in the peak at  $3,400\text{ cm}^{-1}$  is not apparent. Instead, our observations are consistent with the notion that PAH displaces the interfacial water molecules. This expulsion of water molecules at the interface could be due to new hydrogen bond formation via the contact-ion pair formation mechanism discussed earlier. As the PAH concentration is further increased to 10  $\mu$ M and 0.1 mM, the resulting SFG signal intensity reduction across the hydrogen-bonding network exceeds 70 %.<sup>51</sup>

The reversibility of the displacement of interfacial water molecules with PAH was assessed by rinsing the bilayer with PAH-free buffer. After rinsing, the spectral features of the bilayer in the C–H stretching region do not revert, neither do the peaks at  $3,200\text{ cm}^{-1}$  or  $3,400\text{ cm}^{-1}$ , consistent with the possibility that water repulsion induced by PAH is irreversible under our experimental conditions. The experiment was also performed with another negatively charged bilayer that includes the lipid 1,2-dimyristoyl-sn-glycero-3-phospho-L-serine (DMPS). Again, the peaks in the C–H and O–H stretching regions do not revert upon rinsing. Therefore, regardless of the lipid headgroup structure, the negatively charged bilayers remain dehydrated with the addition of PAH. This leads us to question whether water expulsion for supported lipid bilayers is a necessary first step for the subsequent membrane disruption by polycations and is a question we wish to explore in future work.

#### 4.8. Cationic Polymers at Lipid Bilayer Surfaces

In contrast to the large polycations, the interaction of the short oligomers Arg<sub>8</sub> and Lys<sub>8</sub> with the 9:1 DMPC: DMPG bilayers was also evaluated. These peptides were found to be fully ionized when attached to the bilayer. The combined Gouy–Chapman/Hill model was fit to the adsorption isotherms for these octamers, yielding an  $n$  of 0.5 for both. This result is contrary to a recent report by Cremer and Jungwirth and co-workers, who reported the degree of cooperativity to be significantly different between Arg<sub>9</sub> and Lys<sub>9</sub>.<sup>38</sup> This different outcome may be attributed to the fluorescent labelling of the lipid bilayers used in their experiments as well as the difference in fluidity between our 9:1 DMPC: DMPG bilayer system and their 9:1 POPC: POPG bilayer system.

Simulations shown in Figure 4.5 show that the guanidinium group on the arginine side chain can hydrogen bond to both the glycerol and phosphate groups in the lipids whereas the primary amine group on lysine forms a localized hydrogen bond with the phosphate group.<sup>46</sup> This difference leads to substantially different binding modes of Arg<sub>8</sub> and Lys<sub>8</sub> peptides: Arg<sub>8</sub> inserts more deeply into the bilayer to form a “buried” conformation, interacting with the lipids with up to 6 side chains whereas Lys<sub>8</sub> is more likely to “stand-up” and interacts with the bilayer with 1 or 2 side chains.<sup>34</sup>

The atomistic simulations also provide detailed information regarding the distribution and orientation of water and ions at the membrane/water interface, from which charge distributions and electrostatic potentials can be computed and compared to experimental measurements. Shown in Figure 4.6 are the distributions of charge from different components for the case of Arg<sub>8</sub> adsorbed at the membrane surface. The result illustrates the large degree of charge compensation among lipids, ions, adsorbing peptides, and interfacial water, leading to a rather small apparent charge density on the order of mC/m<sup>2</sup>; the latter is of the same order of magnitude as measurement from on-going experimental analysis in our group using heterodyned SHG measurements. Further analysis of the interfacial electrostatic potential and charge distribution from the atomistic simulations also enabled us to examine the quantitative validity of the commonly used Gouy–Chapman model for converting measured surface potential to an effective surface charge density. In the Gouy–Chapman model,<sup>48</sup> the interfacial solvent is described using a dielectric continuum with a bulk dielectric constant, which may not be quantitatively appropriate for a charged interface.<sup>15,19,22</sup> Fitting the atomistic simulation results in the form of the Gouy–Chapman model, however, revealed that the appropriate effective dielectric constant model is, in

fact, around 30, close to what we recently reported from SHG experiments.<sup>15</sup> This value is likely due to the considerable dynamical flexibility of the lipid head-groups, which enable interfacial water molecules to re-orient without much hindrance. Therefore, the use of the bulk dielectric constant of water in the Gouy–Chapman model, as is often seen in the literature, leads to a minor overestimate of the interfacial charge density by a factor of  $\sqrt{80/30} \sim 1.6$  at lipid membrane surfaces.

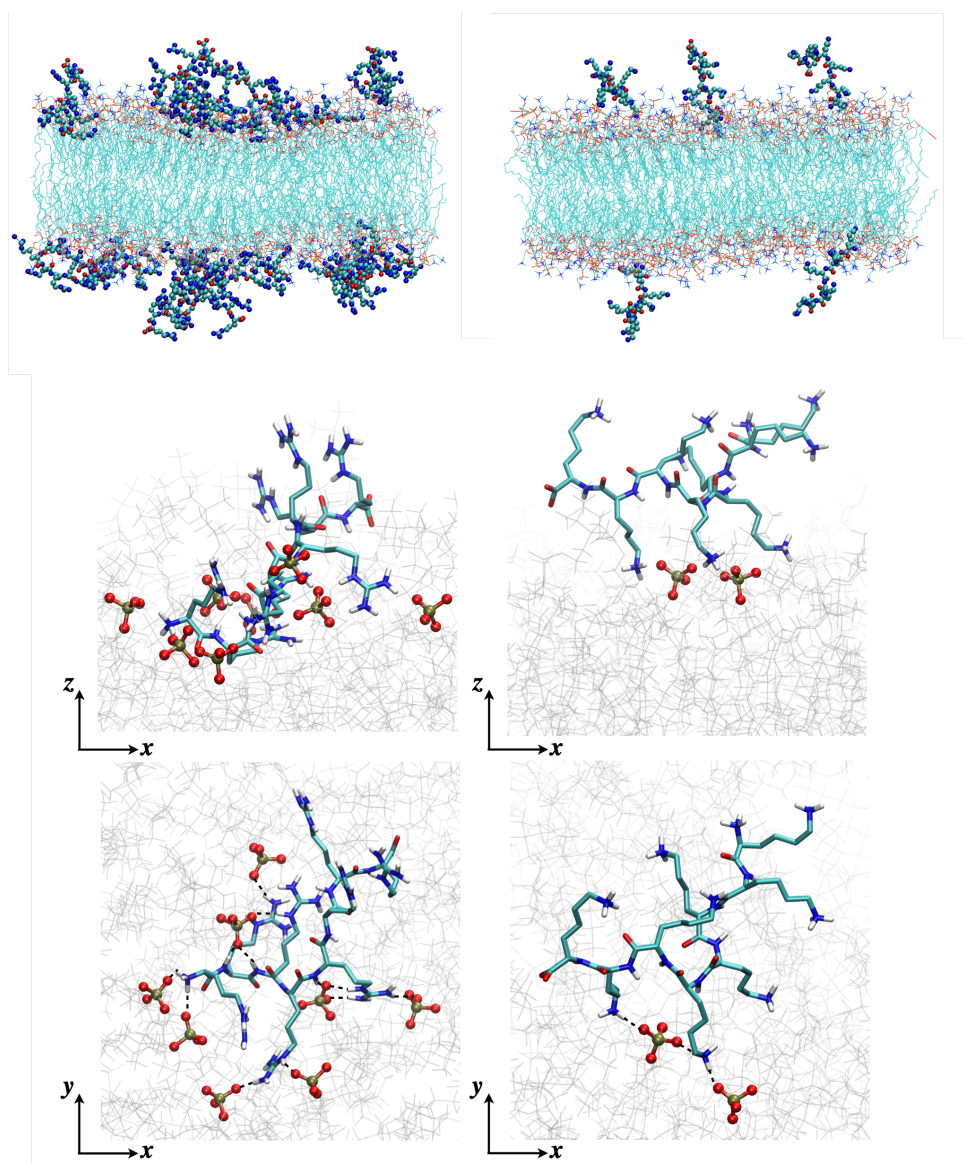


Figure 4.5. The MD simulations show the interaction of Arg<sub>8</sub> (left column) and Lys<sub>8</sub> (right column) with a bilayer formed from a 9:1 mixture of DMPC:DMPG lipids. In the top two panels, the difference in preferred binding between the peptides is seen. Arg<sub>8</sub> prefers to interact with the bilayer, interacting with up to 6 side chains. Lys<sub>8</sub> prefers interacting with the solution, adopting a “stand-up” conformation and interacting with the bilayer with only 1 or 2 side chains. The lower panels show a close up view of the side chains interacting with the phosphate moieties on the lipid headgroup, with Lys<sub>8</sub> interacting with less phosphate moieties than Arg<sub>8</sub>. Reproduced from ref. 34 with permission from the Royal Society of Chemistry (RSC).



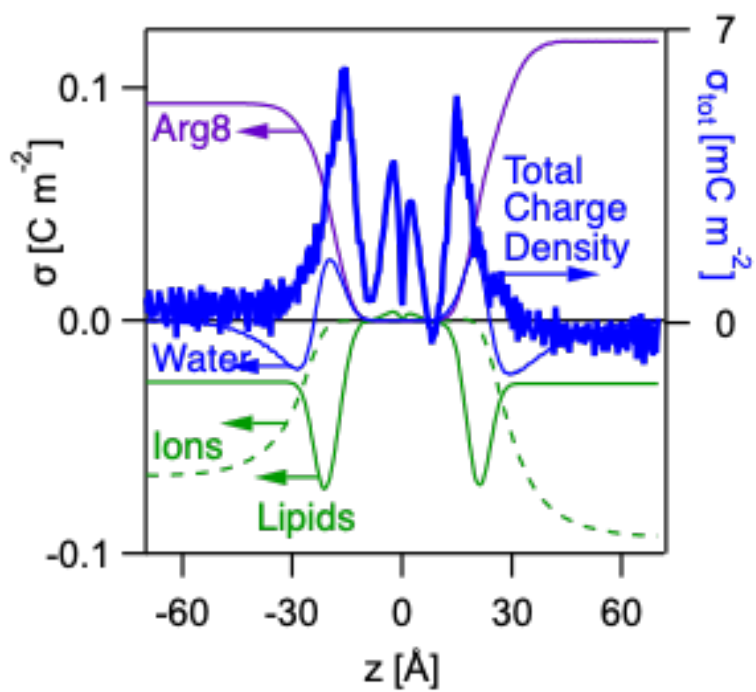


Figure 4.6. Integrated charge density (total, right, and from different components, left),  $\sigma(z)$ , as a function of  $z$  from MD simulations for Arg<sub>8</sub> on a 9:1 DMPC:DMPG bilayer

#### 4.9. Polycations Bind to Bilayers with Comparable $\Delta G_{\text{ads}}$

Besides PAH, we also studied several other polycations that range in size and differ in molecular weight and structure. They also vary in their cationic groups with two polycations (aside from PAH) containing primary amines, namely poly (vinylamine hydrochloride) (PVAm, 25 kDa) and poly-L-lysine (PLL, 4–15 kDa), one polycation containing a quaternary ammonium group, namely poly (diallyldimethylammonium chloride) (PDADMAC, 100 kDa and 400–500 kDa), and one polycation containing a guanidinium group, namely poly-L-arginine (PLR, 5–15 kDa). Figure 4.7 shows that when accounting for the positive charge present (the concentration of each respective polycation multiplied by the respective amount of repeat units), the experimental binding curves, and thus the binding constants, for all polycations surveyed were comparable, regardless of molecular weight or structure.<sup>64</sup>

Reversibility studies were carried out by SHG spectroscopy in order to assess the extent of binding reversibility of the respective polycations (Figure 4.8). All polycations aside from PDADMAC exhibit partial to full reversibility to the bilayers surveyed. PVAm and PDADMAC (400 kDa) exhibit the lowest degree of ionization, being 7% and 16% respectively (the actual degree of ionization estimated from the experiments depends on the contribution of interfacial water to the observed mass change, although the qualitative trend is expected to hold). Yet, while PVAm binds largely reversibly, PDADMAC remains on the bilayer, even when rinsing with polycation-free buffer over more than eight hours. As PDADMAC features the highest molecular weight of the polycations studied, molecular weight and the possibility of loop formation are likely to be an important determinant of the degree of binding reversibility, even counter ion binding to the quaternary ammonium

groups favors charge neutrality. Further work is needed to assess the integrity of the bilayer after the addition of PDADMAC when compared to the other polycations surveyed so as to shed light on whether the bilayer structure is significantly perturbed.

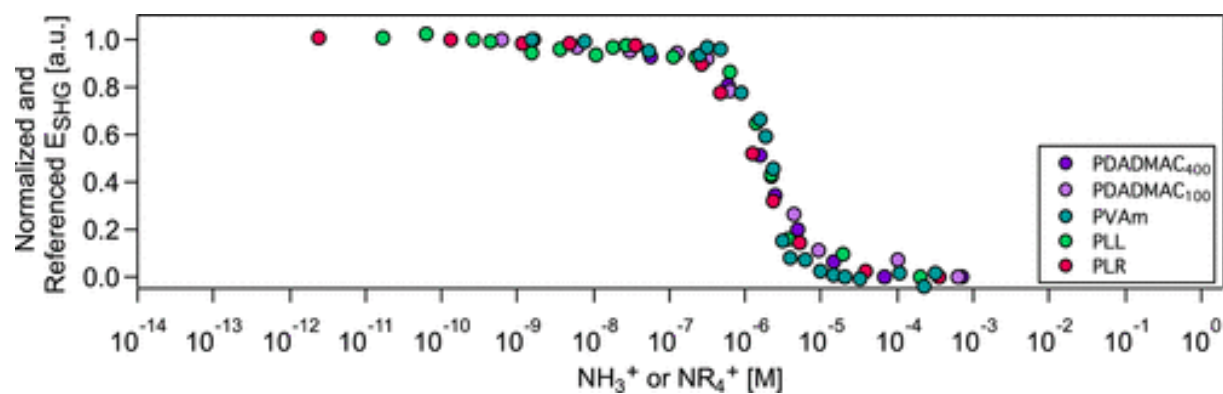


Figure 4.7. Normalized SHG E-field as a function of positive charge for PDADMAC<sub>400</sub>, PDADMAC<sub>100</sub>, PLL, PLR, and PVAm. The concentration of positive charge was determined by multiplying the number of repeat units of each respective polycation by the concentration of the polycation added to the 9:1 DMPC: DMPG bilayer. Adapted from ref. 64 by permission of the Royal Society of Chemistry (RSC) from the PCCP Owner Societies.

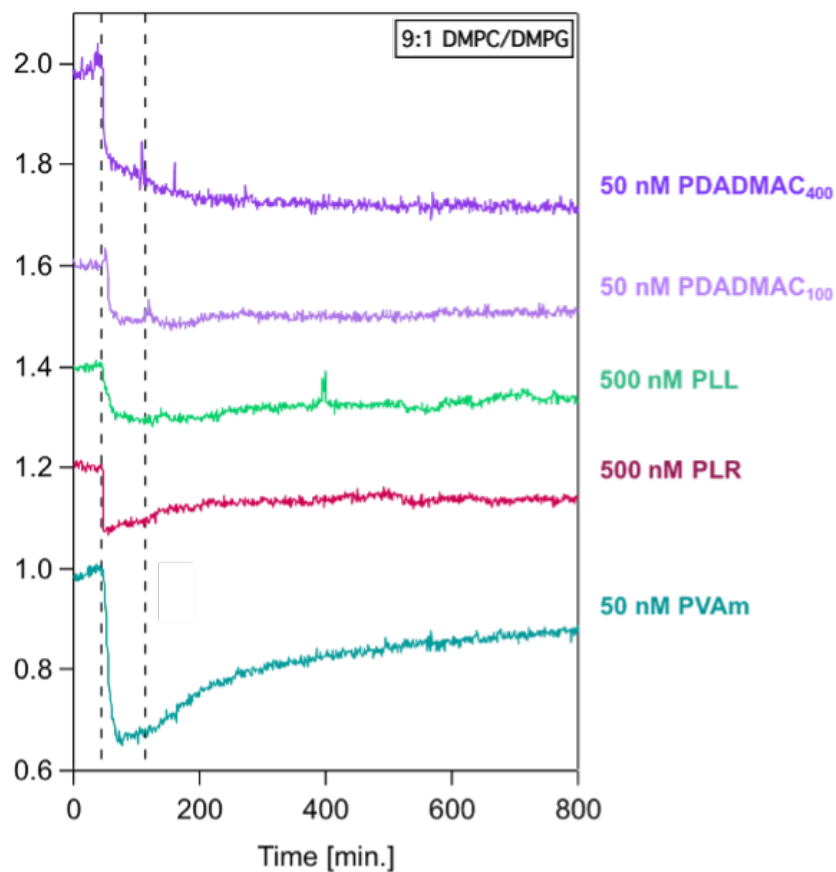


Figure 4.8. Reversibility of adsorption of 50 nM PDADMAC<sub>400</sub> (dark purple), 50 nM PDADMAC<sub>100</sub> (light purple), 500 nM PLL (green), 500 nM PLR (red), and 50 nM PVAm (teal) to a bilayer formed from a 9:1 mixture of DMPC: DMPG lipids. The chosen concentrations represent high surface coverage as determined from their respective adsorption isotherms. At  $t = 43$  min, the polycation solutions are introduced to the bilayer and left to equilibrate until  $t = 112$  min, where the bilayer is then rinsed with polycation-free buffer solution (10 mM Tris, 100 mM NaCl, at pH 7.4). Adapted from ref. 64 by permission of the Royal Society of Chemistry (RSC) from the PCCP Owner Societies.

#### 4.10. Conclusion and Outlook

In conclusion, this review provided mechanistic insight on the interaction of several polycations and peptides with supported bilayer membranes prepared from several different lipids. Large polycations such as PDADMAC and PVAm were found to exhibit low percent apparent ionization as opposed to the smaller peptides and polycations surveyed. The low degree of apparent ionization is likely due to weak binding of these polycations to the membrane surface, crowding, pKa shifts, counter ion compensation, and/or contact-ion pair formation of a small number of their charged repeat units. Interfacial water structure at the PAH:membrane interface was studied at high PAH surface coverage, which resulted in membrane dehydration and the displacement of water molecules by PAH. Additional work is needed to determine the orientation of water molecules with the addition of polycations to our bilayer system by using heterodyne-detected SHG (HD-SHG).<sup>33,65–67</sup> This technique accesses the  $\chi^{(2)}$  and the potential-dependent  $\chi^{(3)}$  terms directly so as to inform about the Stern and Diffuse Layers within the electrical double layer. Furthermore, real-time HD-SHG imaging holds the promise of providing 200 to 300 nm spatial resolution at video frame rates while the EDL expands and compresses during peptide or polycation adsorption. Moreover, the technique allows one to investigate whether dynamics in the Stern and the Diffuse Layers are concerted or decoupled from one another so as to test the validity of Bragg–Williams approaches for describing lipid membranes.

The fundamental mechanisms underlying polycation:membrane interactions shed light on the initial stages of membrane rupturing by processes such as dehydration. This mechanism, as evidenced by our work thus far, depends on the extent of polycation surface coverage. Moreover, the extent of binding and the surface charge contribute to the expulsion

of interfacial water molecules. This insight can be applied to the design of antimicrobials as surrounding dehydration can result in cell death and changes to normal membrane function. This process can be further optimized through predictive computer simulations like the ones described here, or by thermodynamic and electrostatic measurements that are coupled to polycation synthesis capabilities. Hydrophilic polycations are just as vital to study as those that are hydrophobic in order to make advancements in biocidal materials. Future work, therefore, may be extended to include polycations with varying degrees of hydrophilicity and hydrophobicity.

Integration of computer simulation and experimental work is crucial for a quantitative understanding of the SHG/SFG spectra and their molecular level interpretation regarding peptide/polycation-membrane interactions. Along this line, we note that while numerous studies have been conducted to compute SFG spectra for various interfaces (e.g., air/water and membrane/water),<sup>40,68</sup> the number of SHG simulations for solid/water or membrane/water interfaces is modest.<sup>69</sup> Moreover, most atomistic simulations for polycation/peptide-membrane focused on rather short oligomers, with the degree of polymerization in the range of 10–30.<sup>37,70</sup> With further improvement in the accuracy of computational models and algorithms for sampling the conformational and titration states of peptides, oligomers, and polymers at membrane/water interfaces,<sup>71</sup> as well as the development of more sophisticated theoretical models for soft matter interfaces,<sup>72,73</sup> sensitive experimental measurements for membrane/polymer interactions, such as SHG/SFG reviewed herein, will be understood at a more quantitative level, enabling the design of novel biocidal materials with molecular level of precision.

#### 4.11. Future Work: Gramicidin A (gA) containing Supported Lipid Bilayers (SLBs)

In this chapter, we focused on studying the addition of peptides and polycations to the surface of supported lipid bilayers (SLBs). Through simulations, it was apparent that peptides such as Arg<sub>8</sub> and Lys<sub>8</sub> interact with the bilayer through different mechanisms with Arg<sub>8</sub> inserting more deeply into the bilayer surface. To further build on this work, the linear antibiotic peptide, gramicidin A (gA) (15 amino acids in length),<sup>74,75</sup> is considered for future experiments. This peptide integrates into the lipid membrane and forms ion channels. Studying this peptide will not only contribute to our existing knowledge of the interactions of peptides with model membranes, but it will also allow for the increased complexity of our idealized model membrane system.

Ion channels are essential to controlling the flux of ions across a membrane in a very specific manner. The channels formed by gramicidin A are selective to monovalent cations such as Na<sup>+</sup> and K<sup>+</sup>.<sup>74,75</sup> In our previous study, we have seen that an increase in the concentration of negatively charged lipids in the SLBs (10 mol % to 20 mol % PG lipids) leads to a decrease in the sum frequency signal intensity at  $\sim 3,100\text{ cm}^{-1}$ .<sup>52</sup> This was likely due to the small (yet significant) decrease in water molecules surrounding the adjacent lipid headgroups. Therefore, it is clear that changes to the SLB composition can result in changes to the associated hydrogen-bonding network.

With the integration of gramicidin A, it is likely that the respective hydrogen-bonding network will also change when compared to the pure bilayer. The tryptophan side chains from the gramicidin A residues hydrogen-bond with the lipid head groups to orient the C-terminus of the gramicidin A helix towards the bilayer surface and the N-terminus towards



the bilayer interior.<sup>74</sup> Therefore, integrating gramicidin A into the membrane can impact the orientation (and packing) of adjacent lipids, and thus, may result in differences in hydrogen-bonding. It would then be interesting to determine how monovalent vs. divalent cation salts (NaCl vs. CaCl<sub>2</sub>) effect the water structure as the ion channels formed by gramicidin A interact primarily with monovalent cations.

In the literature, gramicidin A integrated bilayers have been formed successfully. One study used SFG spectroscopy to determine the role of gramicidin A in lipid flip-flop.<sup>76</sup> Here, the membranes integrated with gramicidin A were formed using the Langmuir–Blodgett/Langmuir–Schaefer (LB/LS) method. The incorporation of gramicidin A in the lipid membranes was then confirmed using attenuated total reflection Fourier transform infrared spectroscopy (ATR-FTIR). Therefore, by using existing preparation and characterization methods, these membranes can be formed and tuned depending on the experiments.

## CHAPTER 5

**Beyond Fresnel Factors: Probing the Interfacial Water  
Structure at Nickel:Nickel:Oxide:Water Interfaces with Sum  
Frequency Generation (SFG) Spectroscopy**

**Portions of this chapter are part of the following manuscript, in preparation:**

Dalchand, N.; Xi, S.; Gururangan, K.; Walker, C.E.; Ly, C.; Lozier, E.H.; and Geiger,

F.M. Beyond Fresnel Factors: Probing the Interfacial Water Structure at  
Nickel:Nickel:Oxide:Water Interfaces with Sum Frequency Generation (SFG)

Spectroscopy. **2021.**

*In Prep.*

## 5.1. Introduction

When exposed to air, nanoscale metal thin films composed of Earth abundant metals form an oxide overlayer that exhibits complex electronic properties when in contact with water due to the interfacial charged species that exist therein.<sup>1,2</sup> Recently, nanolayer thin films composed of metals such as Fe, V, and Ni have been found to produce electrical current due to intraoxide electron transfer controlled by the motion of ionic water droplets.<sup>3</sup> Therefore, investigating interactions at the metal-water interface is crucial to our understanding of a wide variety of emerging technological devices traversing the fields of energy, electrochemistry, and catalysis.<sup>4-6</sup>

Previous interface specific studies have been conducted on similar metallic interfacial systems using sum frequency generation (SFG) spectroscopy. This technique is interface selective as second-order nonlinear processes are forbidden under the electron dipole approximation in media with inversion symmetry, i.e., in the bulk.<sup>7,8</sup> The sum frequency intensity is proportional to the square modulus of the second-order nonlinear susceptibility tensor  $\chi_{\text{eff}}^{(2)}$  by the relationships shown in Equation 5.1.<sup>9-13</sup>

$$(5.1.1) \quad I_{\text{SFG}}(\omega_{\text{SFG}}) \propto |\chi_{\text{eff}}^{(2)}|^2 I_{\text{VIS}}(\omega_{\text{VIS}}) I_{\text{IR}}(\omega_{\text{IR}})$$

$$(5.1.2) \quad \chi_{\text{eff}}^{(2)} = \chi_{\text{NR}}^{(2)} + \chi_{\text{surface}}^{(2)} + \frac{\kappa}{\sqrt{\kappa^2 + (\Delta k_z)^2}} e^{i \arctan(\frac{\Delta k_z}{\kappa})} \Phi(0) \chi^{(3)}$$

Here,  $\kappa$  is the inverse Debye screening length,  $\Delta k_z$  is the inverse coherence length of the sum frequency process, and  $\Phi(0)$  is the interfacial potential. As denoted by Equation 5.1.2,  $\chi_{\text{eff}}^{(2)}$  includes both the resonant ( $\chi_{\text{surface}}^{(2)}$ ) and nonresonant contributions ( $\chi_{\text{NR}}^{(2)}$ ) from

the system. The nonresonant contributions are spectrally broad; they are present in metals such as gold and silver due to the electronic states present therein.<sup>14-16</sup> These contributions can amplify weak resonant signal in heterodyne detection, but they can also overwhelm resonant contributions in other systems.<sup>17</sup> The overwhelming nonresonant contributions from the metal-water interface was previously studied for Au, Ti, and ITO in the work of Backus et. al.<sup>18</sup> Probing such interfaces was not only difficult due to the electronic nonresonance of the metals and metal-oxides used, but also due to lineshape contributions dominated by Fresnel factors. Significant progress has, nonetheless been made in probing the metal-water interface as the work of Tong et. al more recently reported the hydrophobic nature of water at the gold electrode-water interface using a home-built spectroelectrochemical cell, in which the IR and visible beams contact the electrode through a thin water layer.<sup>19</sup> In this work, they were able to elucidate a peak at  $3,680\text{ cm}^{-1}$  that they observed as the weakly bound water molecules due to the successful transmission of a significant amount of IR light through the thin water layer at frequencies above  $3,600\text{ cm}^{-1}$ . However, probing the extensive hydrogen-bonding network at frequencies in the range of  $3,000 - 3,600\text{ cm}^{-1}$  was still challenging as IR light was absorbed by the external thin water layer in this regime. These studies detail the many challenges in monitoring the interfacial hydrogen-bond network over metals. Studying the metal-water interface has been of scientific interest because of the nature of conductive materials that allows for direct control over the interfacial potential at a given aqueous interface. This would further contribute to our understanding of the electrochemical behavior at material interfaces such as to further optimize their design for projected consumer use.

In an effort to maximize the resonant water response from our metal films, we collected our spectra using PPP-polarization (*p*-polarized SFG, *p*-polarized visible light, and *p*-polarized IR light) as much previous work has reported on maximum sum frequency signal from molecules at metal surfaces when using this polarization combination due to the orthogonal orientation of the transition dipole to the metal surface.<sup>19</sup> We have also used nickel as the metal of choice for these experiments, whose nonresonant response is smaller than that for gold. Baker et. al has shown the signal measured on a 45 nm nickel film to be less than 1% of that measured on gold due to the lack of a surface plasmon resonance (SPR) supported by the nickel film.<sup>20</sup> Furthermore, to ensure that a significant amount of IR penetrates through the metal and contacts the water molecules, the absorption of the thin films were measured and found to be significantly different between films that differed in thickness by as little as 1 nm.

Our SFG set-up was tuned such that no burning was seen on these films and control experiments regarding our calcium fluoride ( $\text{CaF}_2$ ) substrate were carried out and resulted in no sum frequency intensity likely due to the attenuation of our optical set-up (low IR power and loose visible focus). Lastly, due to the ability of the nickel nanolayers to convert mechanical to electrical energy when in contact with ionic solutions, the projected use of these materials would be in oceans and groundwater ecosystems. Therefore, we assessed the effect of introducing salt to the hydrogen-bonding network above the nickel:nickel:oxide surface at two relevant pH's, pH 8.5 (ocean water) and pH 5.8 (groundwater). Here, we find some evidence of a weaker hydrogen-bonding network due to a higher pH. Little change is seen with the addition of 100 mM NaCl.

## 5.2. Methods

### 5.2.1. Metal Nickel Layer Preparation and Characterization

Nickel nanolayers described in this work were prepared with HHV ATS-500 physical vapor deposition system. Prior to deposition, 3 mm thick IR grade  $\text{CaF}_2$  windows (ISP Optics) were sonicated in methanol and then DI water for 12 minutes each and placed into an  $\text{O}_2$  plasma cleaner (Harrick) for 10 minutes on the highest power. Standard purity nickel evaporation pellets (Kurt J. Lesker, Co.) were packed into their appropriate crucible liners (Kurt J. Lesker, Co.) and placed in the source turret inside the deposition chamber. The chamber was evacuated until the pressure reached a base pressure of  $6 \times 10^{-6}$  mbar (optimal vacuum for different metals will vary, please refer metals' evaporation temperature under different pressures). Once the appropriate vacuum was obtained, the nickel source was bombarded with an electron beam with power corresponding to at least 0.5 nm/sec evaporation rate. The film thicknesses were determined in situ with a quartz crystal microbalance and post-deposition with a variable-angle spectroscopic ellipsometer (J.A. Woollam M2000U). To determine film uniformity, the Hitachi S4800-II Scanning Electron Microscopy (SEM) was used. The images were taken at three different magnifications ( $110\times$ ,  $450\times$ , and  $3,000\times$ ) with an incident electron energy of 10 keV.

### 5.2.2. X-ray Photoelectron Spectroscopy (XPS)

An analysis of nickel films—to gauge surface and subsurface composition—was performed on a Thermo Scientific ESCALAB 250Xi spectrometer equipped with an electron flood gun and a scanning ion gun. To start, three narrow scans were executed for each element of interest at the film's surface with a pass energy of 50 eV, a dwell time of 50 ms, and

an energy step size of 0.1 eV, then averaged to yield a final spectrum. To access a film's subsurface, the ion gun was run at 2000 eV for a 5 s etch cycle and a raster size of 2.00 mm, after which the same set of narrow scans were performed as for the film's surface. All analyses were run using a XR6 monochromated X-ray source (500  $\mu\text{M}$ ) with an aluminum anode.

### 5.2.3. Contact Angle Measurements

To monitor any changes in hydrophilicity of the nickel films over time, contact angle measurements were taken using an FTA125 goniometer. The contact angles were taken on nickel films that were prepared on clean 3 in. by 1 in. glass microscope slides. Using glass slides as the substrate in these experiments allowed for multiple contact angles to be taken across a single sample as the surface area is much larger than that of the  $\text{CaF}_2$  substrate. The glass slides were cleaned by placing them in a Nochromix (glass cleaner)/sulfuric acid solution for 1 hr. The slides were then sonicated in methanol for 6 mins and water for 6 mins as well. Finally, the slides were dried with  $\text{N}_2$  and placed in an  $\text{O}_2$  plasma cleaner for 30 s.

The nickel nanolayers were then deposited on the glass slides as detailed in section IIA. Right after deposition, the contact angle of one of the nickel deposited glass slides was taken using the goniometer and represents the hydrophilicity of the film at time 0. A set of films from the same deposition were then left exposed to the ambient laboratory environment and the contact angle of each film was taken at a different timepoint, with the whole set taken in 3 weeks.

To measure the contact angle, a single droplet was formed on the tip of a glass syringe. The droplet was then released on the film surface and a camera was used to take a snapshot of the curvature of the droplet on the film. The software automatically identified the angle between where the droplet contacts the surface and the apex of the droplet. For hydrophilic surfaces with contact angles  $< 20^\circ$ , the software often has difficulties with identifying the droplet apex. Therefore, the angle was manually determined. Each droplet was captured for 41 images.

#### 5.2.4. Vibrational Sum Frequency Generation Spectroscopy

Details of our SFG set-up have been previously reported.<sup>10,21</sup> Briefly, a Ti: sapphire laser system (Solstice, 795 nm pulses, 3 mJ/pulse, 1 kHz repetition rate, 120 fs pulse duration) was used to pump an optical parametric amplifier (TOPAS) to produce a tunable IR beam. The IR beam was tuned to the C–H and O–H stretching regions (2,800–3,800  $\text{cm}^{-1}$ ). The IR and visible beam overlapped at the sample stage with incident angles of  $64^\circ$  and  $47^\circ$  respectively. To avoid burning of our 3–4 nm nickel nanolayers, the IR power was reduced to  $\sim 4.5 \mu\text{J}$  and the visible beam ( $\sim 1.5 \mu\text{J}$ ) was loosely focused to an approximate diameter of  $\sim 1\text{--}2 \text{ mm}$ .<sup>22</sup> All spectra were taken in PPP-polarization ( $p$ -polarized SFG,  $p$ -polarized visible light, and  $p$ -polarized IR light) and in internal reflection geometry. A schematic of our three-layer system composed of  $\text{CaF}_2$ , nickel(-oxide), and an aqueous solution ( $\text{H}_2\text{O}$  or  $\text{D}_2\text{O}$ ) is shown in Figure 5.1. Contributions from both the  $\text{CaF}_2$ -nickel(-oxide) (interface I) and nickel(-oxide)- $\text{H}_2\text{O}$  (interface II) are considered and detailed explicitly in Section 5.2.6. Due to low signal-to-noise, the spectra were acquired for 40–60 minutes with no visible signs of burning. To determine that IR light was not



completely absorbed by the metal nanolayer, transmission spectra were taken between our region of interest ( $2,800\text{--}3,800\text{ cm}^{-1}$ ) using the Thermo Nicolet iS50 spectrometer for the nickel nanolayers on  $\text{CaF}_2$ .

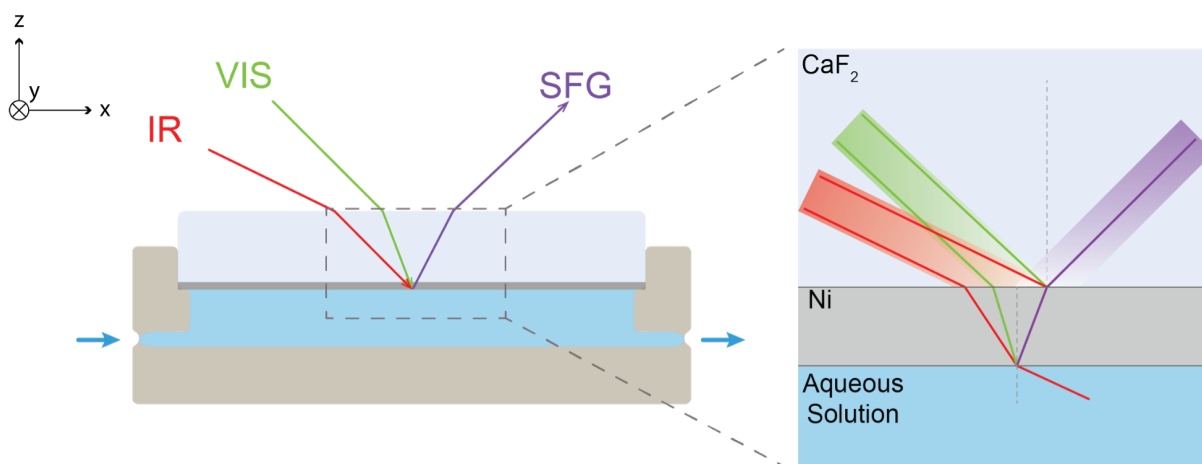


Figure 5.1. Side view (left) of the experimental geometry and a zoom-in (right) on the 3-layered  $\text{CaF}_2$ /nickel:water interface. Dark blue and dark grey represent the water layer and the metal:metal:oxide layer.

### 5.2.5. Flow Experiments

Flow experiments were done in a custom-built Teflon flow cell, in which  $\text{D}_2\text{O}$  (Sigma Aldrich, 151882) was flowed prior to Millipore  $\text{H}_2\text{O}$  ( $18.2\text{ M}\Omega\text{ cm}$ ) to correct for the frequency-dependent IR profile of the nickel: $\text{H}_2\text{O}$  spectra. This method has been used previously in the literature. Aqueous salt solutions ( $100\text{ mM}$ ) were then introduced into the flow cell after Millipore  $\text{H}_2\text{O}$ ; the flow rate was  $\sim 2\text{ mL/min}$ . The aqueous solutions were equilibrated in ambient air to pH 5.8 and adjusted to pH 8.5 using small quantities of NaOH depending on the experiment. The pD was also adjusted to 5.8 and 8.5 using dilute quantities of NaOD (Sigma Aldrich, 164488) or DCl (Sigma Aldrich, 543047)

also depending on the experiment. A conventional glass electrode pH meter was used to measure both pH and pD. The pD was corrected according to the Gross–Butler–Purlee theory:  $\text{pD} = \text{pH} + 0.44$ .<sup>23–25</sup>

### 5.2.6. Fresnel Factor Theory and Calculations

SFG intensity is proportional to the square modulus of  $\chi_{\text{eff}}^{(2)}$  as shown by Equation 5.1.1. Of the 27 tensor elements of  $\chi_{\text{eff}}^{(2)}$ , 7 are non-zero due to symmetry constraints. They can be accessed by the polarization combinations SSP, SPS, PSS, and PPP (beam order: SFG-VIS-IR). Past studies have shown that SFG intensity from the metal(-oxide)/water interface to be the greatest under PPP-polarization combinations.<sup>26</sup> This is in accordance with our experimental observation that spectra obtained under PPP is much higher in intensity and lower in noise than those under SSP. For this reason, experiments and simulations are carried out and compared under PPP-polarization. There are 4 tensor elements associated with PPP-polarization,  $\chi_{\text{xxz}}^{(2)}$ ,  $\chi_{\text{zzx}}^{(2)}$ ,  $\chi_{\text{zxx}}^{(2)}$ , and  $\chi_{\text{zzz}}^{(2)}$  as shown in Equation 5.2.1.<sup>27,28</sup> Although we are unable to calculate the exact value of  $\chi_{\text{eff}}^{(2)}$  due to the inability to calculate the aforementioned individual tensor elements, we are able to determine the magnitudes of the scalar quantities they are multiplied by according to Equations 5.2.2–5.2.5. Even then, the relative magnitude of each term in Equation 5.2.1 can differ significantly depending on the values to each tensor element. Therefore, we compare the spectral lineshapes from our calculations of 5.2.2–5.2.5 to our experimental data to determine the major contributing tensor elements.

$$(5.2.1) \quad \chi_{\text{eff,ppp}}^{(2)} = A\chi_{\text{zzz}}^{(2)} - B\chi_{\text{xxz}}^{(2)} + C\chi_{\text{zxx}}^{(2)} - D\chi_{\text{zzx}}^{(2)}$$

where the scalars in front of the tensor elements are given by:

$$(5.2.2) \quad A = L_{zz}(\omega_{\text{SFG}})L_{zz}(\omega_{\text{VIS}})L_{zz}(\omega_{\text{IR}}) \sin \theta_{\text{SFG}} \sin \theta_{\text{VIS}} \sin \theta_{\text{IR}}$$

$$(5.2.3) \quad B = L_{xx}(\omega_{\text{SFG}})L_{xx}(\omega_{\text{VIS}})L_{zz}(\omega_{\text{IR}}) \cos \theta_{\text{SFG}} \cos \theta_{\text{VIS}} \sin \theta_{\text{IR}}$$

$$(5.2.4) \quad C = L_{zz}(\omega_{\text{SFG}})L_{xx}(\omega_{\text{VIS}})L_{xx}(\omega_{\text{IR}}) \sin \theta_{\text{SFG}} \cos \theta_{\text{VIS}} \cos \theta_{\text{IR}}$$

$$(5.2.5) \quad D = L_{xx}(\omega_{\text{SFG}})L_{zz}(\omega_{\text{VIS}})L_{xx}(\omega_{\text{IR}}) \cos \theta_{\text{SFG}} \sin \theta_{\text{VIS}} \cos \theta_{\text{IR}}$$

The expressions for the Fresnel factor (L) calculations are written in detail in Chapter 2. Briefly,  $L_{xx}^{(I)}$  and  $L_{zz}^{(I)}$  are calculated for interface I (CaF<sub>2</sub>-nickel(-oxide)) and  $L_{xx}^{(II)}$  and  $L_{zz}^{(II)}$  are calculated for interface II ((nickel(-oxide)-water)).<sup>18</sup> The calculation of the Fresnel Factors for both interface I and interface II rely on the refractive indices for all three media in our three-layer system (CaF<sub>2</sub>, nickel, and water). These calculations were also done for D<sub>2</sub>O as the third medium (instead of water) to minimize the contribution from the interfacial –OH resonance response within our frequency range of interest and serve as a reference to the later experiments involving water. The ratios of H<sub>2</sub>O spectra and D<sub>2</sub>O spectra are then taken for both interface I and interface II to show the change due to the resonant response of water molecules at the interface. These calculations are shown in Figure 5.5 with comparison to our experimental results.

### 5.3. Results and Discussion

#### 5.3.1. Hydrophobicity of Nickel Nanolayers Increases Over Time

Contact angle measurements were done to determine the hydrophilicity of the nickel nanolayers as this parameter could be crucial to the hydrogen-bonding of water molecules

at the interface. Through initial contact angle measurements of nickel films taken at different times after deposition, we found there was a change in the hydrophilicity of the nickel nanolayers, therefore, we conducted experiments assessing the contact angle of the thin films over time when the film was exposed to ambient laboratory air. As shown in Figure 5.2a, the contact angle over time for the 5 nm nickel films is shown to increase from  $\sim 10^\circ$  to  $\sim 60^\circ$  over time. This increase in contact angle over time is specific to the nickel nanolayer as glass slides taken in the same range show minimal change. This suggests an increase in the hydrophobic character of the nickel nanolayers over time which tails off at 350 hrs (or 2 weeks). The increase in hydrophobicity is likely due to the presence of adsorbed hydrocarbons from the ambient lab environment as was seen for films of  $\text{TiO}_2$  in the literature.<sup>29</sup> SFG spectra shown in Figure 5.2b further corroborates this hypothesis as there is a pronounced peak shown in the C–H stretching region at  $\sim 2,940 \text{ cm}^{-1}$  after 24 hours of the film being exposed to laboratory air. Plasma cleaning was not done to clean the films due to the introduction of oxygen that could modify the film surface chemistry and increase variability between samples.

### 5.3.2. Nanolayer Characterization and Substrate Contribution Assessment

Before studying the interfacial water structure at the nickel nanolayer surface, the thin films were characterized thoroughly. Figure 5.3a shows an SEM image of a pristine  $\sim 5$  nm nickel film. The film shows uniform coverage across the substrate in a field of view comparable to that of the visible beam spot size. To ensure the visible and IR beams could properly transmit through the metal films without being absorbed (or reflected), we conducted transmission FTIR in conjunction with ellipsometry measurements. Figure 5.3b shows that the percent absorbance of the films increases with increasing film thickness, which is expected. Less anticipated, was the degree at which the absorbance changes upon the addition of each subsequent nanolayer. At thicknesses approaching 5 nm, this absorbance is  $\sim 60\%$ . At  $\sim 4$  nm, this absorbance decreases to  $\sim 50\%$  and at  $\sim 2$  nm, the absorbance decreases further to  $40\%$ . We note that, in our attempt to probe the hydrogen-bonding network, the responses given by the thinner films ( $\leq 4$  nm) yields different lineshapes than those of thicker films (4 – 5 nm) as shown in Figure 5.4. The lineshapes of the  $\leq 4$  nm films showcase a broad feature  $\sim 3,200\text{ cm}^{-1}$  (discussed further in Section 5.3.3.), whereas such a feature was not present for films  $\sim 5$  nm thick. We believe this to be due to the higher absorption of the  $\sim 5$  nm nickel thin films. The response from these films is likely due to the overwhelming contributions from the Fresnel factors therein.

The FTIR measurements detail the thickness ( $\leq 4$  nm) of the nickel nanolayers that were used in the experiments shown in Sections 5.3.3. and 5.3.4. Due to the thin nature of the films, we also acknowledged concerns of possible pores in the nanolayers. These pores would allow for contributions of the underlying substrate (calcium fluoride ( $\text{CaF}_2$ ))

to our sum frequency signal if present. Under visual inspection and SEM images, the films are spread evenly across the substrate surface. A smaller field of view for SEM was also taken for these thin films ( $\sim 30 \mu\text{m}$ ) and they also do not show any signs of  $\text{CaF}_2$  pockets. However, XPS analysis notes the presence of metal fluorides on the sample surface as shown by Figure 5.3c. Due to the presence of the fluorides on the surface, SFG experiments were done on the plain calcium fluoride substrate under the same experimental considerations as how the nickel-water interface is probed (i.e., loosely focused visible lens, low IR power, etc.). Figure 5.3d shows that at both pH 5.8 and pH 8.5 there is no signal from our calcium fluoride substrate. As has been previously noted in the literature, the point of zero charge (PZC) of  $\text{CaF}_2$  is  $\sim \text{pH } 6.2$ .<sup>30,31</sup> Here, there is low surface charge which leads to little to no sum frequency response. Therefore, it is unsurprising that there is no detectable signal at pH 5.8 for the  $\text{CaF}_2$ -water interface. As the pH continues to increase from the PZC, it is expected that there is an increase in the sum frequency signal due to the subsequent reorientation of water molecules at the interface due to electrostatic alignment. Here, however, we do not see any signal present at pH 8.5. We believe this is due to the low incoming IR power and loosely focused visible lens which already yields a relatively low nonresonant response from the nickel film. Thus, due to the minimal presence of signal from the  $\text{CaF}_2$ -water interface we concluded that it is not significantly contributing to the sum frequency response of the nickel-water interface under the conditions of our experiment.

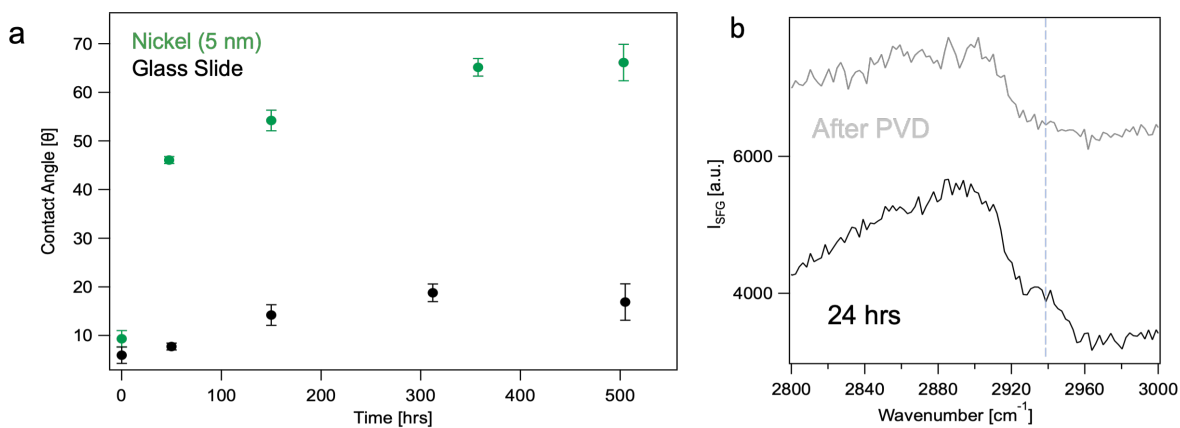


Figure 5.2. Contact angles increase substantially over time for 5 nm nickel films (green) when compared to plain glass slides (black) left out in ambient laboratory air (a) due to the presence of hydrocarbons. (b) SFG spectroscopy is sensitive enough to detect the presence of hydrocarbons in the span of 24 hours.

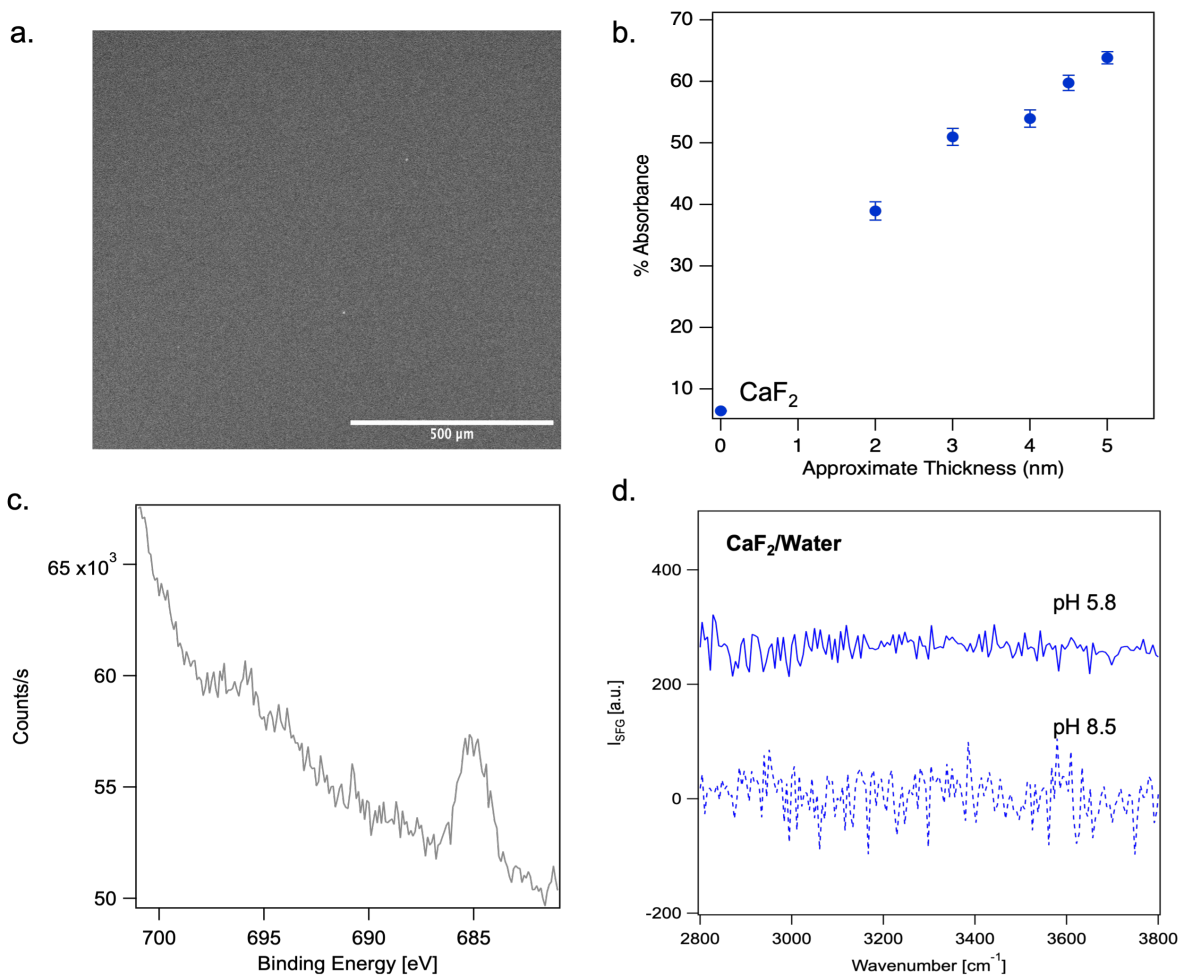


Figure 5.3. The uniformity of the  $\sim 5$  nm nickel film is shown in (a) from an SEM image where the field of view is the approximately the same as the visible beam diameter. IR absorbance of films with thicknesses between  $\sim 2$ – $5$  nanometers was taken using FTIR. The absorbance is shown to be highest for films  $\sim 5$  nm at  $\sim 60\%$  (b). Due to the thin nature of the films, it is possible the  $\text{CaF}_2$  substrate may interfere with the response from the nickel:nickel:oxide:water interface. XPS reveals metal-fluorine bonds at the sample surface (c). However, SFG spectroscopy of plain  $\text{CaF}_2$  at two different values of pH does not result in any signal. Therefore, it is likely the SFG response we collect is not from the  $\text{CaF}_2$ -water interface.



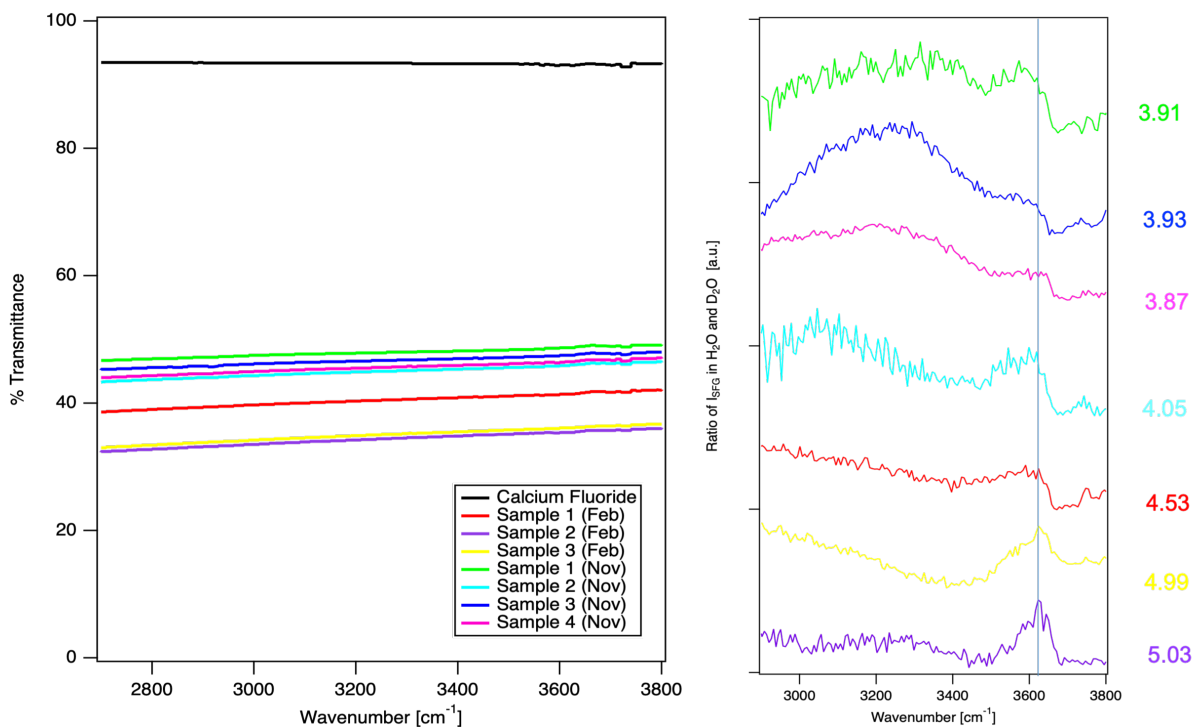


Figure 5.4. Corresponding FTIR (recorded in % transmission), Ellipsometry, and SFG spectra for films of different thicknesses. The thickest film is shown in purple with the lowest % IR transmitted. The thinnest film is shown in green and corresponds to the highest % transmittance of the films shown in this data set.

### 5.3.3. Fresnel Factor Contributions

As previously shown by Backus et. al, the metal:metal:oxide:water interface is particularly challenging to probe due to the complication of Fresnel factors, which account for the transmission and reflection of light at an interface. In their work, the experimental sum frequency lineshapes showed a close resemblance to that of the simulated Fresnel spectra under PPP-polarization. This indicates that the Fresnel coefficients from the interface dominates the overall spectral response. Moreover, in their work, there were nonresonant spectral features present between  $3,000 - 3,400 \text{ cm}^{-1}$  that can overwhelm and complicate potential responses from interfacial water molecules. Therefore, in order to probe interfacial water molecules beyond the Fresnel dominance at the interface, it is important to choose a metal whose Fresnel contributions are featureless in the O–H stretching region. We choose to base our analysis on computing the spectral coefficients A-D (Equations 5.2.2 – 5.2.5) for the metal:metal:oxide:water interface and dividing them by their corresponding metal:metal:oxide:D<sub>2</sub>O spectra. The latter interface serves as a point of reference with no externally introduced O–H oscillators. As a result of the divided spectra, we expected to see if a new feature had emerged resulting from the change of experimental conditions (from D<sub>2</sub>O to H<sub>2</sub>O). The spectral coefficients are shown as opposed to the sole spectra of the individual Fresnel coefficients due to their inclusion of Fresnel contributions from the IR, VIS and SFG light. In order to efficiently simulate a full PPP spectrum, the values of  $\chi_{\text{xxz}}^{(2,n)}$ ,  $\chi_{\text{xzx}}^{(2,n)}$ ,  $\chi_{\text{zxx}}^{(2,n)}$ , and  $\chi_{\text{zzz}}^{(2,n)}$ , need to be known as shown by Equation 5.2.1. We acknowledge that these nonlinear second-order susceptibility tensors could be possibly evaluated using a host of different polarizations, however, that is beyond the scope of this work but will be part of the ongoing work in our lab.

In the following discussion, the spectral coefficients are from interface II, and their corresponding superscripts,  $n=II$ , as indicated by Equations 5.2.1 – 5.2.5 are omitted for brevity. Although interface I is not the interface of interest, we note that its spectral lineshapes can contribute to our sum frequency signal, therefore, calculations were also done for interface I and are qualitatively similar to those from interface II as Figure 5.5 shows. From this we determined that interface I would not affect the following analysis.

As shown in Figure 5.5, two types of lineshapes emerge from the calculation of the spectral coefficients. We see that the ratio of lineshapes of the spectral coefficients A and D have similar spectral features as both are dominated by the contribution from  $L_{zz}(\omega_{IR})$ . This value changes with variable input IR frequencies throughout the experiment. We also see that spectral coefficients B and C share similar features due to the dominance of  $L_{xx}(\omega_{IR})$ . It is important to note that when nickel is chosen to be the reflective layer, in the region of  $3,000 - 3,400 \text{ cm}^{-1}$  where interfacial water molecules vibrate, all four divided spectra of A, B, C, and D show a flat and featureless zone. This simulation indicates the Fresnel contribution to the triple layer system when nickel is in use will not overwhelm interfacial water response, making nickel-based triple layer system an ideal platform for investigating interfacial water without the complication from Fresnel factors.

Indeed, when compared to our experiment results as shown in grey in Figure 5.5, regions outside of the  $3,000 - 3,400 \text{ cm}^{-1}$  zone resembles strongly with the simulated spectral coefficient spectra for Figures 5.5b and 5.5c. Namely, the shoulder at  $\sim 3,500 - 3,600 \text{ cm}^{-1}$  and the region between  $3,650$  and  $3,800 \text{ cm}^{-1}$  both persists regardless of experimental conditions, clearly indicating their origin from the Fresnel factors from the nickel:nickel:oxide:water interface. Therefore, studying the “dangling” O–H groups which

occur at  $3,600\text{ cm}^{-1}$  and beyond is convoluted within our set-up. We note that this region would have been of interest to study as the films increase in hydrophobicity overtime, however, in the region we can probe, we note the presence of a peak at  $\sim 3,200\text{ cm}^{-1}$  in our experimental data as shown by Figures 5.5b and 5.5c, indicating the presence of a tightly knit hydrogen-bonding network<sup>21,32</sup> at a pH 5.8. In the literature it was recently shown that as the number of graphene monolayers increases from 1 to 6, the graphene samples become more hydrophobic.<sup>33</sup> SFG spectra taken for each layer results in a peak at  $\sim 3,200\text{ cm}^{-1}$ . Here, the bonding of F<sup>-</sup> atoms of CaF<sub>2</sub> and H atoms of interfacial water molecules is presented as a rationale for this peak. Although possible in our experiments due to the F<sup>-</sup> ions at the surface shown by XPS (Figure 5.3c), it is unlikely due to the lack of signal intensity from the plain CaF<sub>2</sub> substrates detailed in Figure 5.3d. This suggests the peak at  $\sim 3,200\text{ cm}^{-1}$  stems from hydrogen-bonding between interfacial water molecules and surface hydroxyl groups from the NiO overlayer. Spectra for the nickel films have been taken within days, weeks, and months using the same film resulting in the same feature at  $\sim 3,200\text{ cm}^{-1}$  (with variable intensities each time). As with the increased hydrophobicity of graphene, it is likely the presence of a tightly bound hydrogen-bonding network is independent of whether the surface is hydrophilic or hydrophobic.

In the study mentioned above, a peak at  $\sim 3600\text{ cm}^{-1}$  is also resolved and correlates with the increased hydrophobicity of the films.<sup>33</sup> This peak results in dangling O–H bonds which is often a result of hydrophobic surfaces. For our studies, features around  $\sim 3,600\text{ cm}^{-1}$  are subject to interference with the peak resulting from Fresnel factors. Therefore, although it is likely that the increased hydrophobicity of the films results in a change to

the interfacial hydrogen-bonding network, it is possible that we cannot probe this due to Fresnel factors.

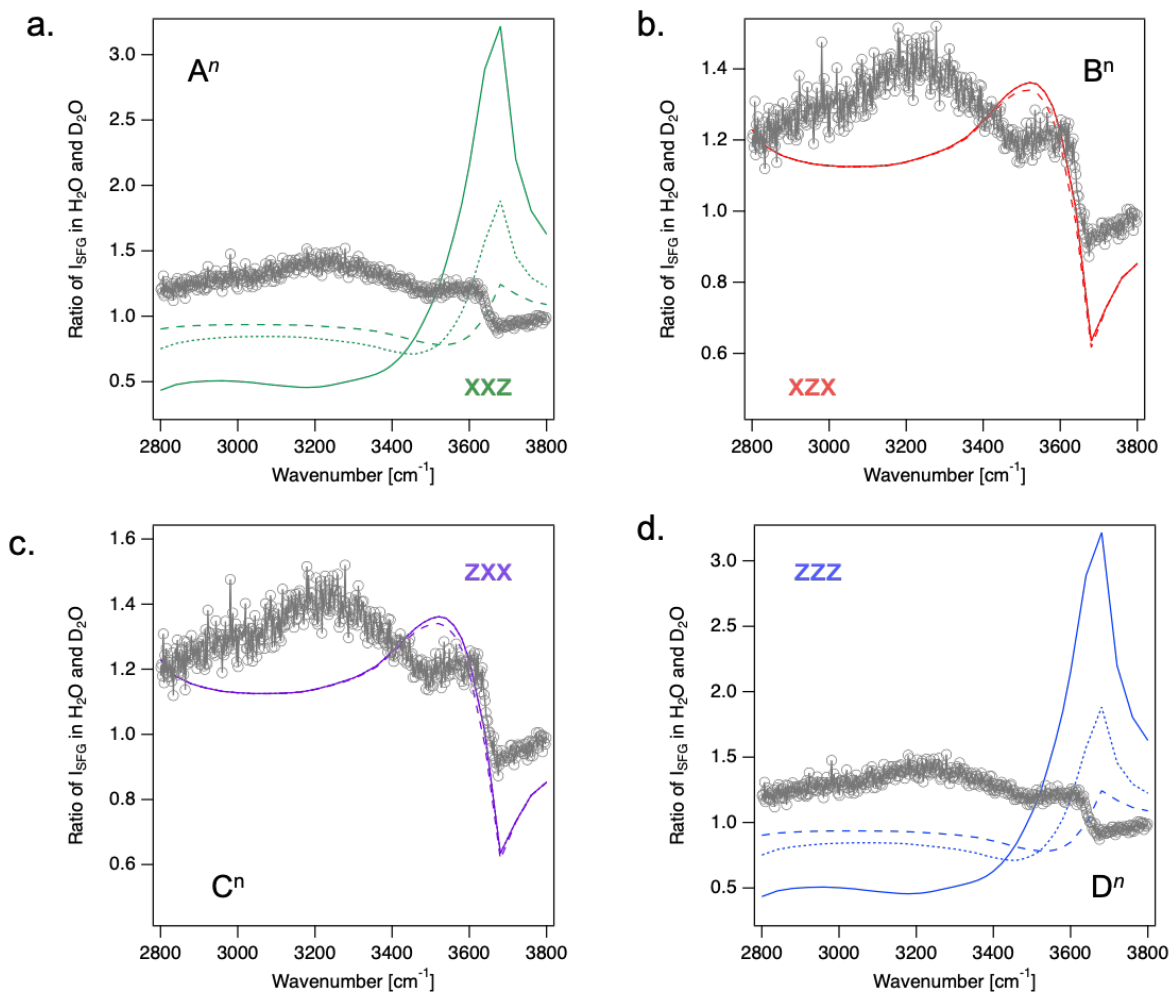


Figure 5.5. Calculations of the spectral coefficients represented by Equations 5.2.2–5.2.5 are shown with comparison to experimental results for the interaction of water with a Ni:NiOx film. Interface I is denoted by the dashed lines in each respective plot. Interface II is shown by the solid ( $\chi_{\text{water}}^{(2)} > \chi_{\text{Ni}}^{(2)}$ ) and dotted ( $\chi_{\text{Ni}}^{(2)} > \chi_{\text{water}}^{(2)}$ ) lines. The representative experimental SFG spectrum here (grey) is taken in PPP-polarization.

### 5.3.4. pH and Ionic Strength Effects on Nickel Nanolayers

To understand the nickel:nickel:oxide:water interface at more complex and realistic environments, our triple layer system was investigated at two different pH's and at two different ionic strength conditions of 0 mM and 100 mM NaCl. Due to their promising ability to produce electricity in the presence of a salinity gradient, these nanolayers have the potential to be implemented in oceans and other environments as an alternative energy source. The two pH's used here, pH 5.8 and pH 8.5, exemplify conditions of rainwater and ocean water respectively. The XPS and SFG results in the left column of Figure 5.6(a, c, and e) are results from a majority of the films sampled. The XPS results in Figure 5.6a show the presence of nickel metal (subsurface) underneath the NiO layer at the surface (which was detected but not shown here).<sup>34</sup> After the addition of 100 mM NaCl, there is no change to the interfacial hydrogen-bonding network at both pH 5.8 and 8.5. However, changes in pH does seem to result in some small, yet significant changes. The lineshapes for experiments done at pH 5.8 are more defined, whereas those at pH 8.5 are more broad and seemingly less intense. The PZC of Ni and NiO is somewhat variable in the literature, but has been found to be somewhere between pH 8–11.<sup>35</sup> Due to pH 8.5 being closer to the PZC, it is likely the surface is less charged, therefore, decreasing the electrostatic alignment of the interfacial water molecules. The difference due to pH also results in a slight shift in wavenumber, where, on average, the peak shifts to a slightly higher frequency with those at a pH of 5.8  $\sim 3,200 - 3,300 \text{ cm}^{-1}$  and those at a pH of 8.5  $\sim 3,300 - 3,400 \text{ cm}^{-1}$ . This is also likely due to pH 8.5 being close to the PZC of Ni and NiO. This would again likely result in weak ordering of the interfacial water molecules.

The right column of Figure 5.6 (b, d, and f) shows the data set from the oldest film sampled that was introduced to several rounds of water containing 100 mM NaCl. There is a striking difference between the XPS spectrum shown in Figure 5.6a and 5.6b, where the XPS spectrum of the subsurface composition of the older nickel film results in an XPS spectrum of NiO. Therefore, it is likely that the film used for the experiments in the right column had oxidized significantly more than any of the films likely due to the film age and a higher exposure to water and salt than any of the other films. The small spectral changes due to pH were found to be the same as those previously mentioned for the majority of films. However, for both pH 8.5 and 5.8 there is an increase in signal intensity with the addition of 100 mM NaCl, with the increase being more intense for the case of pH 8.5. As mentioned, the presence of fluorine atoms was determined at the surface for these nickel films (Figure 5.3c). In one study, the dissolution of F<sup>-</sup> atoms in the presence of NaCl at pH 6 (close to CaF<sub>2</sub> PZC) was found to enhance the CaF<sub>2</sub> surface charge due to exposed Ca<sup>2+</sup> sites. At pH 5.8, the nickel surface is also expected to be positively charged, and although there is screening due to the Cl<sup>-</sup> anions, the surface potential can outweigh the amount of available adsorbates resulting in the slight increase shown by Figure 5.6d. At pH 8.5, the increase is larger as shown by Figure 5.6f. At this pH, the surface should be uncharged. However, due to the projected large amounts of hydrocarbons at the surface of an old, heavily used film, it is likely that an accumulation of Cl<sup>-</sup> anions could occur at the interface as was seen for water interacting with hydrophobic materials such as octadecylsilane (OTS).<sup>36</sup> Future work focusing on monitoring film age and NiO composition after each experimental use should be done to further corroborate

these experiments, however, this insight has proven to be a powerful stepping-stone for an interface that was previously inaccessible.



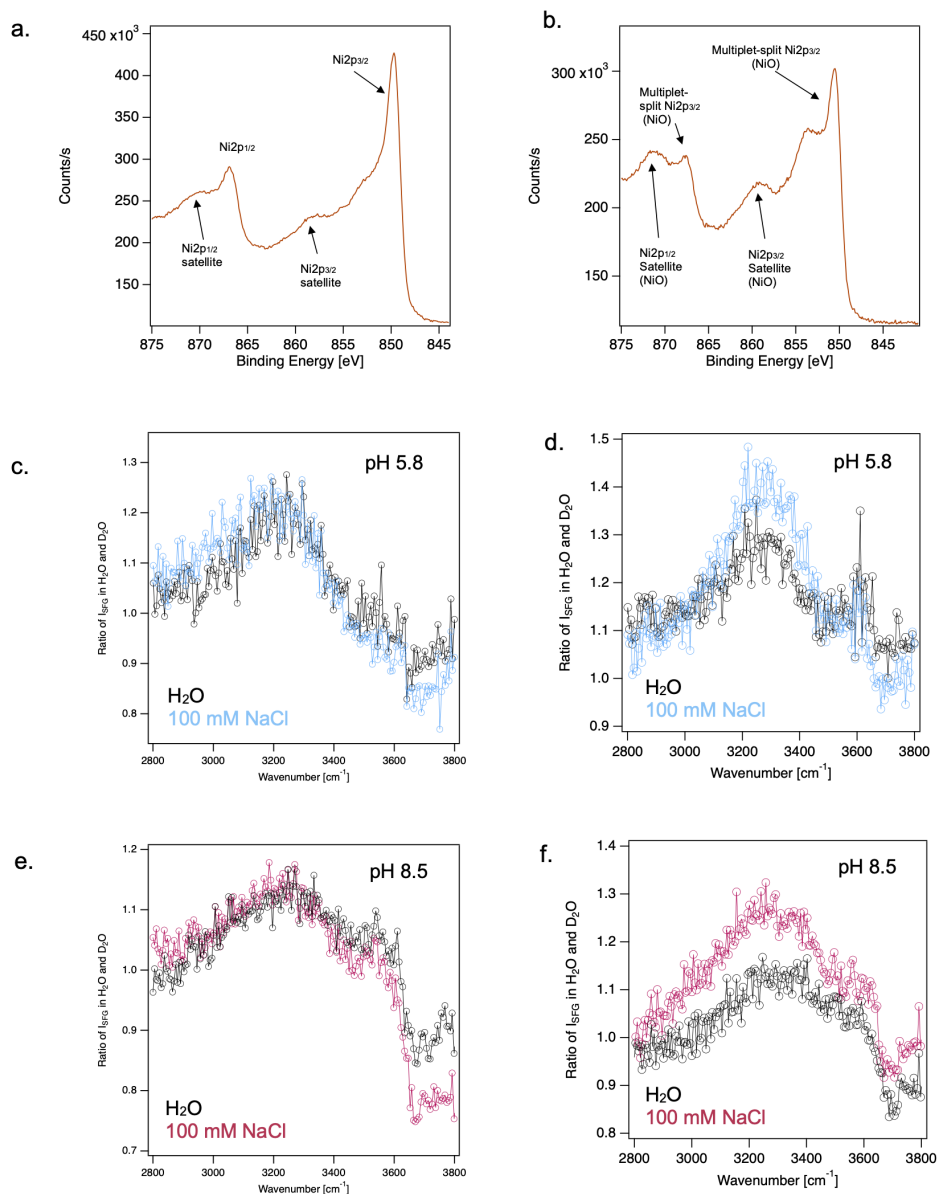


Figure 5.6. The subsurface XPS data reveals differences in a nickel film (a) that has been prepared more recently and exposed to less salt water than a film in (b). SFG spectra are binned during the acquisitions and taken in PPP-polarization. Films exposed to water and subsequently 100 mM NaCl at pH 5.8 and 8.5 are shown for a new film (c and e respectively) and an older film that has been introduced to salt several times (d and f respectively).

#### 5.4. Conclusion

In conclusion, the current work determined there to be an increase in hydrophobicity of the nickel nanolayers over time due to their ability to readily absorb hydrocarbons in ambient laboratory air. Nickel films that were  $\leq 4$  nm thick were used for SFG experiments due to their ability to transmit a significant amount of IR light. This was key in obtaining a spectrum for the hydrogen-bonding network for our set-up in internal reflection geometry. The presence of a peak due to Fresnel factors between  $3,600\text{ cm}^{-1}$  and  $3,800\text{ cm}^{-1}$  limited our ability to probe the dangling  $-\text{OH}$  bonds which are often present for hydrophobic surfaces. Instead, we monitored changes to the region between  $3,100\text{ cm}^{-1}$  to  $3,600\text{ cm}^{-1}$  at both pH 5.8 and 8.5 and determined there to be a peak shift from  $\sim 3,200 - 3,300\text{ cm}^{-1}$  at pH 5.8 to  $\sim 3,300 - 3,400\text{ cm}^{-1}$  at pH 8.5. This is likely due to the low surface charge, therefore, lack of electrostatic alignment around the PZC for Ni and NiO. For an older film that, unlike the majority of nickel films, showed the presence of NiO instead of Ni metal after surface etching, there was an increase in the peak intensity ( $\sim 3,200 - 3,300\text{ cm}^{-1}$  at pH 5.8 and  $\sim 3,300 - 3,400\text{ cm}^{-1}$  at pH 8.5) with the addition of 100 mM NaCl. This was not seen for films with an XPS spectrum of subsurface Ni metal. The increase for pH 5.8 could be the result of  $\text{F}^-$  dissolution from  $\text{CaF}_2$ ; for pH 8.5, the increase could be the result of  $\text{Cl}^-$  anion accumulation at the interface.

These experiments have laid the groundwork for future studies of metal:metal:oxide interfaces. As mentioned, it is possible that the subsequent experiments introducing salt and different pH's to the metal films can corrode and further oxidize them. Therefore, to focus on the metal film's electrochemical abilities without further modifying the film's surface chemistry, applying an external potential could be considered as a potential next

step. Lastly, heterodyned-detected second harmonic generation (HD-SHG) spectroscopy in conjunction with static potential measurements could be done in order to directly quantify the surface potential without fitting to models such as the Gouy–Chapman. This technique provides insight into the phase of the second harmonic response which could disentangle contributions from  $\chi^{(2)}$ , and  $\chi^{(3)}$ . Isolation of  $\chi^{(3)}$  would then, therefore, allow for the direct potential measurements mentioned above.

## CHAPTER 6

# Summary and Future Work: Investigating the Presence of Surface Hydroxyl Groups on the Nickel Surface

### 6.1. Introduction to Chapter 6

As was detailed in Chapter 5, in internal reflection geometry, the nickel nanolayers need to be  $< 5$  nm in order to transmit sufficient IR through the film for our experiments. In this geometry, insight on the dangling  $-OH$  bonds was not feasible due to interference from Fresnel factors. Therefore, to obtain insight on thicker films ( $\sim 10$  nm) and to understand the structure of the surface hydroxyl groups on the native oxide, experiments were also carried out in external geometry. Here, liquid water was not introduced into the system as water is a strong IR absorber. Instead, water vapor at  $\sim 90\%$  relative humidity (RH) was introduced to determine whether there was any discernible interaction between the NiOx overlayer and water layers formed at high RH. A dry condition (0% RH) was also recorded for comparison.

### 6.2. Background

The corrosion and dissolution of wet metal surfaces is often connected with the presence of surface hydroxyl groups in the native metal oxide that forms spontaneously on the metal surface. The costliness of corrosion has led to many efforts in studying polymers and self-assembled monolayers (SAMs) as coatings to protect the underlying metal

without compromising its function.<sup>1-3</sup> Atmospheric corrosion has been noted as the most expensive type of corrosion as moisture in the air and ligand exchange can stimulate dissolution.<sup>4</sup> In ambient air, the metal surface can be covered in multilayers of water which can modify the metal surface composition and structure. It was shown that on an  $\alpha$ -Al<sub>2</sub>O<sub>3</sub> surface at 80% relative humidity (RH), the surface was covered with  $\sim$ 8 monolayers of water at 300 K.<sup>5</sup>

In the literature, work has been done to elucidate surface hydroxyl groups from both metals and mineral oxides using sum frequency generation (SFG) spectroscopy.<sup>4,6-9</sup> One study was successful in probing these surface hydroxyl groups on a zinc surface, doing so at  $\sim$ 90% RH. In this work, ligand exchange between the surface hydroxyl groups and formate ligand (from the introduction of formic acid into the system) was also monitored successfully.<sup>4</sup> To this end, we are interested in analyzing the nickel oxide overlayer of  $\sim$ 10 nm nickel films to learn more about the species of hydroxyl groups that exist therein. The peaks between 3,600 cm<sup>-1</sup> and 3,700 cm<sup>-1</sup> are compared to literature values of surface hydroxyl groups found in single-crystal NiO.

## 6.3. Methods

### 6.3.1. Vibrational Sum Frequency Generation (SFG) Spectroscopy

Details of the laser system are mentioned in Chapters 3 and 5. As mentioned in Chapter 5, thin films of nickel are subject to burning at high IR powers ( $> 5 \mu\text{J}$ ). They can also burn when exposed to a tightly focused visible beam.<sup>10,11</sup> Here,  $\sim$ 10 nm films are used and are prone to the same issues of burning as shown by Figure 6.1. Therefore, the visible beam was again loosely focused. A quick measurement (using a ruler and white card)

of the beam diameter found it to be  $\sim 4$  mm. To ensure there were no distortions in the spectral features obtained from these measurements, the IR beam was moved across the spot, from points 1 to 5 as shown in Figure 6.2. In the figure, the best overlap between the visible and IR beams occurs at point 3. Here, we also obtain the highest sum frequency signal from point 3. As you move away from the best overlap, the signal begins to decrease, which is expected. In each spectrum, there is a peak at  $\sim 2,950$   $\text{cm}^{-1}$  (above the nonresonant nickel response) which is due to hydrocarbons from the natural lab environment (mentioned in Chapter 5 as well). The signal intensity of this peak is strongest at point 3, which is again expected as the overlap between the visible and IR beams is the best here. The presence of this feature at each point suggests there are no distortions due to the larger beam diameter. If the overlap is slightly off-center, we would still expect the same features to persist, without any new, unanticipated features also present. In Chapter 5, other control experiments were done for the  $\sim 5$  nm nickel films that showed the beam needed to be loosely focused but to a lesser degree (1–2 mm in diameter). However, this experiment was important in acknowledging that even a visible beam focused to  $\sim 4$  mm did not result in any distortions, therefore, this suggests the more focused beam used in Chapter 5 also did not result in any distortions.

To showcase the clear changes in the peak at  $\sim 2,950$   $\text{cm}^{-1}$ , the spectra shown in Figure 6.2 were not normalized to gold. However, after gold normalization, the features of the spectra remain the same regardless of overlap (just less intense for the spectra taken when the overlap was on the edge of the visible beam). The SFG spectra shown in the results section of this chapter are shown with normalization to gold.<sup>12</sup>

Along with the control experiment assessing any distortions due to the larger beam size, another control experiment was also done to assess whether all the features at a high visible power (2  $\mu\text{J}$ ) could be resolved at intermediate (1  $\mu\text{J}$ ) and low (0.5  $\mu\text{J}$ ) powers. This is also a precaution taken to prevent any burning of the films during long acquisition times. Figure 6.3 shows representative spectra for a 10 nm nickel film taken in PPP-polarization in air. The spectra taken at 1  $\mu\text{J}$  and 0.5  $\mu\text{J}$  replicate all the features present in the 2  $\mu\text{J}$  spectrum. Therefore, a power  $\sim 1$   $\mu\text{J}$  is used for all subsequent experiments. The spectral features resolved in the spectra are further analyzed in the results section.

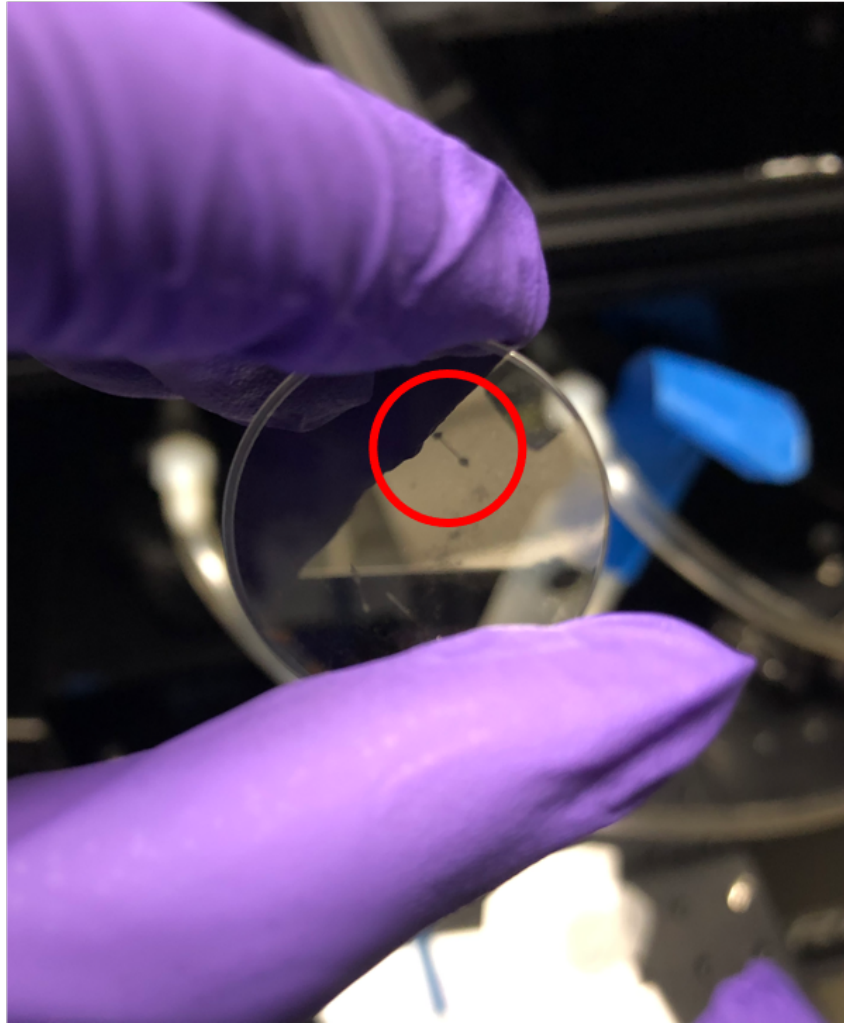


Figure 6.1. The  $\sim 10$  nm nickel films burn when exposed to high IR powers and tight visible focus as was mentioned for the  $\sim 5$  nm films in Chapter 5. The line between spots shows burning from simply moving the film from one spot to another using the sample stage.



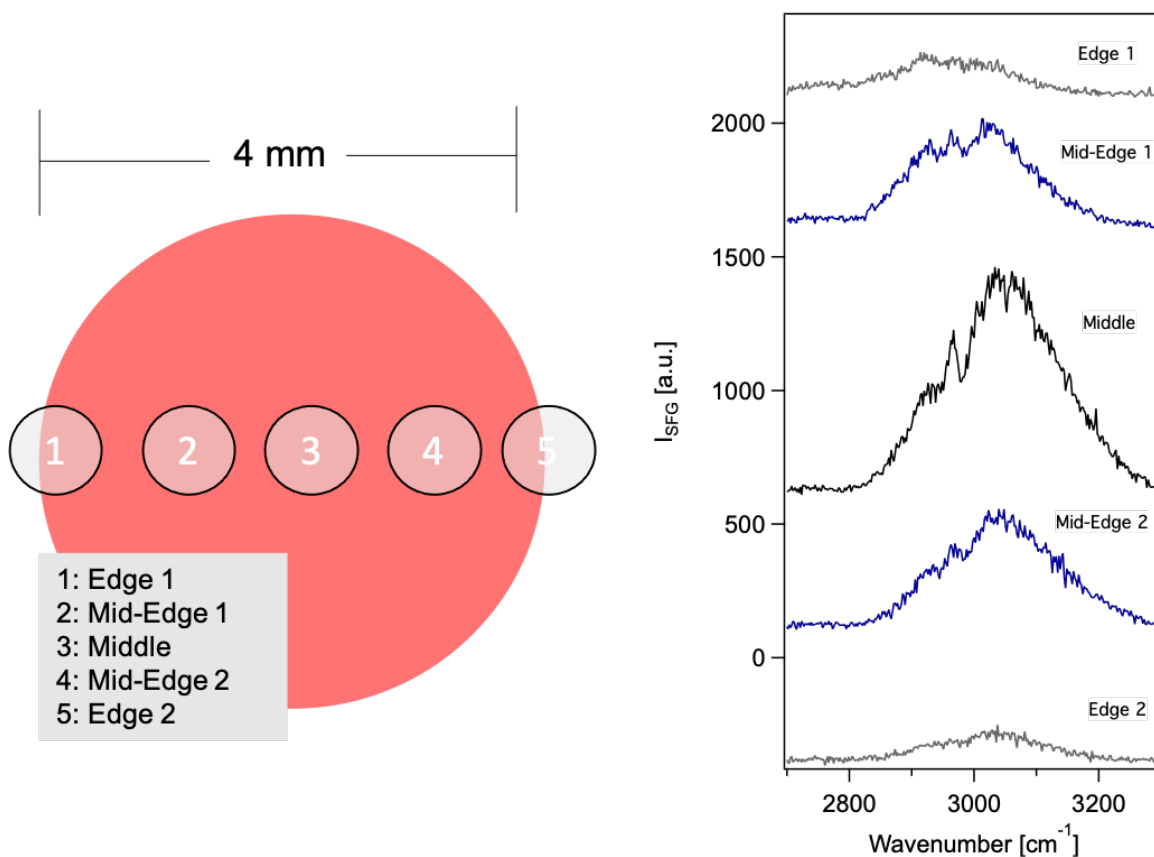


Figure 6.2. The red dot shown here represents the loosely focused visible beam with a diameter  $\sim 4$  mm. The small transparent white circles represent the IR beam moving across the spot from one edge to the other (from 1 to 5). The spectra taken in the C–H stretching region (1 DFG position) with PPP-polarization corresponds to each respective overlap position and is labeled for each position.

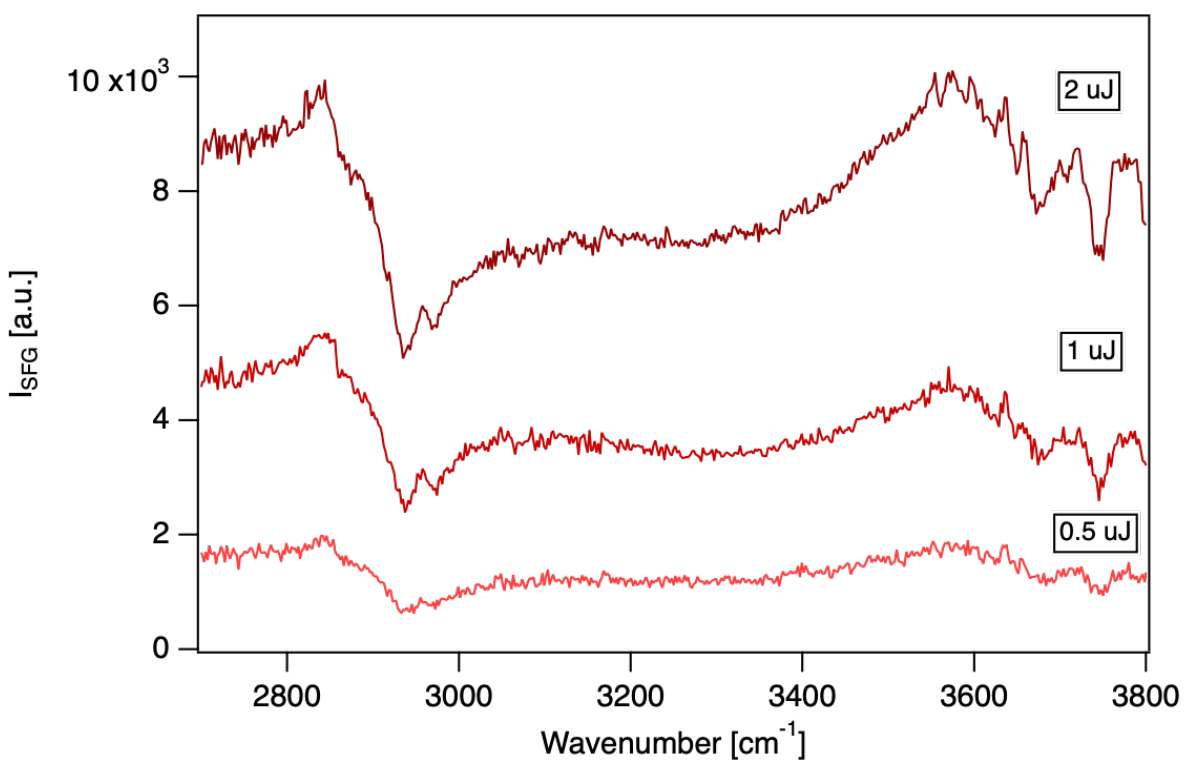


Figure 6.3. A control experiment in which the visible power is tuned to determine whether spectra taken at intermediate (1  $\mu\text{J}$ ) and low (0.5  $\mu\text{J}$ ) visible powers resolve all spectral features from the case of high (2  $\mu\text{J}$ ) visible power.

### 6.3.2. Flow Cell Set-Up

The features of the flow set-up have been previously reported and are briefly mentioned here.<sup>13,14</sup> As shown by Figure 6.4, a helium tank is connected to two paths. One path is a dry path and the other is wet path. In the wet path, helium flows through a bubbler containing  $\sim 10$  mL of water to carry the water vapor to the sample cell. For high RH conditions, the wet path is solely used. For the  $\sim 0\%$  RH condition, the dry path is used. The RH of the laboratory space is usually  $\sim 40\%$ , therefore helium is introduced to get it to  $0\%$  RH. The flow rates are controlled by mass flow controllers (MFCs) which detail the flow rate in SLPM (standard liter per minute).

### 6.3.3. Raman Microscopy

Raman spectra were taken using the Horiba LabRAM HR Evolution Confocal Raman Microscope. The spectra were taken for two ranges,  $200 - 1,000 \text{ cm}^{-1}$  and  $2,800 - 4,000 \text{ cm}^{-1}$ , using a  $633 \text{ nm}$  excitation wavelength with a  $100\times$  objective. For each film ( $10 \text{ nm}$  nickel on  $\text{CaF}_2$ ), 5 spots were taken for each range. The spectra were taken for 2 accumulations of  $30 \text{ s}$  and baseline corrected using linear fitting methods.

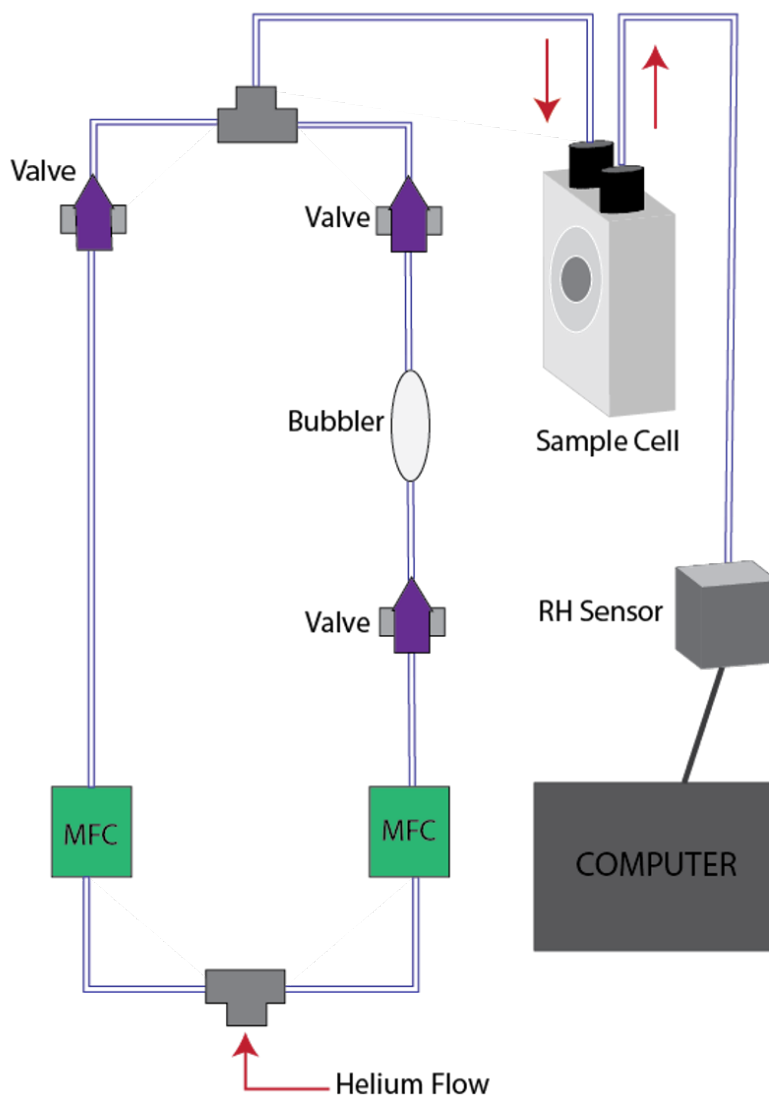


Figure 6.4. The above diagram details the flow-cell set-up used in the relative humidity experiments presented in this chapter. A helium tank is connected to allow the flow of helium through a dry (left) and wet (right) path. The flow rates are controlled with mass flow controllers (MFCs). Water vapor (or dry helium) enters the sample cell through one piece of tubing and exits through another. The RH sensor measures the RH of the sample chamber in real time and is sealed tightly. The sample sits in the cell in external geometry for the SFG experiments.

## 6.4. Preliminary Results and Discussion

### 6.4.1. Attempts to Elucidate Surface Hydroxyl Groups

As external geometry is used in these experiments, transmission through the film was not assessed as it was in Chapter 5. Here, Raman microscopy was used to characterize the films. In Figure 6.5a, there are two noticeable features in the provided Raman spectrum. The sharp feature  $\sim 321 \text{ cm}^{-1}$  is indicative of the  $\text{CaF}_2$  substrate that the films were prepared on.<sup>15</sup> There is also a much broader peak  $\sim 525 \text{ cm}^{-1}$  which represents the Ni–O stretching mode.<sup>16,17</sup> To assess the presence of any surface hydroxyl groups, Raman spectra in the  $2,800\text{--}4,000 \text{ cm}^{-1}$  region were also collected. As Figure 6.5b shows, there were no peaks resolved within this region. An excitation wavelength of 532 nm was also used in an attempt to probe the presence of surface hydroxyl groups, however, no spectral features were observed at this wavelength either. This data provides evidence to suggest that Raman spectroscopy isn't sensitive enough to elucidate surface hydroxyl groups on metal films only  $\sim 10 \text{ nm}$  thick.

SFG spectroscopy, a surface-selective technique (Chapter 2),<sup>18–20</sup> was then used in an effort to probe the surface hydroxyl groups. Figure 6.6a shows spectra taken at 3 different spots for a 10 nm nickel film in air. From the spectra, there are features shown within the  $2,800 - 3,100 \text{ cm}^{-1}$  regime, which, as mentioned, are indicative of the hydrocarbons from the ambient laboratory air. There are then several distinctive features shown between  $3,600 - 3,800 \text{ cm}^{-1}$ . This region is where we would expect to find peaks for surface hydroxyl groups. Two small, reproducible peaks are seen at  $\sim 3,640 \text{ cm}^{-1}$  and  $\sim 3,670 \text{ cm}^{-1}$  as shown by Figure 6.6b. There is also a much broader feature  $\sim 3,715 \text{ cm}^{-1}$  as well.

This feature may also be a combination of two peaks, however, it is not distinct enough to separate. The multiple peaks in the spectrum may be related to the coordination of the hydroxyl oxygen to a different number of metal atoms. In one study, three peaks were found for surface hydroxyl groups of crystalline NiO using IR spectroscopy:  $3,630\text{ cm}^{-1}$ ,  $3,690\text{ cm}^{-1}$ , and  $3,735\text{ cm}^{-1}$ .<sup>21</sup> In another study, only a peak at  $3,672\text{ cm}^{-1}$  was elucidated from silica supported nickel salts.<sup>22</sup> This peak was assigned to pure  $\text{Ni}(\text{OH})_2$ . More information about the surface is needed in order to confidently assign the peaks in the sum frequency spectra to specific surface hydroxyl groups.

#### 6.4.2. Relative Humidity Trials

To gain insight on any hydrogen-bonding or changes to the surface hydroxyl group composition at 90% vs. 0% relative humidity (RH), SFG experiments were conducted. Some preliminary results are shown in Figure 6.7 for both PPP- and SSP-polarizations. Unlike the polycrystalline zinc surface, the nickel surface did not show any signs of hydrogen-bonding as no new features were present between  $3,100\text{ cm}^{-1}$  and  $3,600\text{ cm}^{-1}$ . Furthermore, changes to the surface hydroxyl groups were also very minimal, with the spectra in Figure 6.7b showing a slight decrease in the peaks at  $\sim 3,640\text{ cm}^{-1}$  and  $\sim 3,670\text{ cm}^{-1}$  when going from 0% to 97% RH. Other trials have also been done and primarily show changes (if there are changes) to the peaks at  $\sim 3,640\text{ cm}^{-1}$  and  $\sim 3,670\text{ cm}^{-1}$ . The peak at  $3,715\text{ cm}^{-1}$  has typically remained unchanged. More experiments and characterization needs to be done, however, in order to draw further conclusions.

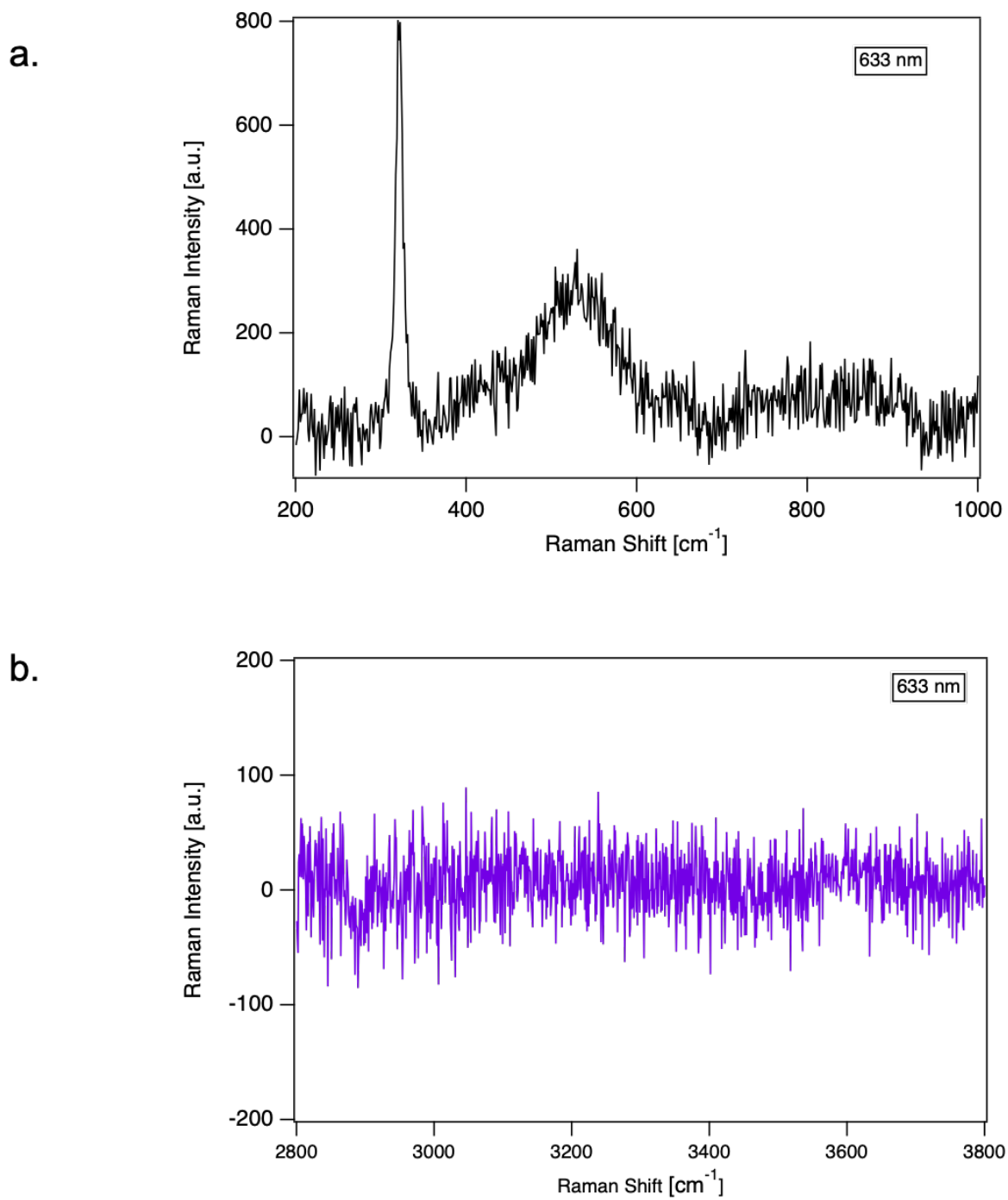


Figure 6.5. Representative Raman spectra of a  $\sim 10$  nm nickel film in the regions of interest for (a) nickel oxide and (b) nickel hydroxides.

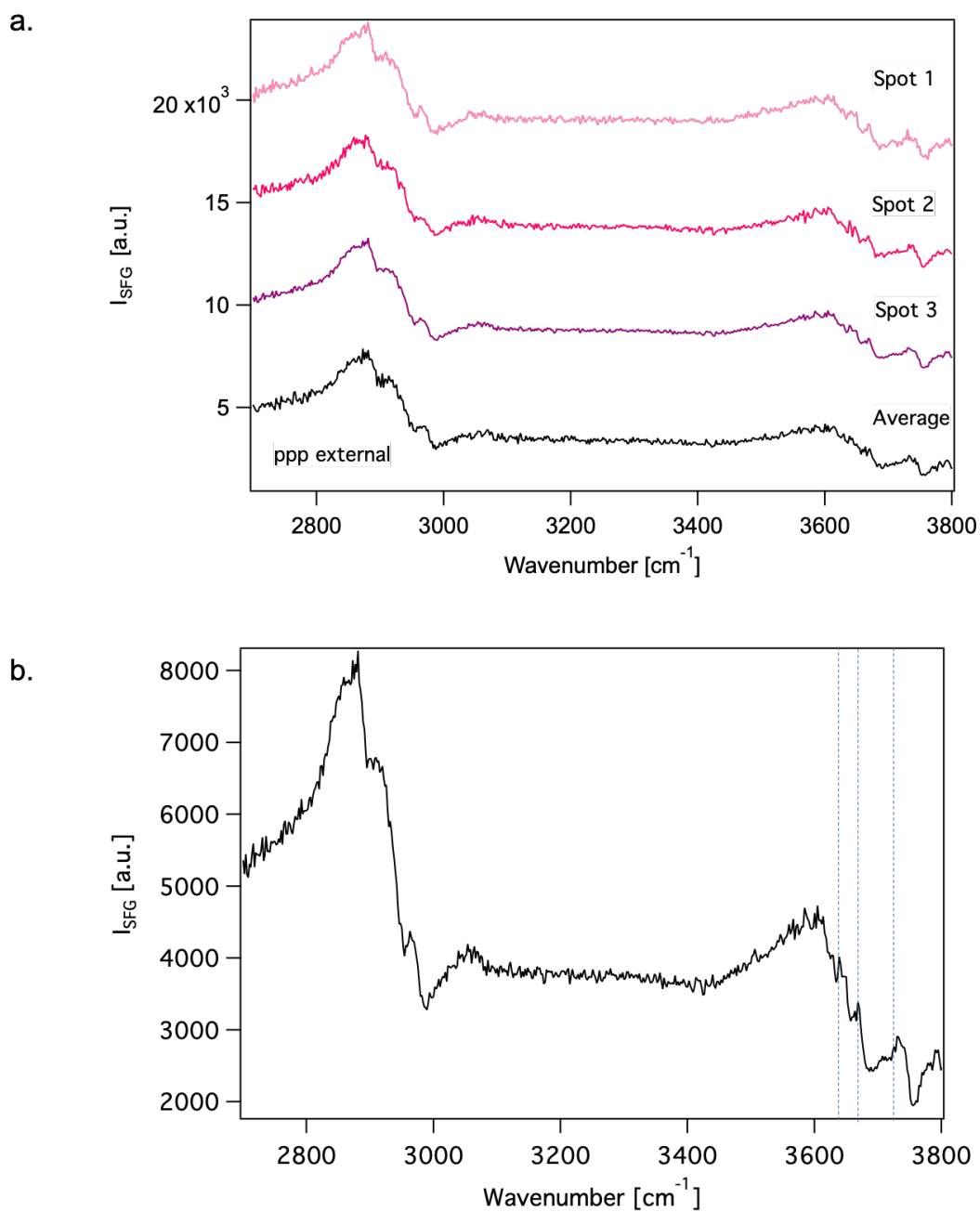


Figure 6.6. Representative SFG spectra of a 10 nm nickel film (on  $\text{CaF}_2$ ) taken in PPP-polarization at three different spots (a). The spots are averaged and shown by the black trace in (a). It is enlarged in (b) to showcase the 3 possible surface hydroxyl groups denoted by the blue dotted lines.



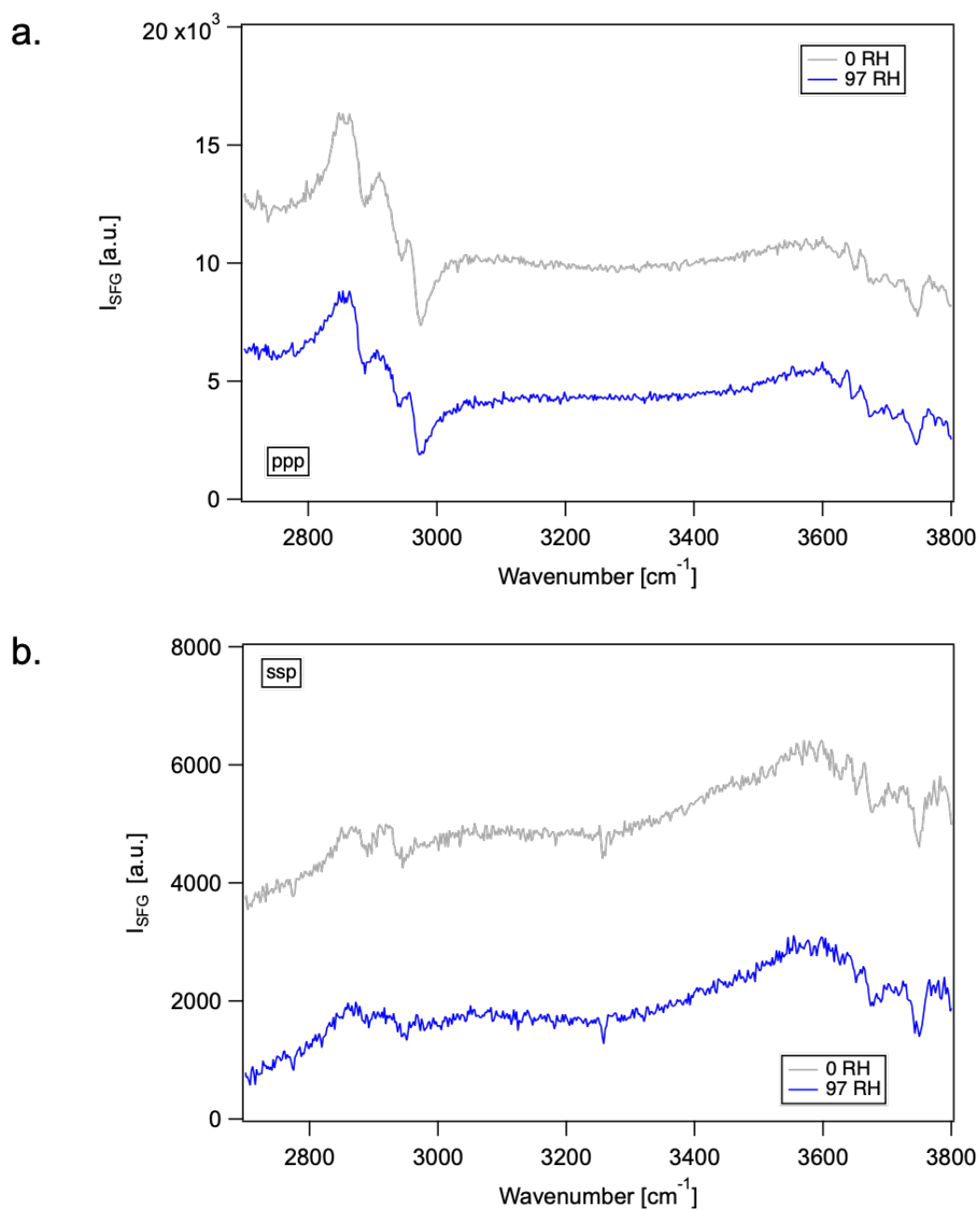


Figure 6.7. Representative relative humidity experiments conducted in (a) PPP- and (b) SSP-polarization.

## 6.5. Conclusions and Future Work

This chapter provides a framework for the conditions and set-up involved with conducting SFG experiments on thin metal nanolayers at different relative humidities. As mentioned in the results section, more experiments need to be done to accurately identify the surface hydroxyl groups. Once the hydroxyl groups are identified, it would be interesting to then compare them to those on an iron surface and also introduce organic acids such as oxalic acid into the system. As mentioned in Chapter 5, nanolayer thin films of nickel and iron can convert mechanical to electrical energy in the presence of a salinity gradient,<sup>23</sup> therefore, possible implementation can include oceans and coastal environments. Oxalic acid is one of many organic acids commonly found in soils.<sup>24</sup> This acid may contact the films and induce corrosion, therefore, it would be interesting to mechanistically understand how it interacts (if it interacts) with the metal surface hydroxyl groups.

## REFERENCES

### References for Chapter 1

- (1) Björneholm, O.; Hansen, M. H.; Hodgson, A.; Liu, L.-M.; Limmer, D. T.; Michaelides, A.; Pedevilla, P.; Rossmeisl, J.; Shen, H.; Tocci, G.; Tyrode, E.; Walz, M.-M.; Werner, J.; Bluhm, H. Water at Interfaces. *Chem. Rev.* **2016**, *116*, 7698–7726.
- (2) Gragson, D. E.; Richmond, G. L. Investigations of the structure and hydrogen bonding of water molecules at liquid surfaces by vibrational sum frequency spectroscopy. *J. Phys. Chem. B* **1998**, *102*, 3847–3861.
- (3) Stumm, W. Reactivity at the mineral-water interface: dissolution and inhibition. *Colloids Surf.* **1997**, *120*, 143–166.
- (4) Azam, M. S.; Cai, C.; Gibbs, J. M.; Tyrode, E.; Hore, D. K. Silica Surface Charge Enhancement at Elevated Temperatures Revealed by Interfacial Water Signals. *J. Am. Chem. Soc.* **2020**, *142*, 669–673.
- (5) Sulpizi, M.; Gageot, M.-P.; Sprik, M. The Silica-Water Interface: How the Silanols Determine the Surface Acidity and Modulate the Water Properties. *J. Chem. Theory Comput.* **2012**, *8*, 1037–1047.
- (6) Mondal, J. A.; Namboodiri, V.; Mathi, P.; Singh, A. K. Alkyl Chain Length Dependent Structural and Orientational Transformations of Water at Alcohol–Water

- Interfaces and Its Relevance to Atmospheric Aerosols. *J. Phys. Chem. Lett.* **2017**, *8*, 1637–1644.
- (7) Ishizuka, S.; Matsugi, A.; Hama, T.; Enami, S. Interfacial Water Mediates Oligomerization Pathways of Monoterpene Carbocations. *J. Phys. Chem. Lett.* **2020**, *11*, 67–74.
- (8) Manning, B. A.; Goldberg, S. Adsorption and Stability of Arsenic(III) at the Clay Mineral-Water Interface. *Environ. Sci. Technol.* **1997**, *31*, 2005–2011.
- (9) Pandey, R.; Usui, K.; Livingstone, R. A.; Fischer, S. A.; Pfaendtner, J.; Backus, E. H. G.; Nagata, Y.; Fröhlich-Nowoisky, J.; Schmäser, L.; Mauri, S.; Scheel, J. F.; Knopf, D. A.; Pöschl, U.; Bonn, M.; Weidner, T. Ice-nucleating bacteria control the order and dynamics of interfacial water. *Sci. Adv.* **2016**, *2*, e1501630.
- (10) Miller, Q. R. S.; Kaszuba, J. P.; Kerisit, S. N.; Schaef, H. T.; Bowden, M. E.; McGrail, B. P.; Rosso, K. M. Emerging investigator series: ion diffusivities in nanoconfined interfacial water films contribute to mineral carbonation thresholds. *Environ. Sci. Nano* **2020**, *7*, 1068–1081.
- (11) Tong, Y.; Lapointe, F.; Thamer, M.; Wolf, M.; Campen, R. K. Hydrophobic Water Probed Experimentally at the Gold Electrode/Aqueous Interface. *Angew. Chem. Int. Ed.* **2017**, *56*, 4211–4214.
- (12) Dreier, L.; Liu, Z.; Narita, A.; Zadel, M.-J. v.; Mullen, K.; Tielrooij, K.-J.; Backus, E.; Bonn, M. Surface-Specific Spectroscopy of Water at a Potentiostatically Controlled Supported Graphene Monolayer. *J. Phys. Chem. C* **2019**, *123*, 24031–24038.

- (13) Wallentine, S.; Bandaranayake, S.; Biswas, S.; Baker, L. R. Plasmon-Resonant Vibrational Sum Frequency Generation of Electrochemical Interfaces: Direct Observation of Carbon Dioxide Electroreduction on Gold. *J. Phys. Chem A* **2020**, *124*, 8057–8064.
- (14) Noguchi, H.; Okada, T.; Uosaki, K. Molecular structure at electrode/electrolyte solution interfaces related to electrocatalysis. *Faraday Discuss.* **2009**, *140*, 125–137.
- (15) Thennarasu, S.; Huang, R.; Lee, D.-K.; Yang, P.; Maloy, L.; Chen, Z.; Ramamoorthy, A. Limiting an Antimicrobial Peptide to the Lipid-Water Interface Enhances Its Bacterial Membrane Selectivity: A Case Study of MSI-367. *Biochemistry* **2010**, *49*, 10595–10605.
- (16) Osborne, D. G.; Dunbar, J. A.; Lapping, J. G.; White, A. M.; Kubarych, K. J. Site-Specific Measurements of Lipid Membrane Interfacial Water Dynamics with Multi-dimensional Infrared Spectroscopy. *J. Phys. Chem. B* **2013**, *117*, 15407–15414.
- (17) Ghosh, A.; Campen, R. K.; Sovago, M.; Bonn, M. Structure and dynamics of interfacial water in model lung surfactants. *Faraday Discuss.* **2009**, *141*, 145–159.
- (18) Hauner, I. M.; Deblais, A.; Beattie, J. K.; Kellay, H.; Bonn, D. The Dynamic Surface Tension of Water. *J. Phys. Chem. Lett.* **2017**, *8*, 1599–1603.
- (19) Franks, F. In *The Physics and Physical Chemistry of Water*; Springer: 1972, pp 1–20.
- (20) Ostroverkhov, V.; Waychunas, G. A.; Shen, Y. R. Vibrational spectra of water at water/ $\alpha$ -quartz (0001) interface. *Chem. Phys. Lett.* **2004**, *386*, 144–148.

- (21) Covert, P. A.; Jena, K. C.; Hore, D. K. Throwing Salt into the Mix: Altering Interfacial Water Structure by Electrolyte Addition. *J. Phys. Chem. Lett.* **2014**, *5*, 143–148.
- (22) Dewan, S.; Yeganeh, M. S.; Borguet, E. Experimental Correlation Between Interfacial Water Structure and Mineral Reactivity. *J. Phys. Chem. Lett.* **2013**, *4*, 1977–1982.
- (23) Kim, D.; Kim, E.; Park, S.; Kim, S.; Min, B. K.; Yoon, H. J.; Kwak, K.; Cho, M. Wettability of graphene and interfacial water structure. *Chem* **2021**, *7*, 1602–1614.
- (24) Richmond, G. L. Molecular bonding and interactions at aqueous surfaces as probed by vibrational sum frequency spectroscopy. *Chem. Rev.* **2002**, *102*, 2693–2724.
- (25) Tian, C. S.; Shen, Y. R. Structure and charging of hydrophobic material/water interfaces studied by phase-sensitive sum-frequency vibrational spectroscopy. *Proc. Natl. Acad. Sci.* **2009**, *106*, 15148.
- (26) Uosaki, K.; Yano, T.; Nihonyanagi, S. Interfacial Water Structure at As-Prepared and UV-Induced Hydrophilic TiO<sub>2</sub> Surfaces Studied by Sum Frequency Generation Spectroscopy and Quartz Crystal Microbalance. *J. Phys. Chem. B* **2004**, *108*, 19086–19088.
- (27) Gonella, G.; Backus, E. H. G.; Nagata, Y.; Bonthuis, D. J.; Loche, P.; Schlaich, A.; Netz, R. R.; Kühnle, A.; McCrum, I. T.; Koper, M. T. M.; Wolf, M.; Winter, B.; Meijer, G.; Campen, R. K.; Bonn, M. Water at charged interfaces. *Nat. Rev. Chem.* **2021**, *5*, 466–485.
- (28) Hopkins, A. J.; Schrödle, S.; Richmond, G. L. Specific Ion Effects of Salt Solutions at the CaF<sub>2</sub>/Water Interface. *Langmuir* **2010**, *26*, 10784–10790.

- (29) Jena, K. C.; Hore, D. K. Variation of Ionic Strength Reveals the Interfacial Water Structure at a Charged Mineral Surface. *J. Phys. Chem. C* **2009**, *113*, 15364–15372.
- (30) Schaefer, J.; Gonella, G.; Bonn, M.; Backus, E. H. G. Surface-specific vibrational spectroscopy of the water/silica interface: screening and interference. *Phys. Chem. Chem. Phys.* **2017**, *19*, 16875–16880.
- (31) Coreño, J.; Martínez, A.; Bolarín, A.; Sánchez, F. Apatite nucleation on silica surface: A  $\zeta$  potential approach. *J. Biomed. Mater. Res.* **2001**, *57*, 119–125.
- (32) Nel, A. E.; Mädler, L.; Velegol, D.; Xia, T.; Hoek, E. M. V.; Somasundaran, P.; Klaessig, F.; Castranova, V.; Thompson, M. Understanding biophysicochemical interactions at the nano–bio interface. *Nat. Mater.* **2009**, *8*, 543–557.
- (33) Das, M.; Shim, K. H.; An, S. S. A.; Yi, D. K. Review on gold nanoparticles and their applications. *Toxicol. Environ. Health Sci.* **2011**, *3*, 193–205.
- (34) Yin, J.; Qi, X.; Yang, L.; Hao, G.; Li, J.; Zhong, J. A hydrogen peroxide electrochemical sensor based on silver nanoparticles decorated silicon nanowire arrays. *Electrochim. Acta* **2011**, *56*, 3884–3889.
- (35) Silva, T. R.; Brondani, D.; Zapp, E.; Vieira, I. C. Electrochemical Sensor Based on Gold Nanoparticles Stabilized in Poly(Allylamine hydrochloride) for Determination of Vanillin. *Electroanalysis* **2015**, *27*, 465–472.
- (36) Abadeer, N. S.; Murphy, C. J. Recent Progress in Cancer Thermal Therapy Using Gold Nanoparticles. *J. Phys. Chem. C* **2016**, *120*, 4691–4716.
- (37) Cui, A. Y.; Cui, Q. Modulation of Nanoparticle Diffusion by Surface Ligand Length and Charge: Analysis with Molecular Dynamics Simulations. *J. Phys. Chem. B* **2021**, *125*, 4555–4565.

- (38) Lochbaum, C. A.; Chew, A. K.; Zhang, X.; Rotello, V.; Van Lehn, R. C.; Pedersen, J. A. Lipophilicity of Cationic Ligands Promotes Irreversible Adsorption of Nanoparticles to Lipid Bilayers. *ACS Nano* **2021**, *15*, 6562–6572.
- (39) Qiu, T. A.; Torelli, M. D.; Vartanian, A. M.; Rackstraw, N. B.; Buchman, J. T.; Jacob, L. M.; Murphy, C. J.; Hamers, R. J.; Haynes, C. L. Quantification of Free Polyelectrolytes Present in Colloidal Suspension, Revealing a Source of Toxic Responses for Polyelectrolyte-Wrapped Gold Nanoparticles. *Anal. Chem.* **2017**, *89*, 1823–1830.
- (40) Troiano, J. M. et al. Direct Probes of 4 nm Diameter Gold Nanoparticles Interacting with Supported Lipid Bilayers. *J. Phys. Chem. C* **2014**, *119*, 534–546.
- (41) Buchman, J. T.; Rahnamoun, A.; Landy, K. M.; Zhang, X.; Vartanian, A. M.; Jacob, L. M.; Murphy, C. J.; Hernandez, R.; Haynes, C. L. Using an environmentally-relevant panel of Gram-negative bacteria to access the toxicity of polyallylamine hydrochloride-wrapped gold nanoparticles. *Environ. Sci. Nano* **2018**, *5*, 279–288.
- (42) Hamers, R. J. Nanomaterials and Global Sustainability. *Acc. Chem. Res.* **2017**, *50*, 633–637.
- (43) Yang, Y.; Westerhoff, P. In *Nanomaterial: Impacts on Cell Biology and Medicine*, Capco, D. G., Chen, Y., Eds.; Springer Netherlands: Dordrecht, 2014, pp 1–17.
- (44) Tarun, O. B.; Hanneschläger, C.; Pohl, P.; Roke, S. Label-free and charge-sensitive dynamic imaging of lipid membrane hydration on millisecond time scales. *Proc. Natl. Acad. Sci.* **2018**, *115*, 4081.
- (45) Marrink, S.-J.; Berendsen, H. J. Simulation of water transport through a lipid membrane. *J. Phys. Chem.* **1994**, *98*, 4155–4168.



- (46) Mondal, J. A.; Nihonyanagi, S.; Yamaguchi, S.; Tahara, T. Three Distinct Water Structures at a Zwitterionic Lipid/Water Interface Revealed by Heterodyne-Detected Vibrational Sum Frequency Generation. *J. Am. Chem. Soc.* **2012**, *134*, 7842–7850.
- (47) Ishiyama, T.; Terada, D.; Morita, A. Hydrogen-Bonding Structure at Zwitterionic Lipid/Water Interface. *J. Phys. Chem. Lett.* **2016**, *7*, 216–220.
- (48) Worcester, D. L.; Franks, N. P. Structural analysis of hydrated egg lecithin and cholesterol bilayers II. Neutron diffraction. *J. Mol. Biol.* **1976**, *100*, 359–378.
- (49) Kiselev, M. A.; Ryabova, N. Y.; Balagurov, A. M.; Dante, S.; Hauss, T.; Zbytovska, J.; Wartewig, S.; Neubert, R. H. H. New insights into the structure and hydration of a stratum corneum lipid model membrane by neutron diffraction. *Eur. Biophys. J.* **2005**, *34*, 1030–1040.
- (50) Stubbs, C. D.; Ho, C.; Slater, S. J. Fluorescence techniques for probing water penetration into lipid bilayers. *J. Fluoresc.* **1995**, *5*, 19–28.
- (51) Kanti De, S.; Kanwa, N.; Ahamed, M.; Chakraborty, A. Spectroscopic evidence for hydration and dehydration of lipid bilayers upon interaction with metal ions: a new physical insight. *Phys. Chem. Chem. Phys.* **2018**, *20*, 14796–14807.
- (52) Bouvrais, H.; Pott, T.; Bagatolli, L. A.; Ipsen, J. H.; Méléard, P. Impact of membrane-anchored fluorescent probes on the mechanical properties of lipid bilayers. *Biochim. Biophys. Acta* **2010**, *1798*, 1333–1337.
- (53) Doğangün, M.; Ohno, P. E.; Liang, D.; McGeachy, A. C.; Bé, A. G.; Dalchand, N.; Li, T.; Cui, Q.; Geiger, F. M. Hydrogen-Bond Networks near Supported Lipid

- Bilayers from Vibrational Sum Frequency Generation Experiments and Atomistic Simulations. *J. Phys. Chem. B* **2018**, *122*, 4870–4879.
- (54) Geiger, F. M. Second Harmonic Generation, Sum Frequency Generation, and  $\chi^{(3)}$ : Dissecting Environmental Interfaces with a Nonlinear Optical Swiss Army Knife. *Annu. Rev. Phys. Chem.* **2009**, *60*, 61–83.
- (55) Olenick, L. L.; Chase, H. M.; Fu, L.; Zhang, Y.; McGeachy, A. C.; Dogangun, M.; Walter, S. R.; Wang, H.; Geiger, F. M. Single-component supported lipid bilayers probed using broadband nonlinear optics. *Phys. Chem. Chem. Phys.* **2018**, *20*, 3063–3072.
- (56) Dogangun, M.; Hang, M. N.; Machesky, J.; McGeachy, A. C.; Dalchand, N.; Hamers, R. J.; Geiger, F. M. Evidence for Considerable Metal Cation Concentrations from Lithium Intercalation Compounds in the Nano-Bio Interface Gap. *J. Phys. Chem. C* **2017**, *121*, 27473–27482.
- (57) Dalchand, N.; Doğangün, M.; Ohno, P. E.; Ma, E.; Martinson, A. B. F.; Geiger, F. M. Perturbation of Hydrogen-Bonding Networks over Supported Lipid Bilayers by Poly(allylamine hydrochloride). *J. Phys. Chem. B* **2019**, *123*, 4251–4257.
- (58) Nihonyanagi, S.; Yamaguchi, S.; Tahara, T. Direct evidence for orientational flip-flop of water molecules at charged interfaces: A heterodyne-detected vibrational sum frequency generation study. *J. Chem. Phys.* **2009**, *130*, 204704.
- (59) Castellana, E. T.; Cremer, P. S. Solid supported lipid bilayers: From biophysical studies to sensor design. *Surf. Sci. Rep.* **2006**, *61*, 429–444.

- (60) Schönherr, H.; Johnson, J. M.; Lenz, P.; Frank, C. W.; Boxer, S. G. Vesicle Adsorption and Lipid Bilayer Formation on Glass Studied by Atomic Force Microscopy. *Langmuir* **2004**, *20*, 11600–11606.
- (61) Bhide, S. Y.; Berkowitz, M. L. Structure and dynamics of water at the interface with phospholipid bilayers. *J. Chem. Phys.* **2005**, *123*, 224702.
- (62) Pandit, S. A.; Berkowitz, M. L. Molecular Dynamics Simulation of Dipalmitoylphosphatidylserine Bilayer with Na<sup>+</sup> Counterions. *Biophys. J.* **2002**, *82*, 1818–1827.
- (63) Boamah, M. D.; Isheim, D.; Geiger, F. M. Dendritic Oxide Growth in Zerovalent Iron Nanofilms Revealed by Atom Probe Tomography. *J. Phys. Chem. C* **2018**, *122*, 28225–28232.
- (64) Bohling, C.; Sigmund, W. Self-Limitation of Native Oxides Explained. *Silicon* **2016**, *8*, 339–343.
- (65) Boamah, M. D.; Lozier, E. H.; Kim, J.; Ohno, P. E.; Walker, C. E.; Miller, T. F.; Geiger, F. M. Energy conversion via metal nanolayers. *Proc. Natl. Acad. Sci.* **2019**, *116*, 16210–16215.
- (66) Yin, J.; Li, X.; Yu, J.; Zhang, Z.; Zhou, J.; Guo, W. Generating electricity by moving a droplet of ionic liquid along graphene. *Nature Nanotech.* **2014**, *9*, 378–383.
- (67) Tang, Q.; Yang, P. The era of water-enabled electricity generation from graphene. *J. Mater. Chem. A* **2016**, *4*, 9730–9738.
- (68) Zhang, Z.; Li, X.; Yin, J.; Xu, Y.; Fei, W.; Xue, M.; Wang, Q.; Zhou, J.; Guo, W. Emerging hydrovoltaic technology. *Nature Nanotech.* **2018**, *13*, 1109–1119.
- (69) Hodgson, A.; Haq, S. Water adsorption and the wetting of metal surfaces. *Surf. Sci. Rep.* **2009**, *64*, 381–451.

- (70) Carrasco, J.; Hodgson, A.; Michaelides, A. A molecular perspective of water at metal interfaces. *Nature Mater.* **2012**, *11*, 667–674.
- (71) Michaelides, A.; Morgenstern, K. Ice nanoclusters at hydrophobic metal surfaces. *Nat. Mater.* **2007**, *6*, 597–601.
- (72) Guo, J.; Bian, K.; Lin, Z.; Jiang, Y. Perspective: Structure and dynamics of water at surfaces probed by scanning tunneling microscopy and spectroscopy. *J. Chem. Phys.* **2016**, *145*, 160901.
- (73) Backus, E. H. G.; Garcia-Araez, N.; Bonn, M.; Bakker, H. J. On the Role of Fresnel Factors in Sum-Frequency Generation Spectroscopy of Metal-Water and Metal-Oxide-Water Interfaces. *J. Phys. Chem. C* **2012**, *116*, 23351–23361.

## References for Chapter 2

- (1) Zhuang, X.; Miranda, P. B.; Kim, D.; Shen, Y. R. Mapping molecular orientation and conformation at interfaces by surface nonlinear optics. *Phys. Rev. B* **1999**, *59*, 12632–12640.
- (2) Lambert, A. G.; Davies, P. B.; Neivandt, D. J. Implementing the Theory of Sum Frequency Generation Vibrational Spectroscopy: A Tutorial Review. *Appl. Spectrosc. Rev.* **2005**, *40*, 103–145.
- (3) Eienthal, K. B. Equilibrium and dynamic processes at interfaces by second harmonic and sum frequency generation. *Annu. Rev. Phys. Chem.* **1992**, *43*, 627–661.
- (4) Morita, A., *Theory of Sum Frequency Generation Spectroscopy*; Springer: 2018; Vol. 35.
- (5) Geiger, F. M. Second Harmonic Generation, Sum Frequency Generation, and  $\chi^{(3)}$ : Dissecting Environmental Interfaces with a Nonlinear Optical Swiss Army Knife. *Annu. Rev. Phys. Chem.* **2009**, *60*, 61–83.
- (6) Wang, H.-f.; Velarde, L.; Gan, W.; Fu, L. Quantitative Sum-Frequency Generation Vibrational Spectroscopy of Molecular Surfaces and Interfaces: Lineshape, Polarization, and Orientation. *Annu. Rev. Phys. Chem.* **2015**, *66*, 189–216.
- (7) Lee, C. M.; Kubicki, J. D.; Fan, B.; Zhong, L.; Jarvis, M. C.; Kim, S. H. Hydrogen-Bonding Network and OH Stretch Vibration of Cellulose: Comparison of Computational Modeling with Polarized IR and SFG Spectra. *J. Phys. Chem. B* **2015**, *119*, 15138–15149.

- (8) Chen, X.; Wang, J.; Boughton, A. P.; Kristalyn, C. B.; Chen, Z. Multiple Orientation of Melittin inside a Single Lipid Bilayer Determined by Combined Vibrational Spectroscopic Studies. *J. Am. Chem. Soc.* **2007**, *129*, 1420–1427.
- (9) Wang, J.; Chen, C.; Buck, S. M.; Chen, Z. Molecular Chemical Structure on Poly(methyl methacrylate) (PMMA) Surface Studied by Sum Frequency Generation (SFG) Vibrational Spectroscopy. *J. Phys. Chem. B* **2001**, *105*, 12118–12125.
- (10) Lu, X.; Shephard, N.; Han, J.; Xue, G.; Chen, Z. Probing Molecular Structures of Polymer/Metal Interfaces by Sum Frequency Generation Vibrational Spectroscopy. *Macromolecules* **2008**, *41*, 8770–8777.
- (11) Briggman, K. A.; Stephenson, J. C.; Wallace, W. E.; Richter, L. J. Absolute Molecular Orientational Distribution of the Polystyrene Surface. *J. Phys. Chem. B* **2001**, *105*, 2785–2791.
- (12) Han, H.; Peng, M.; Hu, Y.; Nguyen, A. V.; Sun, W. An SFG spectroscopy study of the interfacial water structure and the adsorption of sodium silicate at the fluorite and silica surfaces. *Miner. Eng.* **2019**, *138*, 178–187.
- (13) Dreier, L.; Liu, Z.; Narita, A.; Zadel, M.-J. v.; Mullen, K.; Tielrooij, K.-J.; Backus, E.; Bonn, M. Surface-Specific Spectroscopy of Water at a Potentiostatically Controlled Supported Graphene Monolayer. *J. Phys. Chem. C* **2019**, *123*, 24031–24038.
- (14) Tong, Y.; Lapointe, F.; Thamer, M.; Wolf, M.; Campen, R. K. Hydrophobic Water Probed Experimentally at the Gold Electrode/Aqueous Interface. *Angew. Chem. Int. Ed.* **2017**, *56*, 4211–4214.

- (15) Baldelli, S. Probing Electric Fields at the Ionic Liquid-Electrode Interface Using Sum Frequency Generation Spectroscopy and Electrochemistry. *J. Phys. Chem. B* **2005**, *109*, 13049–13051.
- (16) Huang-Fu, Z.-C.; Song, Q.-T.; He, Y.-H.; Wang, J.-J.; Ye, J.-Y.; Zhou, Z.-Y.; Sun, S.-G.; Wang, Z.-H. Electrochemical CO<sub>2</sub> reduction on Cu and Au electrodes studied using in situ sum frequency generation spectroscopy. *Phys. Chem. Chem. Phys.* **2019**, *21*, 25047–25053.
- (17) Bé, A. G.; Chase, H. M.; Liu, Y.; Upshur, M. A.; Zhang, Y.; Tuladhar, A.; Chase, Z. A.; Bellcross, A. D.; Wang, H.-F.; Wang, Z.; Batista, V. S.; Martin, S. T.; Thomson, R. J.; Geiger, F. M. Atmospheric  $\beta$ -Caryophyllene-Derived Ozonolysis Products at Interfaces. *ACS Earth Space Chem.* **2019**, *3*, 158–169.
- (18) Voges, A. B.; Stokes, G. Y.; Gibbs-Davis, J. M.; Lettan, R. B.; Bertin, P. A.; Pike, R. C.; Nguyen, S. T.; Scheidt, K. A.; Geiger, F. M. Insights into Heterogeneous Atmospheric Oxidation Chemistry: Development of a Tailor-Made Synthetic Model for Studying Tropospheric Surface Chemistry. *J. Phys. Chem. C* **2007**, *111*, 1567–1578.
- (19) Jubb, A. M.; Hua, W.; Allen, H. C. Environmental Chemistry at Vapor/Water Interfaces: Insights from Vibrational Sum Frequency Generation Spectroscopy. *Annu. Rev. Phys. Chem.* **2012**, *63*, 107–130.
- (20) Ho, J.; Psciuk, B. T.; Chase, H. M.; Rudshiteyn, B.; Upshur, M. A.; Fu, L.; Thomson, R. J.; Wang, H.-F.; Geiger, F. M.; Batista, V. S. Sum Frequency Generation Spectroscopy and Molecular Dynamics Simulations Reveal a Rotationally Fluid Adsorption State of  $\alpha$ -Pinene on Silica. *J. Phys. Chem. C* **2016**, *120*, 12578–12589.

- (21) Olenick, L. L. et al. Lipid Corona Formation from Nanoparticle Interactions with Bilayers. *Chem* **2018**, *4*, 1–15.
- (22) Liu, J.; Conboy, J. C. Direct Measurement of the Transbilayer Movement of Phospholipids by Sum-Frequency Vibrational Spectroscopy. *J. Am. Chem. Soc.* **2004**, *126*, 8376–8377.
- (23) Dogangun, M.; Ohno, P. E.; Liang, D.; McGeachy, A. C.; Be, A. G.; Dalchand, N.; Li, T.; Cui, Q.; Geiger, F. M. Hydrogen-Bond Networks near Supported Lipid Bilayers from Vibrational Sum Frequency Generation Experiments and Atomistic Simulations. *J. Phys. Chem. B* **2018**, *122*, 4870–4879.
- (24) Dogangun, M.; Hang, M. N.; Machesky, J.; McGeachy, A. C.; Dalchand, N.; Hamers, R. J.; Geiger, F. M. Evidence for Considerable Metal Cation Concentrations from Lithium Intercalation Compounds in the Nano-Bio Interface Gap. *J. Phys. Chem. C* **2017**, *121*, 27473–27482.
- (25) Chen, X.; Hua, W.; Huang, Z.; Allen, H. C. Interfacial Water Structure Associated with Phospholipid Membranes Studied by Phase-Sensitive Vibrational Sum Frequency Generation Spectroscopy. *J. Am. Chem. Soc.* **2010**, *132*, 11336–11342.
- (26) Dalchand, N.; Doğangün, M.; Ohno, P. E.; Ma, E.; Martinson, A. B. F.; Geiger, F. M. Perturbation of Hydrogen-Bonding Networks over Supported Lipid Bilayers by Poly(allylamine hydrochloride). *J. Phys. Chem. B* **2019**, *123*, 4251–4257.
- (27) Olenick, L. L.; Chase, H. M.; Fu, L.; Zhang, Y.; McGeachy, A. C.; Dogangun, M.; Walter, S. R.; Wang, H.; Geiger, F. M. Single-component supported lipid bilayers probed using broadband nonlinear optics. *Phys. Chem. Chem. Phys.* **2018**, *20*, 3063–3072.



- (28) Hall, S. A.; Jena, K. C.; Covert, P. A.; Roy, S.; Trudeau, T. G.; Hore, D. K. Molecular-Level Surface Structure from Nonlinear Vibrational Spectroscopy Combined with Simulations. *J. Phys. Chem. B* **2014**, *118*, 5617–5636.
- (29) Eienthal, K. B. Liquid Interfaces Probed by Second-Harmonic and Sum-Frequency Spectroscopy. *Chem. Rev.* **1996**, *96*, 1343–1360.
- (30) Shen, Y. R. Surface Properties Probed by Second-Harmonic and Sum-Frequency Generation. *Nature* **1989**, *337*, 519–525.
- (31) Ohno, P. E.; Saslow, S. A.; Wang, H.; Geiger, F. M.; Eienthal, K. B. Phase referenced nonlinear spectroscopy of the alpha-quartz/water interface. *Nat. Commun.* **2016**, *7*, 13587.
- (32) Gonella, G.; Lütgebaucks, C.; de Beer, A. G. F.; Roke, S. Second Harmonic and Sum-Frequency Generation from Aqueous Interfaces is Modulated by Interference. *J. Phys. Chem. C* **2016**, *120*, 9165–9173.
- (33) Boamah, M. D.; Ohno, P. E.; Geiger, F. M.; Eienthal, K. B. Relative permittivity in the electrical double layer from nonlinear optics. *J. Chem. Phys.* **2018**, *148*, 222808.
- (34) Moberg, D. R.; Straight, S. C.; Paesani, F. Temperature Dependence of the Air/Water Interface Revealed by Polarization Sensitive Sum-Frequency Generation Spectroscopy. *J. Phys. Chem. B* **2018**, *122*, 4356–4365.
- (35) Wen, Y.-C.; Zha, S.; Liu, X.; Yang, S.; Guo, P.; Shi, G.; Fang, H.; Shen, Y. R.; Tian, C. Unveiling Microscopic Structures of Charged Water Interfaces by Surface-Specific Vibrational Spectroscopy. *Phys. Rev. Lett.* **2016**, *116*, 016101.

- (36) Gan, W.; Wu, D.; Zhang, Z.; Feng, R.-r.; Wang, H.-f. Polarization and experimental configuration analyses of sum frequency generation vibrational spectra, structure, and orientational motion of the air/water interface. *J. Chem. Phys.* **2006**, *124*, 114705.
- (37) Lu, R.; Gan, W.; Wu, B.-h.; Chen, H.; Wang, H.-f. Vibrational Polarization Spectroscopy of CH Stretching Modes of the Methylene Group at the Vapor/Liquid Interfaces with Sum Frequency Generation. *J. Phys. Chem. B* **2004**, *108*, 7297–7306.
- (38) Backus, E. H. G.; Garcia-Araez, N.; Bonn, M.; Bakker, H. J. On the Role of Fresnel Factors in Sum-Frequency Generation Spectroscopy of Metal-Water and Metal-Oxide-Water Interfaces. *J. Phys. Chem. C* **2012**, *116*, 23351–23361.
- (39) Wang, H.-f.; Gan, W.; Lu, R.; Rao, Y.; Wu, B.-H. Quantitative spectral and orientational analysis in surface sum frequency generation vibrational spectroscopy (SFG-VS). *Int. Rev. Phys. Chem.* **2005**, *24*, 191–256.
- (40) Bordenyuk, A. N.; Weeraman, C.; Yatawara, A.; Jayathilake, H. D.; Stiopkin, I.; Liu, Y.; Benderskii, A. V. Vibrational Sum Frequency Generation Spectroscopy of Dodecanethiol on Metal Nanoparticles. *J. Phys. Chem. C* **2007**, *111*, 8925–8933.
- (41) Simpson, G. J.; Dailey, C. A.; Plocinik, R. M.; Moad, A. J.; Polizzi, M. A.; Everly, R. M. Direct Determination of Effective Interfacial Optical Constants by Nonlinear Optical Null Ellipsometry of Chiral Films. *Anal. Chem.* **2005**, *77*, 215–224.

- (42) Wang, L.; Nihonyanagi, S.; Inoue, K.-i.; Nishikawa, K.; Morita, A.; Ye, S.; Tahara, T. Effect of Frequency-Dependent Fresnel Factor on the Vibrational Sum Frequency Generation Spectra for Liquid/Solid Interfaces. *J. Phys. Chem. C* **2019**, *123*, 15665–15673.
- (43) Tong, Y.; Zhao, Y.; Li, N.; Osawa, M.; Davies, P. B.; Ye, S. Interference effects in the sum frequency generation spectra of thin organic films. I. Theoretical modeling and simulation. *J. Chem. Phys.* **2010**, *133*, 034704.
- (44) Dai, M.; Wan, W.; Zhu, X.; Song, B.; Liu, X.; Lu, M.; Cui, B.; Chen, Y. Broadband and wide angle infrared wire-grid polarizer. *Opt. Express* **2015**, *23*, 15390–15397.

### References for Chapter 3

- (1) Troiano, J. M. et al. Direct Probes of 4 nm Diameter Gold Nanoparticles Interacting with Supported Lipid Bilayers. *J. Phys. Chem. C* **2014**, *119*, 534–546.
- (2) Silva, T. R.; Brondani, D.; Zapp, E.; Vieira, I. C. Electrochemical Sensor Based on Gold Nanoparticles Stabilized in Poly(Allylamine hydrochloride) for Determination of Vanillin. *Electroanalysis* **2015**, *27*, 465–472.
- (3) Buchman, J. T.; Rahnamoun, A.; Landy, K. M.; Zhang, X.; Vartanian, A. M.; Jacob, L. M.; Murphy, C. J.; Hernandez, R.; Haynes, C. L. Using an environmentally-relevant panel of Gram-negative bacteria to access the toxicity of polyallylamine hydrochloride-wrapped gold nanoparticles. *Environ. Sci. Nano* **2018**, *5*, 279–288.
- (4) Qiu, T. A.; Torelli, M. D.; Vartanian, A. M.; Rackstraw, N. B.; Buchman, J. T.; Jacob, L. M.; Murphy, C. J.; Hamers, R. J.; Haynes, C. L. Quantification of Free Polyelectrolytes Present in Colloidal Suspension, Revealing a Source of Toxic Responses for Polyelectrolyte-Wrapped Gold Nanoparticles. *Anal. Chem.* **2017**, *89*, 1823–1830.
- (5) Olenick, L. L. et al. Lipid Corona Formation from Nanoparticle Interactions with Bilayers. *Chem.* **2018**, *4*, 2709–2723.
- (6) Troiano, J. M.; McGeachy, A. C.; Olenick, L. L.; Fang, D.; Liang, D.; Hong, J.; Kuech, T. R.; Caudill, E. R.; Pedersen, J. A.; Cui, Q.; Geiger, F. M. Quantifying the Electrostatics of Polycation-Lipid Bilayer Interactions. *J. Am. Chem. Soc.* **2017**, *139*, 5808–5816.
- (7) Chan, Y.-H. M.; Boxer, S. G. Model membrane systems and their applications. *Curr. Opin. Chem. Biol.* **2007**, *11*, 581–587.

- (8) Plant, A. L. Supported Hybrid Bilayer Membranes as Rugged Cell Membrane Mimics. *Langmuir* **1999**, *15*, 5128–5135.
- (9) Tanaka, M.; Sackmann, E. Polymer-supported membranes as models of the cell surface. *Nature* **2005**, *437*, 656.
- (10) Bonn, M.; Bakker, H. J.; Tong, Y.; Backus, E. H. No Ice-Like Water at Aqueous Biological Interfaces. *Biointerphases* **2012**, *7*, 20.
- (11) Nagata, Y.; Mukamel, S. Vibrational Sum-Frequency Generation Spectroscopy at the Water/Lipid Interface: Molecular Dynamics Simulation Study. *J. Am. Chem. Soc.* **2010**, *132*, 6434–6442.
- (12) Leroueil, P. R.; Berry, S. A.; Duthie, K.; Han, G.; Rotello, V. M.; McNerny, D. Q.; Jr. Baker, J. R.; Orr, B. G.; Banaszak Holl, M. M. Wide Varieties of Cationic Nanoparticles Induce Defects in Supported Lipid Bilayers. *Nano Lett.* **2008**, *8*, 420–424.
- (13) Brown, K. L.; Conboy, J. C. Electrostatic Induction of Lipid Asymmetry. *J. Am. Chem. Soc.* **2011**, *133*, 8794–8797.
- (14) Dogangun, M.; Hang, M. N.; Machesky, J.; McGeachy, A. C.; Dalchand, N.; Hamers, R. J.; Geiger, F. M. Evidence for Considerable Metal Cation Concentrations from Lithium Intercalation Compounds in the Nano-Bio Interface Gap. *J. Phys. Chem. C* **2017**, *121*, 27473–27482.
- (15) Dogangun, M.; Hang, M. N.; Troiano, J. M.; McGeachy, A. C.; Melby, E. S.; Pedersen, J. A.; Hamers, R. J.; Geiger, F. M. Alteration of Membrane Compositional Asymmetry by LiCoO<sub>2</sub> Nanosheets. *ACS Nano* **2015**, *9*, 8755–8765.

- (16) Stanglmaier, S.; Hertrich, S.; Fritz, K.; Moulin, J.-F.; Haese-Seiller, M.; Radler, J. O.; Nickel, B. Asymmetric Distribution of Anionic Phospholipids in Supported Lipid Bilayers. *Langmuir* **2012**, *28*, 10818–10821.
- (17) Bahrami, A. H.; Raatz, M.; Jaime, A.-C.; Michel, R.; Curtis, E. M.; Hall, C. K.; Gradzielski, M.; Lipowsky, R.; Weigl, T. R. Wrapping of nanoparticles by membranes. *Adv. Colloid Interface Sci.* **2014**, *208*, 214–224.
- (18) Zhang, S.; Gao, H.; Bao, G. Physical Principles of Nanoparticle Cellular Endocytosis. *ACS Nano* **2015**, *9*, 8655–8671.
- (19) Jing, B.; Zhu, Y. Disruption of Supported Lipid Bilayers by Semihydrophobic Nanoparticles. *J. Am. Chem. Soc.* **2011**, *133*, 10983–10989.
- (20) Livingston, R. A.; Zhang, Z.; Piatkowski, L.; Bakker, H. J.; Hunger, J.; Bonn, M.; Backus, E. H. Water in Contact with a Cationic Lipid Exhibits Bulklike Vibrational Dynamics. *J. Phys. Chem. B* **2016**, *120*, 10069–1008.
- (21) Schlaich, A.; Knapp, E. W.; Netz, R. R. Water Dielectric Effects in Planar Confinement. *Physical Review Letters* **2016**, *117*, 048001.
- (22) Richmond, G. L. Molecular bonding and interactions at aqueous surfaces as probed by vibrational sum frequency spectroscopy. *Chem. Rev.* **2002**, *102*, 2693–2724.
- (23) Chen, X.; Hua, W.; Huang, Z.; Allen, H. C. Interfacial Water Structure Associated with Phospholipid Membranes Studied by Phase-Sensitive Vibrational Sum Frequency Generation Spectroscopy. *J. Am. Chem. Soc.* **2010**, *132*, 11336–11342.
- (24) Ishiyama, T.; Terada, D.; Morita, A. Hydrogen-Bonding Structure at Zwitterionic Lipid/Water Interface. *J. Phys. Chem. Lett.* **2016**, *7*, 216–220.

- (25) Mifflin, A. L.; Velarde, L.; Ho, J.; Psciuk, B. T.; Negre, C. F. A.; Ebben, C. J.; Upshur, M. A.; Lu, Z.; Strick, B. L.; Thomson, R. J.; Batista, V. S.; Wang, H.-f.; Geiger, F. M. Accurate Line Shapes from Sub-1  $\text{cm}^{-1}$  Resolution Sum Frequency Generation Vibrational Spectroscopy of  $\alpha$ -Pinene at Room Temperature. *J. Phys. Chem. A* **2015**, *119*, 1292–1302.
- (26) Buchbinder, A. M.; Weitz, E.; Geiger, F. M. Pentane, Hexane, Cyclopentane, Cyclohexane, 1-Hexene, 1-Pentene, cis-2-Pentene, Cyclohexene, and Cyclopentene at Vapor/ $\alpha$ -Alumina and Liquid/ $\alpha$ -Alumina Interfaces Studied by Broadband Sum Frequency Generation. *J. Phys. Chem. C* **2010**, *114*, 554–566.
- (27) Stokes, G. Y.; Chen, E. H.; Buchbinder, A. M.; Paxton, W. F.; Keeley, A.; Geiger, F. M. Atmospheric Heterogeneous Stereochemistry. *J. Am. Chem. Soc.* **2009**, *131*, 13733–13737.
- (28) Ohno, P. E.; Wang, H.; Geiger, F. M. Second-order spectral lineshapes from charged interfaces. *Nat. Commun.* **2017**, *8*, 1032.
- (29) Reddy, S. K.; Thiriaux, R.; Wellen Rudd, B. A.; Lin, L.; Adel, T.; Joutsuka, T.; Geiger, F. M.; Allen, H. C.; Morita, A.; Paesani, F. Bulk Contributions Modulate the Sum-Frequency Generation Spectra of Water on Model Sea-Spray Aerosols. *Chem* **2018**, *4*, 1629–1644.
- (30) Ohno, P. E.; Wang, H. F.; Paesani, F.; Skinner, J. L.; Geiger, F. M. Second-Order Vibrational Lineshapes from the Air/Water Interface. *J. Phys. Chem A* **2018**, *122*, 4457–4464.
- (31) McGeachy, A. C.; Dalchand, N.; Caudill, E. R.; Li, T.; Dogangun, M.; Olenick, L. L.; Chang, H.; Pedersen, J. A.; Geiger, F. M. Interfacial electrostatics of poly(vinylamine

- hydrochloride), poly(diallyldimethylammonium chloride), poly-L-lysine, and poly-L-arginine interacting with lipid bilayers. *Phys. Chem. Chem. Phys.* **2018**, *20*, 10846–10856.
- (32) Fischer, D.; Li, Y.; Ahlemeyer, B.; Kriegelstein, J.; Kissel, T. In vitro cytotoxicity testing of polycations: influence of polymer structure on cell viability and hemolysis. *Biomaterials* **2003**, *24*, 1121–1131.
- (33) Hong, S.; Leroueil, P. R.; Janus, E. K.; Peters, J. L.; Kober, M.-M.; Islam, M. T.; Orr, B. G.; Jr. Baker, J. R.; Banaszak Holl, M. M. Interaction of Polycationic Polymers with Supported Lipid Bilayers and Cells: Nanoscale Hole Formation and Enhanced Membrane Permeability. *Bioconjugate Chem.* **2006**, *17*, 728–734.
- (34) Doğangün, M.; Ohno, P. E.; Liang, D.; McGeachy, A. C.; Bé, A. G.; Dalchand, N.; Li, T.; Cui, Q.; Geiger, F. M. Hydrogen-Bond Networks near Supported Lipid Bilayers from Vibrational Sum Frequency Generation Experiments and Atomistic Simulations. *J. Phys. Chem. B* **2018**, *122*, 4870–4879.
- (35) Olenick, L. L.; Chase, H. M.; Fu, L.; Zhang, Y.; McGeachy, A. C.; Dogangun, M.; Walter, S. R.; Wang, H.; Geiger, F. M. Single-component supported lipid bilayers probed using broadband nonlinear optics. *Phys. Chem. Chem. Phys.* **2018**, *20*, 3063–3072.
- (36) Kalb, E.; Frey, S.; Tamm, L. K. Formation of supported planar bilayers by fusion of vesicles to supported phospholipid monolayers. *Biochim. Biophys. Acta, Biomembr.* **1992**, *1103*, 307–316.
- (37) Castellana, E. T.; Cremer, P. S. Solid supported lipid bilayers: From biophysical studies to sensor design. *Surf. Sci. Rep.* **2006**, *61*, 429–444.



- (38) Woollam, J. A.; Snyder, P. G. Fundamentals and applications of variable angle spectroscopic ellipsometry. *Mat. Sci. Eng., B* **1990**, *5*, 279–283.
- (39) Kreke, M. R.; Badami, A. S.; Brady, J. B.; Akers, R. M.; Goldstein, A. S. Modulation of protein adsorption and cell adhesion by poly(allylamine hydrochloride) heparin films. *Biomaterials* **2005**, *26*, 2975–2981.
- (40) Lvov, Y.; Decher, G.; Mohwald, H. Assembly, Structural Characterization, and Thermal Behavior of Layer-by-Layer Deposited Ultrathin Films of Poly(vinyl sulfate) and Poly(allylamine). *Langmuir* **1993**, *9*, 481–486.
- (41) Decher, G.; Eckle, M.; Schmitt, J.; Struth, B. Layer-by-layer assembled multicomposite films. *Curr. Opin. Colloid Interface Sci.* **1998**, *3*, 32–39.
- (42) Kujawa, P.; Audi-Hayet, A.; Selb, J.; Candau, F. Rheological properties of multisticker associative polyelectrolytes in semidilute solutions. *J. Polym. Sci. B* **2004**, *42*, 1640–1655.
- (43) Jachimska, B.; Jasinski, T.; Warszniski, P.; Adamczyk, Z. Conformations of poly(allylamine hydrochloride) in electrolyte solutions: Experimental measurements and theoretical modeling. *Colloids Surf. A* **2010**, *355*, 7–15.
- (44) Hagen, W.; Tielens, A. G. G. M.; Greenberg, J. M. The infrared spectra of amorphous solid water and ice i, between 10 and 140 k. *Chem. Phys.* **1981**, *56*.
- (45) Lawrence, C.; Skinner, J. L. Ultrafast infrared spectroscopy probes hydrogen-bonding dynamics in liquid water. *Chem. Phys. Lett.* **2003**, *369*, 472–477.
- (46) Shen, Y. R.; Ostroverkhov, V. Sum-Frequency Vibrational Spectroscopy on Water Interfaces: Polar Orientation of Water Molecules at Interfaces. *Chem. Rev.* **2006**, *106*, 1140–1154.

- (47) Gragson, D. E.; Richmond, G. L. Investigations of the structure and hydrogen bonding of water molecules at liquid surfaces by vibrational sum frequency spectroscopy. *J. Phys. Chem. B* **1998**, *102*, 3847–3861.
- (48) Petrache, H. I.; Tristram-Nagle, S.; Gawrisch, K.; Harries, D.; Parsegian, V. A.; Nagle, J. F. Structure and Fluctuations of Charged Phosphatidylserine Bilayers in the Absence of Salt. *Biophys. J.* **2004**, *86*, 1574–1586.
- (49) Mondal, J. A.; Nihonyanagi, S.; Yamaguchi, S.; Tahara, T. Three Distinct Water Structures at a Zwitterionic Lipid/Water Interface Revealed by Heterodyne-Detected Vibrational Sum Frequency Generation. *J. Am. Chem. Soc.* **2012**, *134*, 7842–7850.
- (50) Pandit, S. A.; Berkowitz, M. L. Molecular Dynamics Simulation of Dipalmitoylphosphatidylserine Bilayer with Na<sup>+</sup> Counterions. *Biophys. J.* **2002**, *82*, 1818–1827.
- (51) Bhide, S. Y.; Berkowitz, M. L. Structure and dynamics of water at the interface with phospholipid bilayers. *J. Chem. Phys.* **2005**, *123*, 224702.
- (52) Elmore, D. E. Molecular dynamics simulation of a phosphatidylglycerol membrane. *FEBS Lett.* **2005**, *580*, 144–148.
- (53) Murzyn, K.; Zhao, W.; Karttunen, M.; Kurdziel, M.; Rog, T. Dynamics of water at membrane surfaces: Effect of headgroup structure. *Biointerphases* **2006**, *1*, 98–105.
- (54) Boamah, M. D.; Ohno, P. E.; Geiger, F. M.; Eissenthal, K. B. Relative permittivity in the electrical double layer from nonlinear optics. *J. Chem. Phys.* **2018**, *148*, 222808.

- (55) Ohno, P. E.; Saslow, S. A.; Wang, H.; Geiger, F. M.; Eisenthal, K. B. Phase referenced nonlinear spectroscopy of the alpha-quartz/water interface. *Nat. Commun.* **2016**, *7*, 13587.
- (56) Ohno, P. E.; Chang, H.; Spencer, A. P.; Liu, Y.; Boamah, M. D.; Wang, H.-f.; Geiger, F. M. Beyond the Gouy–Chapman Model with Heterodyne-Detected Second Harmonic Generation. *J. Phys. Chem. Lett.* **2019**, *10*, 2328–2334.
- (57) Cordomi, A.; Edholm, O.; Perez, J. J. Effect of Force Field Parameters on Sodium and Potassium Ion Binding to Dipalmitoyl Phosphatidylcholine Bilayers. *J. Chem. Theory Comput.* **2009**, *5*, 2125–2134.

### References for Chapter 4

- (1) Green, J.-B. D.; Fulghum, T.; Nordhaus, M. A. A Review of Immobilized Antimicrobial Agents and Methods for Testing. *Biointerphases* **2011**, *6*, MR13–MR28.
- (2) Iarikov, D. D.; Kargar, M.; Sahari, A.; Russel, L.; Gause, K. T.; Behkam, B.; Ducker, W. A. Antimicrobial Surfaces Using Covalently Bound Polyallylamine. *Biomacromolecules* **2014**, *15*, 169–176.
- (3) Kügler, R.; Bouloussa, O.; Rondelez, F. Evidence of a Charge-Density Threshold for Optimum Efficiency of Biocidal Cationic Surfaces. *Microbiology* **2005**, *151*, 1341–1348.
- (4) Onaizi, S. A.; Leong, S. S. J. Tethering Antimicrobial Peptides: Current Status and Potential Challenges. *Biotechnol. Adv.* **2011**, *29*, 67–74.
- (5) Modra, K.; Dai, S.; Zhang, H.; Shi, B.; Bi, J. Polycation-Mediated Gene Delivery: Challenges and Considerations for the Process of Plasmid DNA Transfection. *Eng. Life Sci.* **2015**, *15*, 489–498.
- (6) Brown, M. A.; Abbas, Z.; Kleibert, A.; Green, R. G.; Goel, A.; May, S.; Squires, T. M. Determination of Surface Potential and Electrical Double-Layer Structure at the Aqueous Electrolyte-Nanoparticle Interface. *Phys. Rev. X* **2016**, *6*, 011007.
- (7) Brown, M. A.; Bossa, G. V.; May, S. Emergence of a Stern Layer from the Incorporation of Hydration Interactions into the Gouy–Chapman Model of the Electrical Double Layer. *Langmuir* **2015**, *31*, 11477–11483.
- (8) Ahmed, S. M. Studies of the Dissociation of Oxide Surfaces at the Liquid-Solid Interface. *Can. J. Chem.* **1966**, *44*, 1663–1670.

- (9) Abendroth, R. P. Behavior of a Pyrogenic Silica in Simple Electrolytes. *J. Colloid Interface Sci.* **1970**, *34*, 591–596.
- (10) Kitamura, A.; Fujiwara, K.; Yamamoto, T.; Nishikawa, S.; Moriyama, H. Analysis of Adsorption Behavior of Cations onto Quartz Surface by Electrical Double-layer Model. *J. Nucl. Sci. Technol.* **1999**, *36*, 1167–1175.
- (11) Bonthuis, D. J.; Horinek, D.; Bocquet, L.; Netz, R. R. Electrohydraulic Power Conversion in Planar Nanochannels. *Phys. Rev. Lett.* **2009**, *103*, 144503.
- (12) Ermakov, Y. A. Boundary Potential of Lipid Bilayers: Methods, Interpretations and Biological Applications. *IOP Conf. Series: Journal of Physics: Conf. Series* **2017**, *794*, 012007.
- (13) Kandori, K.; Ishiguro, H.; Kno-no, K.; Kitahara, A. Effects of pH and Ionic Surfactants on Ionic Lattices with High Surface Charge Density. *Langmuir* **1989**, *5*, 1258–1261.
- (14) Casper, C. B.; Verreault, D.; Adams, E. M.; Hua, W.; Allen, H. C. Surface Potential of DPPC Monolayers on Concentrated Aqueous Salt Solutions. *Journal of Physical Chemistry B* **2016**, *120*, 2043–2052.
- (15) Boamah, M. D.; Ohno, P. E.; Geiger, F. M.; Eienthal, K. B. Relative permittivity in the electrical double layer from nonlinear optics. *J. Chem. Phys.* **2018**, *148*, 222808.
- (16) Kurosaki, S. The Dielectric Behavior of Sorbed Water on Silica Gel. *J. Phys. Chem.* **1954**, *58*, 320–324.

- (17) Sakamoto, T.; Nakamura, H.; Uedaira, H.; Wada, A. High-Frequency Dielectric Relaxation of Water Bound to Hydrophilic Silica Gels. *J. Phys. Chem.* **1989**, *93*, 357–366.
- (18) Wander, M. C. F.; Clark, A. E. Structural and Dielectric Properties of Quartz-Water Interfaces. *J. Phys. Chem. C* **2008**, *112*, 19986–19994.
- (19) Schlaich, A.; Knapp, E. W.; Netz, R. R. Water Dielectric Effects in Planar Confinement. *Physical Review Letters* **2016**, *117*, 048001.
- (20) Sahai, N.; Sverjensky, D. A. Evaluation of Internally Consistent Parameters for the Triple-Layer Model by the Systematic Analysis of Oxide Surface Titration Data. *Geochim. Cosmochim. Acta* **1997**, *61*, 2801–2826.
- (21) Teschke, O.; Ceotto, G.; de Souza, E. F. Interfacial Water Dielectric-Permittivity-Profile Measurements Using Atomic Force Microscopy. *Phys. Rev. E* **2001**, *64*, 011605.
- (22) Fumagalli, L.; Esfandiar, A.; Fabregas, R.; Hu, S.; Ares, P.; Janardanan, A.; Yang, Q.; Radha, B.; Taniguchi, T.; Watanabe, K.; Gomila, G.; Novoselov, K. S.; Geim, A. K. Anomalously Low Dielectric Constant of Confined Water. *Science* **2018**, *360*, 1339–1342.
- (23) Delgado, A. V.; Gonzalez-Caballero, F.; Hunter, R. J.; Koopal, L. K.; Lyklema, J. Measurement and Interpretation of Electrokinetic Phenomena. *Pure Appl. Chem.* **2005**, *77*, 1753–1805.
- (24) Mattei, M.; Kang, G.; Goubert, G.; Chulhai, D. V.; Schatz, G. C.; Jensen, L.; van Duyne, R. P. Tip-Enhanced Raman Voltammetry: Coverage Dependence and Quantitative Modeling. *Nano Lett.* **2017**, *17*, 590–596.

- (25) Yang, Y.; Mayer, K. M.; Wickremasinghe, N. S.; Hafner, J. H. Probing the Lipid Membrane Dipole Potential by Atomic Force Microscopy. *Biophys. J.* **2008**, *95*, 5193–5199.
- (26) Hapala, P.; Svec, M.; Stetsovych, O.; van der Heijden, N. J.; Ondracek, M.; van der Lit, J.; Mutombo, P.; Swart, I.; Jelinek, P. Mapping the Electrostatic Force Field of Single Molecules from High-Resolution Scanning Probe Images. *Nat. Commun.* **2016**, *7*, 11560.
- (27) Ong, S.; Zhao, X.; Eienthal, K. B. Polarization of Water Molecules at a Charged Interface: Second Harmonic Studies of the Silica/Water Interface. *Chem. Phys. Lett.* **1992**, *191*, 327–335.
- (28) Shen, Y. R. Surface Properties Probed by Second-Harmonic and Sum-Frequency Generation. *Nature* **1989**, *337*, 519–525.
- (29) Ohno, P. E.; Saslow, S. A.; Wang, H.; Geiger, F. M.; Eienthal, K. B. Phase referenced nonlinear spectroscopy of the alpha-quartz/water interface. *Nat. Commun.* **2016**, *7*, 13587.
- (30) Wen, Y.-C.; Zha, S.; Liu, X.; Yang, S.; Guo, P.; Shi, G.; Fang, H.; Shen, Y. R.; Tian, C. Unveiling Microscopic Structures of Charged Water Interfaces by Surface-Specific Vibrational Spectroscopy. *Phys. Rev. Lett.* **2016**, *116*, 016101.
- (31) Gonella, G.; Lütgebaucks, C.; de Beer, A. G. F.; Roke, S. Second Harmonic and Sum-Frequency Generation from Aqueous Interfaces is Modulated by Interference. *J. Phys. Chem. C* **2016**, *120*, 9165–9173.
- (32) Ohno, P. E.; Wang, H.; Geiger, F. M. Second-order spectral lineshapes from charged interfaces. *Nat. Commun.* **2017**, *8*, 1032.

- (33) Chang, H.; Ohno, P. E.; Liu, Y.; Lozier, E. H.; Dalchand, N.; Geiger, F. M. Direct Measurement of Charge Reversal on Lipid Bilayers Using Heterodyne-Detected Second Harmonic Generation Spectroscopy. *J. Phys. Chem. B* **2020**, *124*, 641–649.
- (34) McGeachy, A. C.; Caudill, E. R.; Liang, D.; Cui, Q.; Pedersen, J. A.; Geiger, F. M. Counting Charges on Membrane-Bound Peptides. *Chem. Sci.* **2018**, *9*, 4285–4298.
- (35) Torrens, F.; Castellano, G.; Campos, A.; Abad, C. Negatively Cooperative Binding of Melittin to Neutral Phospholipid Vesicles. *J. Mol. Struct.* **2007**, *834*, 216–228.
- (36) Solomatin, S. V.; Greenfeld, M.; Herschlag, D. Implications of Molecular Heterogeneity for the Cooperativity of Biological Macromolecules. *Nat. Struct. Mol. Biol.* **2011**, *18*, 732–734.
- (37) Mosior, M.; McLaughlin, S. Electrostatics and Reduction of Dimensionality Produce Apparent Cooperativity when Basic Peptides Bind to Acidic Lipids in Membranes. *Biochim. Biophys. Acta* **1992**, *1105*, 185–187.
- (38) Robison, A. D.; Sun, S.; Poyton, M. F.; Johnson, G. A.; Pellois, J. P.; Jungwirth, P.; Vazdar, M.; Cremer, P. S. Polyarginine Interacts More Strongly and Cooperatively than Polylysine with Phospholipid Bilayers. *J. Phys. Chem. B* **2016**, *120*, 9287–9296.
- (39) Kostritskii, A. Y.; Kondinskaia, D. A.; Nesterenko, A. M.; Gurtovenko, A. A. Adsorption of Synthetic Cationic Polymers on Model Phospholipid Membranes: Insight from Atomic-Scale Molecular Dynamics Simulations. *Langmuir* **2016**, *32*, 10402–10414.
- (40) Ishiyama, T.; Morita, A. Computational Analysis of Vibrational Sum Frequency Generation Spectroscopy. *Annu. Rev. Phys. Chem.* **2017**, *68*, 355–377.



- (41) Zhang, L.; Yethiraj, A.; Cui, Q. Free Energy Calculations for the Peripheral Binding of Proteins/Peptides to an Anionic Membrane. 1. Implicit Membrane Models. *J. Chem. Theory Comput.* **2014**, *10*, 2845–2859.
- (42) Donnini, S.; Tegeler, F.; Groenhof, G.; Grubmuller, H. Constant pH Molecular Dynamics in Explicit Solvent with  $\lambda$ -Dynamics. *J. Chem. Theory Comput.* **2011**, *7*, 1962–1978.
- (43) Wallace, J. A.; Shen, J. K. Continuous Constant pH Molecular Dynamics in Explicit Solvent with pH-Based Replica Exchange. *J. Chem. Theory Comput.* **2011**, *7*, 2617–2629.
- (44) Goh, G. B.; Knight, J. L.; III, C. L. B. Constant pH Molecular Dynamics Simulations of Nucleic Acids in Explicit Solvent. *J. Chem. Theory Comput.* **2012**, *8*, 36–46.
- (45) Noid, W. G. Perspective: Coarse-grained Models for Biomolecular Systems. *J. Chem. Phys.* **2013**, *139*, 090901.
- (46) Wu, Z.; Cui, Q.; Yethiraj, A. Why Do Poly-Arg and Poly-Lys Organize Lipids Differently? Insights from Coarse-grained and Atomistic Simulations. *J. Phys. Chem. B* **2013**, *117*, 12145–12156.
- (47) Marrink, S. J.; Tieleman, D. P. Perspective on the Martini Model. *Chem. Soc. Rev.* **2013**, *42*, 6801–6822.
- (48) Barrat, J.-L.; Hansen, J.-P., *Basic Concepts for Simple and Complex Liquids*; Cambridge University Press: Cambridge, UK, 2003.
- (49) Olenick, L. L.; Chase, H. M.; Fu, L.; Zhang, Y.; McGeachy, A. C.; Dogangun, M.; Walter, S. R.; Wang, H.; Geiger, F. M. Single-component supported lipid bilayers

- probed using broadband nonlinear optics. *Phys. Chem. Chem. Phys.* **2018**, *20*, 3063–3072.
- (50) Troiano, J. M.; McGeachy, A. C.; Olenick, L. L.; Fang, D.; Liang, D.; Hong, J.; Kuech, T. R.; Caudill, E. R.; Pedersen, J. A.; Cui, Q.; Geiger, F. M. Quantifying the Electrostatics of Polycation-Lipid Bilayer Interactions. *J. Am. Chem. Soc.* **2017**, *139*, 5808–5816.
- (51) Dalchand, N.; Doğangün, M.; Ohno, P. E.; Ma, E.; Martinson, A. B. F.; Geiger, F. M. Perturbation of Hydrogen-Bonding Networks over Supported Lipid Bilayers by Poly(allylamine hydrochloride). *J. Phys. Chem. B* **2019**, *123*, 4251–4257.
- (52) Doğangün, M.; Ohno, P. E.; Liang, D.; McGeachy, A. C.; Bé, A. G.; Dalchand, N.; Li, T.; Cui, Q.; Geiger, F. M. Hydrogen-Bond Networks near Supported Lipid Bilayers from Vibrational Sum Frequency Generation Experiments and Atomistic Simulations. *J. Phys. Chem. B* **2018**, *122*, 4870–4879.
- (53) Netz, R. R.; Andelman, D. Neutral and Charged Polymers at Interfaces. *Phys. Rep.* **2003**, *380*, 1–95.
- (54) Liu, J.; Conboy, J. C. Structure of a Gel Phase Lipid Bilayer Prepared by the Langmuir–Blodgett/Langmuir–Schaefer Method Characterized by Sum-Frequency Vibrational Spectroscopy. *Langmuir* **2005**, *21*, 9091–9097.
- (55) Brown, K. L.; Conboy, J. C. Electrostatic Induction of Lipid Asymmetry. *J. Am. Chem. Soc.* **2011**, *133*, 8794–8797.
- (56) Dogangun, M.; Hang, M. N.; Machesky, J.; McGeachy, A. C.; Dalchand, N.; Hamers, R. J.; Geiger, F. M. Evidence for Considerable Metal Cation Concentrations from

- Lithium Intercalation Compounds in the Nano-Bio Interface Gap. *J. Phys. Chem. C* **2017**, *121*, 27473–27482.
- (57) Dogangun, M.; Hang, M. N.; Troiano, J. M.; McGeachy, A. C.; Melby, E. S.; Pedersen, J. A.; Hamers, R. J.; Geiger, F. M. Alteration of Membrane Compositional Asymmetry by LiCoO<sub>2</sub> Nanosheets. *ACS Nano* **2015**, *9*, 8755–8765.
- (58) Brown, K. L.; Conboy, J. C. Lipid Flip-Flop in Binary Membranes Composed of Phosphatidylserine and Phosphatidylcholine. *J. Phys. Chem. B* **2013**, *117*, 15041–15050.
- (59) Liu, J.; Conboy, J. C. Direct Measurement of the Transbilayer Movement of Phospholipids by Sum-Frequency Vibrational Spectroscopy. *J. Am. Chem. Soc.* **2004**, *126*, 8376–8377.
- (60) Gragson, D. E.; Richmond, G. L. Investigations of the structure and hydrogen bonding of water molecules at liquid surfaces by vibrational sum frequency spectroscopy. *J. Phys. Chem. B* **1998**, *102*, 3847–3861.
- (61) Mondal, J. A.; Nihonyanagi, S.; Yamaguchi, S.; Tahara, T. Three Distinct Water Structures at a Zwitterionic Lipid/Water Interface Revealed by Heterodyne-Detected Vibrational Sum Frequency Generation. *J. Am. Chem. Soc.* **2012**, *134*, 7842–7850.
- (62) Richmond, G. L. Molecular bonding and interactions at aqueous surfaces as probed by vibrational sum frequency spectroscopy. *Chem. Rev.* **2002**, *102*, 2693–2724.
- (63) Lawrence, C.; Skinner, J. L. Ultrafast infrared spectroscopy probes hydrogen-bonding dynamics in liquid water. *Chem. Phys. Lett.* **2003**, *369*, 472–477.

- (64) McGeachy, A. C.; Dalchand, N.; Caudill, E. R.; Li, T.; Dogangun, M.; Olenick, L. L.; Chang, H.; Pedersen, J. A.; Geiger, F. M. Interfacial electrostatics of poly(vinylamine hydrochloride), poly(diallyldimethylammonium chloride), poly-L-lysine, and poly-L-arginine interacting with lipid bilayers. *Phys. Chem. Chem. Phys.* **2018**, *20*, 10846–10856.
- (65) Ohno, P. E.; Chang, H.; Spencer, A. P.; Liu, Y.; Boamah, M. D.; Wang, H.-f.; Geiger, F. M. Beyond the Gouy–Chapman Model with Heterodyne-Detected Second Harmonic Generation. *J. Phys. Chem. Lett.* **2019**, *10*, 2328–2334.
- (66) Boamah, M. D.; Ohno, P. E.; Lozier, E.; Van Ardenne, J.; Geiger, F. M. Specifics about Specific Ion Adsorption from Heterodyne-Detected Second Harmonic Generation. *arXiv:1905.04148* and *J. Phys. Chem. B* **2019**, *123*.
- (67) Dalstein, L.; Chiang, K.-Y.; Wen, Y.-C. Direct Quantification of Water Surface Charge by Phase-Sensitive Second Harmonic Spectroscopy. *J. Phys. Chem. Lett.* **2019**, *10*.
- (68) Ohno, P. E.; Wang, H.-f.; Paesani, F.; Skinner, J. L.; Geiger, F. M. Second-Order Vibrational Lineshapes from the Air/Water Interface. *J. Phys. Chem. A* **2018**, *122*, 4457–4464.
- (69) Chen, S.-H.; Singer, S. J. Molecular Dynamics Study of the Electric Double Layer and Nonlinear Spectroscopy at the Amorphous Silica-Water Interface. *J. Phys. Chem. B* **2019**, *123*, 6364–6384.
- (70) Wilkosz, N.; Jamróz, D.; Kopeć, W.; Nakai, K.; Yusa, S.-i.; Wyrwal-Sarna, M.; Bednar, J.; Nowakowska, M.; Kepczynski, M. Effect of Polycation Structure on Interaction with Lipid Membranes. *J. Phys. Chem. B* **2017**, *121*, 7318–7326.

- (71) Cui, Q.; Hernandez, R.; Mason, S. E.; Fraunheim, T.; Pedersen, J. A.; Geiger, F. M. Sustainable Nanotechnology: Opportunities and Challenges for Theoretical/Computational Studies. *J. Phys. Chem. B* **2016**, *120*, 7297–7306.
- (72) Bonthuis, D. J.; Gekle, S.; Netz, R. R. Profile of the Static Permittivity Tensor of Water at Interfaces: Consequences for Capacitance, Hydration Interaction and Ion Adsorption. *Langmuir* **2012**, *28*, 7679–7694.
- (73) Bonthuis, D. J.; Netz, R. R. Beyond the Continuum: How Molecular Solvent Structure Affects Electrostatics and Hydrodynamics at Solid-Electrolyte Interfaces. *J. Phys. Chem. B* **2013**, *117*, 11397–11413.
- (74) Su, Z.; Goodall, B.; Leitch, J. J.; Lipkowski, J. Ion transport mechanism in gramicidin A channels formed in floating bilayer lipid membranes supported on gold electrodes. *Electrochim. Acta* **2021**, *375*, 137892.
- (75) Andrew Woolley, G.; Wallace, B. A. Model ion channels: Gramicidin and alamethicin. *J. Membrane Biol.* **1992**, *129*, 109–136.
- (76) Anglin, T. C.; Liu, J.; Conboy, J. C. Facile Lipid Flip-Flop in a Phospholipid Bilayer Induced by Gramicidin A Measured by Sum-Frequency Vibrational Spectroscopy. *Biophys. J.* **2007**, *92*, L01–L03.

### References for Chapter 5

- (1) Bohling, C.; Sigmund, W. Self-Limitation of Native Oxides Explained. *Silicon* **2016**, *8*, 339–343.
- (2) Boamah, M. D.; Isheim, D.; Geiger, F. M. Dendritic Oxide Growth in Zerovalent Iron Nanofilms Revealed by Atom Probe Tomography. *J. Phys. Chem. C* **2018**, *122*, 28225–28232.
- (3) Boamah, M. D.; Lozier, E. H.; Kim, J.; Ohno, P. E.; Walker, C. E.; Miller, T. F.; Geiger, F. M. Energy conversion via metal nanolayers. *Proc. Natl. Acad. Sci.* **2019**, *116*, 16210–16215.
- (4) Dreier, L.; Liu, Z.; Narita, A.; Zadel, M.-J. v.; Mullen, K.; Tielrooij, K.-J.; Backus, E.; Bonn, M. Surface-Specific Spectroscopy of Water at a Potentiostatically Controlled Supported Graphene Monolayer. *J. Phys. Chem. C* **2019**, *123*, 24031–24038.
- (5) Toney, M. F.; Howard, J. N.; Richer, J.; Borges, G. L.; Gordon, J. G.; Melroy, O. R.; Wiesler, D. G.; Yee, D.; Sorensen, L. B. Voltage-dependent ordering of water molecules at an electrode–electrolyte interface. *Nature* **1994**, *368*, 444–446.
- (6) Bouzid, A.; Pasquarello, A. Atomic-Scale Simulation of Electrochemical Processes at Electrode/Water Interfaces under Referenced Bias Potential. *The Journal of Physical Chemistry Letters* **2018**, *9*, 1880–1884.
- (7) Geiger, F. M. Second Harmonic Generation, Sum Frequency Generation, and  $\chi^{(3)}$ : Dissecting Environmental Interfaces with a Nonlinear Optical Swiss Army Knife. *Annu. Rev. Phys. Chem.* **2009**, *60*, 61–83.
- (8) Morita, A., *Theory of Sum Frequency Generation Spectroscopy*; Springer: 2018; Vol. 35.

- (9) Ohno, P. E.; Wang, H.; Geiger, F. M. Second-order spectral lineshapes from charged interfaces. *Nat. Commun.* **2017**, *8*, 1032.
- (10) Doğangün, M.; Ohno, P. E.; Liang, D.; McGeachy, A. C.; Bé, A. G.; Dalchand, N.; Li, T.; Cui, Q.; Geiger, F. M. Hydrogen-Bond Networks near Supported Lipid Bilayers from Vibrational Sum Frequency Generation Experiments and Atomistic Simulations. *J. Phys. Chem. B* **2018**, *122*, 4870–4879.
- (11) Reddy, S. K.; Thiriaux, R.; Wellen Rudd, B. A.; Lin, L.; Adel, T.; Joutsuka, T.; Geiger, F. M.; Allen, H. C.; Morita, A.; Paesani, F. Bulk Contributions Modulate the Sum-Frequency Generation Spectra of Water on Model Sea-Spray Aerosols. *Chem* **2018**, *4*, 1629–1644.
- (12) Boamah, M. D.; Ohno, P. E.; Geiger, F. M.; Eisenthal, K. B. Relative permittivity in the electrical double layer from nonlinear optics. *J. Chem. Phys.* **2018**, *148*, 222808.
- (13) Gonella, G.; Lütgebaucks, C.; de Beer, A. G. F.; Roke, S. Second Harmonic and Sum-Frequency Generation from Aqueous Interfaces is Modulated by Interference. *J. Phys. Chem. C* **2016**, *120*, 9165–9173.
- (14) Marmolejos, J. M.; Bisson, P. J.; Shultz, M. J. Gold as a standard phase reference in complex sum frequency generation measurements. *J. Chem. Phys.* **2019**, *150*, 124705.
- (15) Barbillon, G.; Noblet, T.; Busson, B.; Tadjeddine, A.; Humbert, C. Localised detection of thiophenol with gold nanotriangles highly structured as honeycombs by nonlinear sum frequency generation spectroscopy. *J. Mater. Sci* **2018**, *53*, 4554–4562.

- (16) Lambert, A. G.; Davies, P. B.; Neivandt, D. J. Implementing the Theory of Sum Frequency Generation Vibrational Spectroscopy: A Tutorial Review. *Appl. Spectrosc. Rev.* **2005**, *40*, 103–145.
- (17) Covert, P. A.; Hore, D. K. Assessing the Gold Standard: The Complex Vibrational Nonlinear Susceptibility of Metals. *J. Phys. Chem. C* **2015**, *119*, 271–276.
- (18) Backus, E. H. G.; Garcia-Araez, N.; Bonn, M.; Bakker, H. J. On the Role of Fresnel Factors in Sum-Frequency Generation Spectroscopy of Metal-Water and Metal-Oxide-Water Interfaces. *J. Phys. Chem. C* **2012**, *116*, 23351–23361.
- (19) Tong, Y.; Lapointe, F.; Thamer, M.; Wolf, M.; Campen, R. K. Hydrophobic Water Probed Experimentally at the Gold Electrode/Aqueous Interface. *Angew. Chem. Int. Ed.* **2017**, *56*, 4211–4214.
- (20) Wallentine, S.; Bandaranayake, S.; Biswas, S.; Baker, L. R. Plasmon-Resonant Vibrational Sum Frequency Generation of Electrochemical Interfaces: Direct Observation of Carbon Dioxide Electroreduction on Gold. *J. Phys. Chem A* **2020**, *124*, 8057–8064.
- (21) Dalchand, N.; Doğangün, M.; Ohno, P. E.; Ma, E.; Martinson, A. B. F.; Geiger, F. M. Perturbation of Hydrogen-Bonding Networks over Supported Lipid Bilayers by Poly(allylamine hydrochloride). *J. Phys. Chem. B* **2019**, *123*, 4251–4257.
- (22) Williams, C. T.; Yang, Y.; Bain, C. D. Total Internal Reflection Sum-Frequency Spectroscopy: A Strategy for Studying Molecular Adsorption on Metal Surfaces. *Langmuir* **2000**, *16*, 2343–2350.



- (23) Covington, A. K.; Paabo, M.; Robinson, R. A.; Bates, R. G. Use of the Glass Electrode in Deuterium Oxide and the Relation between the Standardized pD (paD) Scale and the Operational pH in Heavy Water. *Anal. Chem.* **1968**, *40*, 700–706.
- (24) Glasoe, P. K.; Long, F. A. Use of Glass Electrodes to Measure Acidities in Deuterium Oxide. *J. Phys. Chem.* **1960**, *64*, 188–190.
- (25) Hamid, S.; Dillert, R.; Schneider, J.; Bahnemann, D. W. Spectroscopic analysis of proton exchange during the photocatalytic decomposition of aqueous acetic acid: an isotopic study on the product distribution and reaction rate. *Catal. Sci. Technol.* **2018**, *8*, 5886–5899.
- (26) Baldelli, S.; Mailhot, G.; Ross, P. N.; Somorjai, G. A. Potential-Dependent Vibrational Spectroscopy of Solvent Molecules at the Pt(111) Electrode in a Water/Acetonitrile Mixture Studied by Sum Frequency Generation. *J. Am. Chem. Soc.* **2001**, *123*, 7697–7702.
- (27) Dalstein, L.; Revel, A.; Humbert, C.; Busson, B. Nonlinear optical response of a gold surface in the visible range: A study by two-color sum-frequency generation spectroscopy. I. Experimental determination. *J. Chem. Phys.* **2018**, *148*, 134701.
- (28) Gan, W.; Wu, B.-h.; Zhang, Z.; Guo, Y.; Wang, H.-f. Vibrational Spectra and Molecular Orientation with Experimental Configuration Analysis in Surface Sum Frequency Generation (SFG). *J. Phys. Chem. C* **2007**, *111*, 8716–8725.
- (29) Wang, C.-y.; Groenzin, H.; Shultz, M. J. Molecular Species on Nanoparticulate Anatase TiO<sub>2</sub> Film Detected by Sum Frequency Generation: Trace Hydrocarbons and Hydroxyl Groups. *Langmuir* **2003**, *19*, 7330–7334.

- (30) Becraft, K. A.; Moore, F. G.; Richmond, G. L. In-situ spectroscopic investigations of surfactant adsorption and water structure at the  $\text{CaF}_2$ /aqueous solution interface. *Phys. Chem. Chem. Phys.* **2004**, *6*, 1880–1889.
- (31) Covert, P. A.; Jena, K. C.; Hore, D. K. Throwing Salt into the Mix: Altering Interfacial Water Structure by Electrolyte Addition. *J. Phys. Chem. Lett.* **2014**, *5*, 143–148.
- (32) Lawrence, C.; Skinner, J. L. Ultrafast infrared spectroscopy probes hydrogen-bonding dynamics in liquid water. *Chem. Phys. Lett.* **2003**, *369*, 472–477.
- (33) Kim, D.; Kim, E.; Park, S.; Kim, S.; Min, B. K.; Yoon, H. J.; Kwak, K.; Cho, M. Wettability of graphene and interfacial water structure. *Chem* **2021**, *7*, 1602–1614.
- (34) Payne, B. P.; Biesinger, M. C.; McIntyre, N. S. The study of polycrystalline nickel metal oxidation by water vapour. *J. Electron Spectrosc.* **2009**, *175*, 55–65.
- (35) Mahmood, T.; Saddique, M.; Naeem, A.; Mustafa, S.; Dilara, B.; Raza, Z. A. Cation exchange removal of Cd from aqueous solution by NiO. *J. Hazard. Mater.* **2011**, *185*, 824–828.
- (36) Tian, C. S.; Shen, Y. R. Structure and charging of hydrophobic material/water interfaces studied by phase-sensitive sum-frequency vibrational spectroscopy. *Proc. Natl. Acad. Sci.* **2009**, *106*, 15148.

### References for Chapter 6

- (1) Grundmeier, G.; Schmidt, W.; Stratmann, M. Corrosion protection by organic coatings: electrochemical mechanism and novel methods of investigation. *Electrochim. Acta* **2000**, *45*, 2515–2533.
- (2) Khodakarami, S.; Zhao, H.; Rabbi, K. F.; Miljkovic, N. Scalable Corrosion-Resistant Coatings for Thermal Applications. *ACS Appl. Mater. Interfaces* **2021**, *13*, 4519–4534.
- (3) Abdolah Zadeh, M.; van der Zwaag, S.; Garcia, S. J. Adhesion and Long-Term Barrier Restoration of Intrinsic Self-Healing Hybrid Sol–Gel Coatings. *ACS Appl. Mater. Interfaces* **2016**, *8*, 4126–4136.
- (4) Hedberg, J.; Baldelli, S.; Leygraf, C. Evidence for the Molecular Basis of Corrosion of Zinc Induced by Formic Acid using Sum Frequency Generation Spectroscopy. *J. Phys. Chem. Lett.* **2010**, *1*, 1679–1682.
- (5) Brown Jr, G. E.; Henrich, V.; Casey, W.; Clark, D.; Eggleston, C.; Andrew Felmy, A. F.; Goodman, D. W.; Gratzel, M.; Maciel, G.; McCarthy, M. I. Metal oxide surfaces and their interactions with aqueous solutions and microbial organisms. *Chem. Rev.* **1999**, *99*, 77–174.
- (6) Dalstein, L.; Potapova, E.; Tyrode, E. The elusive silica/water interface: Isolated silanols under water as revealed by vibrational sum frequency spectroscopy. *Phys. Chem. Chem. Phys.* **2017**, *19*, 10343–10349.
- (7) Liu, D.; Ma, G.; Xu, M.; Allen, H. C. Adsorption of Ethylene Glycol Vapor on  $\alpha$ - $\text{Al}_2\text{O}_3$  (0001) and Amorphous  $\text{SiO}_2$  Surfaces: Observation of Molecular Orientation

- and Surface Hydroxyl Groups as Sorption Sites. *Environ. Sci. Technol.* **2005**, *39*, 206–212.
- (8) Wang, C.-y.; Groenzin, H.; Shultz, M. J. Molecular Species on Nanoparticulate Anatase TiO<sub>2</sub> Film Detected by Sum Frequency Generation: Trace Hydrocarbons and Hydroxyl Groups. *Langmuir* **2003**, *19*, 7330–7334.
- (9) Braunschweig, B.; Eissner, S.; Daum, W. Molecular Structure of a Mineral/Water Interface: Effects of Surface NanoRoughness of  $\alpha$ -Al<sub>2</sub>O<sub>3</sub> (0001). *J. Phys. Chem. C* **2008**, *112*, 1751–1754.
- (10) Backus, E. H. G.; Garcia-Araez, N.; Bonn, M.; Bakker, H. J. On the Role of Fresnel Factors in Sum-Frequency Generation Spectroscopy of Metal-Water and Metal-Oxide-Water Interfaces. *J. Phys. Chem. C* **2012**, *116*, 23351–23361.
- (11) Williams, C. T.; Yang, Y.; Bain, C. D. Total Internal Reflection Sum-Frequency Spectroscopy: A Strategy for Studying Molecular Adsorption on Metal Surfaces. *Langmuir* **2000**, *16*, 2343–2350.
- (12) Doğangün, M.; Ohno, P. E.; Liang, D.; McGeachy, A. C.; Bé, A. G.; Dalchand, N.; Li, T.; Cui, Q.; Geiger, F. M. Hydrogen-Bond Networks near Supported Lipid Bilayers from Vibrational Sum Frequency Generation Experiments and Atomistic Simulations. *J. Phys. Chem. B* **2018**, *122*, 4870–4879.
- (13) Liu, Y.; Chase, H. M.; Geiger, F. M. Partially (resp. fully) reversible adsorption of monoterpenes (resp. alkanes and cycloalkanes) to fused silica. *J. Chem. Phys.* **2019**, *150*, 074701.
- (14) Chase, H. M.; Ho, J.; Upshur, M. A.; Thomson, R. J.; Batista, V. S.; Geiger, F. M. Unanticipated Stickiness of  $\alpha$ -Pinene. *J. Phys. Chem. A* **2017**, *121*, 3239–3246.

- (15) Kerr, L. T.; Byrne, H. J.; Hennelly, B. M. Optimal choice of sample substrate and laser wavelength for Raman spectroscopic analysis of biological specimen. *Anal. Methods* **2015**, *7*, 5041–5052.
- (16) Dharmaraj, N.; Prabu, P.; Nagarajan, S.; Kim, C. H.; Park, J. H.; Kim, H. Y. Synthesis of nickel oxide nanoparticles using nickel acetate and poly(vinyl acetate) precursor. *Mat. Sci. Eng. B* **2006**, *128*, 111–114.
- (17) Cordoba-Torresi, S. I.; Hugot-Le Goff, A.; Joiret, S. Electrochromic Behavior of Nickel Oxide Electrodes: II . Identification of the Bleached State by Raman Spectroscopy and Nuclear Reactions. *J. Electrochem. Soc.* **1991**, *138*, 1554–1559.
- (18) Geiger, F. M. Second Harmonic Generation, Sum Frequency Generation, and  $\chi^{(3)}$ : Dissecting Environmental Interfaces with a Nonlinear Optical Swiss Army Knife. *Annu. Rev. Phys. Chem.* **2009**, *60*, 61–83.
- (19) Lambert, A. G.; Davies, P. B.; Neivandt, D. J. Implementing the Theory of Sum Frequency Generation Vibrational Spectroscopy: A Tutorial Review. *Appl. Spectrosc. Rev.* **2005**, *40*, 103–145.
- (20) Eisenthal, K. B. Equilibrium and dynamic processes at interfaces by second harmonic and sum frequency generation. *Annu. Rev. Phys. Chem.* **1992**, *43*, 627–661.
- (21) Tsyganenko, A. A.; Filimonov, V. N. Infrared Spectra of Surface Hydroxyl Groups and Crystalline Structure of Oxides. *Spectrosc. Lett.* **1972**, *5*, 477–487.
- (22) Morrow, B.; Ramamurthy, P. Infrared studies of the formation of hydroxyl groups during hydrogen-oxygen reactions on noble metal catalysts. *J. Phys. Chem.* **1973**, *77*, 3052–3058.

- (23) Boamah, M. D.; Lozier, E. H.; Kim, J.; Ohno, P. E.; Walker, C. E.; Miller, T. F.; Geiger, F. M. Energy conversion via metal nanolayers. *Proc. Natl. Acad. Sci.* **2019**, *116*, 16210–16215.
- (24) Su, C.; Puls, R. W. Nitrate Reduction by Zerovalent Iron: Effects of Formate, Oxalate, Citrate, Chloride, Sulfate, Borate, and Phosphate. *Environ. Sci. Technol.* **2004**, *38*, 2715–2720.

## APPENDIX A

**Fresnel Coefficients for a Single Interface**

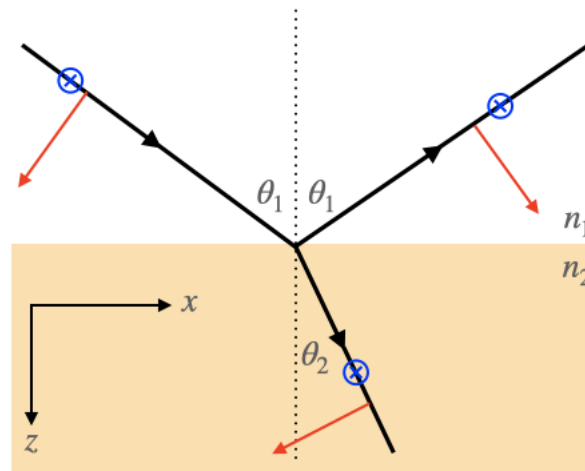
In this appendix, we derive the Fresnel coefficients 2.3.9 – 2.3.11 that describe the reflection and transmission of an incident beam of light off of a single interface. In this section, we follow the discussion of Morita.<sup>1</sup> We assume that the normal to the interface points along the  $z$ -axis and the plane of incidence is the  $xz$ -plane. This situation is shown in Figure A.1 with the adopted right-handed Cartesian coordinate system. In the following derivations, we will make use the electrodynamic boundary conditions

$$(A.0.1) \quad \begin{aligned} E_{1,\parallel} - E_{2,\parallel} &= 0 \\ H_{1,\parallel} - H_{2,\parallel} &= J_{\text{surf}}, \end{aligned}$$

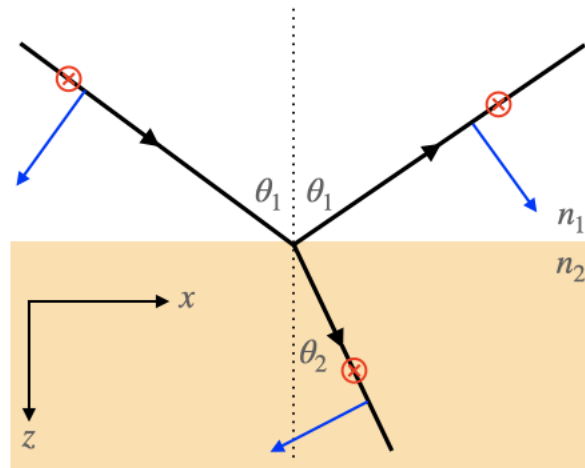
where  $J_{\text{surf}}$  is the surface current density running across the interface and  $E_{1(2),\parallel}$  and  $H_{1(2),\parallel}$  denotes the parallel, meaning the  $x$ - or  $y$ -, component of the electric or magnetic field in medium 1(2), respectively. For perfect dielectrics,  $J_{\text{surf}} = 0$ , and so we will only enforce continuity of the parallel field components of  $\mathbf{E}$  and  $\mathbf{H}$  across the interface. We will also need the relationship between the  $\mathbf{E}$  and  $\mathbf{H}$  fields within a particular medium. From Maxwell's equations, it can be derived that  $E = \sqrt{\frac{\epsilon}{\mu}}H$  and  $n = \sqrt{\epsilon\mu}$ , where  $\epsilon = \epsilon_r\epsilon_0$  is the dielectric permittivity,  $\mu = \mu_r\mu_0$  is the magnetic permeability, and  $n$  is the index of refraction. Using these relations, we have that  $H = \frac{n}{\mu}E$ . We will typically assume that  $\mu$  is the same for both materials so that  $H = nE$ . Furthermore, to rationalize the indicated

direction of the  $\mathbf{H}$  or  $\mathbf{E}$  fields in the diagrams shown in Figure A.1, one should recall that the direction of a travelling beam of light is given by the Poynting vector,  $\mathbf{S} = \mathbf{E} \times \mathbf{H}$ . Practically speaking, the direction of either the  $\mathbf{E}$  or  $\mathbf{H}$  field will be fixed by choosing either an  $s$ - or  $p$ -polarization of light. Thus, the direction of the remaining field should be chosen such that the direction of  $\mathbf{E} \times \mathbf{H}$  coincides with the direction of propagation for the beam of interest (e.g. incident, reflected, or transmitted).





(a) Diagram of light reflection and transmission off an interface for  $s$ -polarized light. Note that the  $\mathbf{H}$  field lies in the plane of incidence while the  $\mathbf{E}$  field is perpendicular.



(b) Diagram of light reflection and transmission off an interface for  $p$ -polarized light. Note that the  $\mathbf{E}$  field lies in the plane of incidence while the  $\mathbf{H}$  field is perpendicular.

Figure A.1. Diagrams showing the geometries of light scattering off of an interface for (a)  $s$ - and (b)  $p$ -polarized light. In both diagrams, the blue represents the electric field and the red denotes the magnetic field. The cross-hatched circle represents a field vector pointing into the page in the  $-y$ -direction.

### A.1. Fresnel coefficients for *s*-polarization

For *s*-polarized light (transverse electric, or TE mode), the electric field will point perpendicular to the *xz*-plane and the magnetic field will point be perpendicular to the direction of propagation and lie within the *xz*-plane, as shown in Figure A.1a. Therefore, the incident beam of light has the following field components:

$$(A.1.1) \quad \mathbf{E}_{\text{inc}}^s = -E_I \hat{\mathbf{y}}$$

$$(A.1.2) \quad \mathbf{H}_{\text{inc}}^s = -H_I \cos \theta_1 \hat{\mathbf{x}} + H_I \sin \theta_1 \hat{\mathbf{z}}.$$

Meanwhile, the reflected beam is described by the fields

$$(A.1.3) \quad \mathbf{E}_{\text{ref}}^s = -E_R \hat{\mathbf{y}}$$

$$(A.1.4) \quad \mathbf{H}_{\text{ref}}^s = H_R \cos \theta_1 \hat{\mathbf{x}} + H_R \sin \theta_1 \hat{\mathbf{z}}$$

and the transmitted beam is characterized by the fields

$$(A.1.5) \quad \mathbf{E}_{\text{trans}}^s = -E_T \hat{\mathbf{y}}$$

$$(A.1.6) \quad \mathbf{H}_{\text{trans}}^s = -H_T \cos \theta_2 \hat{\mathbf{x}} + H_T \sin \theta_2 \hat{\mathbf{z}}$$

Using the electrodynamic boundary conditions, we enforce continuity of the parallel, meaning the *x*- or *y*-, components of each field across the interface. Therefore, we have

the following two equations

$$(A.1.7) \quad E_I + E_R = E_T$$

$$(A.1.8) \quad -H_I \cos \theta_1 + H_R \cos \theta_1 = -H_T \cos \theta_2.$$

Using the fact that  $H = nE$ , the magnetic field continuity condition can be rewritten as

$$(A.1.9) \quad -n_1 E_I \cos \theta_1 + n_1 E_R \cos \theta_1 = -n_2 E_T \cos \theta_2.$$

To solve for the reflected field amplitude,  $E_R$ , one can proceed by inserting equation A.1.7 into equation A.1.9 to obtain the Fresnel reflection coefficient,

$$(A.1.10) \quad \begin{aligned} -n_1 E_I \cos \theta_1 + n_1 E_R \cos \theta_1 &= -n_2 E_I \cos \theta_2 - n_2 E_R \cos \theta_2 \\ (n_1 \cos \theta_1 + n_2 \cos \theta_2) E_R &= (n_1 \cos \theta_1 - n_2 \cos \theta_2) E_I \\ r_{12}^s = \frac{E_R}{E_I} &= \frac{n_1 \cos \theta_1 - n_2 \cos \theta_2}{n_1 \cos \theta_1 + n_2 \cos \theta_2}. \end{aligned}$$

A similar calculation for the Fresnel transmission coefficient follows from substituting  $E_R = E_T - E_I$ , obtained from equation A.1.7, into A.1.9. This results in

$$(A.1.11) \quad \begin{aligned} -n_1 E_I \cos \theta_1 + n_1 E_T \cos \theta_1 - n_1 E_I \cos \theta_1 &= -n_2 E_T \cos \theta_2 \\ (n_1 \cos \theta_1 + n_2 \cos \theta_2) E_T &= 2n_1 \cos \theta_1 E_I \\ t_{12}^s = \frac{E_T}{E_I} &= \frac{2n_1 \cos \theta_1}{n_1 \cos \theta_1 + n_2 \cos \theta_2}. \end{aligned}$$

## A.2. Fresnel coefficients for $p$ -polarization

For  $p$ -polarized light (transverse magnetic, or TM mode), the magnetic field will point perpendicular to the  $xz$ -plane and the electric field will be perpendicular to the direction of propagation and lie within the  $xz$ -plane, as indicated in Figure A.1b. In fact, by comparing the diagrams in Figure A.1, it is clear that the Figure A.1b simply exchanges the roles of the  $\mathbf{E}$  and  $\mathbf{H}$  fields relative to Figure A.1a. Therefore, the vector components of  $\mathbf{E}^p$  have the same form as those for  $\mathbf{H}^s$  and, similarly, the components of  $\mathbf{H}^p$  adopt the same structure as those of  $\mathbf{E}^s$ . Therefore, we may write that the incident beam is

$$(A.2.1) \quad \mathbf{E}_{\text{inc}}^p = -E_I \cos \theta_1 \hat{\mathbf{x}} + E_I \sin \theta_1 \hat{\mathbf{z}}$$

$$(A.2.2) \quad \mathbf{H}_{\text{inc}}^p = -H_I \hat{\mathbf{y}},$$

the reflected beam is

$$(A.2.3) \quad \mathbf{E}_{\text{ref}}^p = E_R \cos \theta_1 \hat{\mathbf{x}} + E_R \sin \theta_1 \hat{\mathbf{z}}$$

$$(A.2.4) \quad \mathbf{H}_{\text{ref}}^p = -H_R \hat{\mathbf{y}},$$

and the transmitted beam is

$$(A.2.5) \quad \mathbf{E}_{\text{trans}}^p = -E_T \cos \theta_2 \hat{\mathbf{x}} + E_T \sin \theta_2 \hat{\mathbf{z}}$$

$$(A.2.6) \quad \mathbf{H}_{\text{trans}}^p = -H_T \hat{\mathbf{y}}.$$

Again, imposing continuity of the parallel components of the fields across the interface results in

$$(A.2.7) \quad -E_I \cos \theta_1 + E_R \cos \theta_1 = -E_T \cos \theta_2.$$

$$(A.2.8) \quad H_I + H_R = H_T$$

and imposing  $H = nE$  changes equation A.2.8 into

$$(A.2.9) \quad n_1 E_I + n_1 E_R = n_2 E_T.$$

To solve for the Fresnel reflection coefficient, insert A.2.9 into A.2.7 and solve for  $E_R$  in terms of  $E_I$  to obtain

$$(A.2.10) \quad \begin{aligned} -E_I \cos \theta_1 + E_R \cos \theta_1 &= -\frac{n_1}{n_2} E_I \cos \theta_2 - \frac{n_1}{n_2} E_R \cos \theta_2 \\ E_R(n_2 \cos \theta_1 + n_2 \cos \theta_2) &= E_I(n_2 \cos \theta_1 - n_1 \cos \theta_2) \\ r_{12}^p = \frac{E_R}{E_I} &= \frac{n_2 \cos \theta_1 - n_1 \cos \theta_2}{n_2 \cos \theta_1 + n_1 \cos \theta_2}. \end{aligned}$$

To solve for the Fresnel transmission coefficient, insert substitute  $n_1 E_R = n_2 E_T - n_1 E_I$  from A.2.9 into A.2.7 to obtain

$$(A.2.11) \quad \begin{aligned} -E_I \cos \theta_1 + \left( \frac{n_2}{n_1} E_T - E_I \right) \cos \theta_1 &= -E_T \cos \theta_2 \\ 2n_1 \cos \theta_1 E_I &= (n_1 \cos \theta_2 + n_2 \cos \theta_1) E_T \\ t_{12}^p = \frac{E_T}{E_I} &= \frac{2n_1 \cos \theta_1}{n_2 \cos \theta_1 + n_1 \cos \theta_2}. \end{aligned}$$

### A.3. Fresnel Local Field Factors

In the context of spectroscopy, we want not just the Fresnel coefficients,  $t_{12}$  and  $r_{12}$ , but we are interested in the transformation that maps the electric field in one medium to the field in another. In particular, we want to find the linear transformation  $\mathbf{L}$  such that such that the field in medium  $j$ ,  $\mathbf{E}^{(j)}$  is related to the field in medium  $i$ ,  $\mathbf{E}^{(i)}$  in the following form

$$(A.3.1) \quad \begin{bmatrix} E_x^{(j)} \\ E_y^{(j)} \\ E_z^{(j)} \end{bmatrix} = \begin{bmatrix} L_{xx} & L_{xy} & L_{xz} \\ L_{yx} & L_{yy} & L_{yz} \\ L_{zx} & L_{zy} & L_{zz} \end{bmatrix} \begin{bmatrix} E_x^{(i)} \\ E_y^{(i)} \\ E_z^{(i)} \end{bmatrix}$$

where the matrix  $\mathbf{L}$  is a symmetric (and typically diagonal) matrix. We can find the form of the local field factors for the single interface system studied above. In particular, the only field in medium 2 is the transmitted field, defined for  $s$ -polarization in Equation A.1.5 and for  $p$ -polarization in Equation A.2.5. The corresponding incident fields are given by Equations A.1.1 and A.2.1 for  $s$ - and  $p$ -polarization, respectively. Thus, for  $s$ -polarization, Equation A.3.1 reduces to a single equation for the only non-zero field component in the  $y$ -direction

$$(A.3.2) \quad E_T = L_{yy}^s E_I,$$

where

$$(A.3.3) \quad L_{yy}^s = t_{12}^s$$

from definition of  $t_{12}^s$  in Equation A.1.12. The situation is less trivial for  $p$ -polarization. In this case, we have two non-zero field components,  $x$  and  $z$ , related through Equation A.3.1 as

$$(A.3.4) \quad \begin{bmatrix} -E_T \cos \theta_2 \\ E_T \sin \theta_2 \end{bmatrix} = \begin{bmatrix} L_{xx}^p & L_{xz}^p \\ L_{zx}^p & L_{zz}^p \end{bmatrix} \begin{bmatrix} -E_I \cos \theta_1 \\ E_I \sin \theta_1 \end{bmatrix}.$$

We can see that  $L_{xz}^p = L_{zx}^p = 0$  and the individual  $L_{xx}^p$  and  $L_{zz}^p$  are found, using the fact that  $E_T = t_{12}^p E_I$  from Equation A.2.12, as

$$(A.3.5) \quad L_{xx}^p = t_{12}^p \frac{\cos \theta_2}{\cos \theta_1}$$

$$(A.3.6) \quad L_{zz}^p = t_{12}^p \frac{\sin \theta_2}{\sin \theta_1} = t_{12}^p \frac{n_1}{n_2},$$

where in the last equality of A.3.6 we have used Snell's law  $n_1 \sin \theta_1 = n_2 \sin \theta_2$ .

## APPENDIX B

**Original Research Proposal****Abstract**

In the presence of Zn (II) and albumin, C-peptide, a 31-amino acid polypeptide secreted alongside insulin, has shown to stimulate the release of ATP by erythrocytes. ATP can then increase NO production, acting indirectly as a vasodilator. This is one of the main therapeutic properties of C-peptide in alleviating diabetes-related complications. Although recent work has highlighted the importance of all three components in the increased release of ATP, little is known about the mechanism of binding of Zn (II) and C-peptide to albumin and any subsequent changes binding has on both protein secondary structure and ATP production. To this end, we propose an approach that couples X-ray crystallography and site-directed mutagenesis to first understand the site(s) at which C-peptide and Zn (II) bind to albumin (human serum albumin, HSA) and to mutate those site (s) to determine which are crucial to inducing changes to protein secondary structure upon binding. Changes to HSA secondary structure are assessed by fluorescence spectroscopy and circular dichroism (CD). The wild-type (WT) and mutant HSA can then be incubated with erythrocytes in a buffer solution containing both Zn (II) and C-peptide to determine which mutation results in the greatest release of ATP. These results can then be compared to the degree of secondary structure change (i.e., more/less  $\alpha$ -helical character than the WT) to determine whether there is a strong correlation between ATP released and secondary structure. Finally, the local solvation environment for the domain



that has the most binding sites, or the most crucial binding site(s) is studied using a combined approach of 2D-IR and molecular dynamics simulations. This approach will be used to complement both fluorescence and CD results.

### B.1. Introduction, Background, and Significance of Research

Diabetes mellitus is a disease that affects the body's ability to maintain normal blood glucose levels. It is primarily due to the inability of the pancreas to produce insulin (type 1 diabetes) or the body's inability to efficiently use insulin (type 2 diabetes).<sup>1,2</sup> Long-term complications can include poor circulation and increased risk of cardiovascular disease as well as nerve impairment and retinopathy.<sup>3-5</sup> To mitigate the likelihood of developing these potential complications, the administration of C-peptide has been considered.<sup>6-8</sup> C-peptide is produced and secreted alongside insulin by the pancreatic  $\beta$ -cells and is often used as a biomarker for insulin as it is secreted in equimolar concentrations in the body.<sup>9,10</sup>

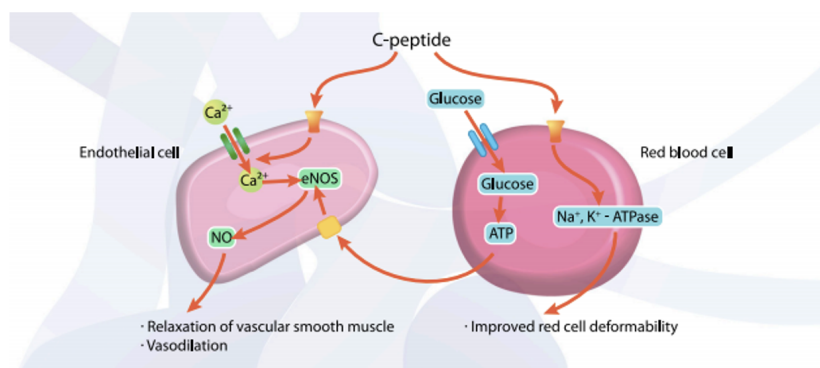


Figure B.1. **The effects of C-peptide on circulation.** C-peptide can increase eNOS activity and therefore, increase the production of NO by stimulating  $Ca^{2+}$  uptake by endothelial cells (cells that line the blood vessels). In erythrocytes, C-peptide can also increase glucose uptake, resulting in increased ATP production and therefore, also increase the production of NO. Lastly, C-peptide has been shown to stimulate  $Na^+$ ,  $K^+$ -ATPase activity.<sup>8</sup>

Experimental and clinical evidence has suggested the therapeutic properties of C-peptide are due to its role in several biochemical pathways.<sup>2,11,12</sup> For example, experiments on animal models have shown that endoneurial blood flow is improved when C-peptide is administered. This is likely due to the stimulation of endothelial nitric oxide synthase (eNOS).<sup>8,13</sup> The eNOS releases nitric oxide (NO) into the blood which is a vasodilator. In erythrocytes, C-peptide increases glucose uptake and the subsequent release of ATP. Both processes are shown in Figure B.1. ATP release by erythrocytes stimulates NO production which is necessary for a healthy response to low oxygen tension as this release can indirectly act as a vasodilator, increasing blood circulation at optimal levels.<sup>14</sup>

Although the evidence presented above shows great potential for the use of C-peptide in replacement therapy, it is currently still not being used. One major reason is that the biological and therapeutic effects of C-peptide are likely not due to C-peptide alone. Recent work has highlighted the importance of both albumin and Zn (II) in C-peptide's biological activity.<sup>15</sup> One study, in particular, showed that ATP release was not enhanced for a system that contained both C-peptide and albumin unless they were in the presence of Zn (II).<sup>16</sup> An understanding of this three-component system is, therefore, essential to understanding the mechanism underlying the therapeutic properties of C-peptide. To begin investigating this mechanism, this study aims to determine the binding site(s) of C-peptide to Human Serum Albumin (HSA) and assess the differences in binding sites (if any) when Zn (II) is also present. From the elucidated binding sites, HSA will then be mutated to determine whether specific binding sites are crucial to ATP production. Changes to secondary structure due to the mutations is also assessed and compared to ATP production as secondary structure is vital to protein function.

Fundamental studies such as these are necessary in order to drive clinical research. It allows for the freedom of optimizing a simplified experimental design before it is tested in a more complex system. If differences between the experimental and clinical trials then occur, there can be a return to basic science to further explore what key elements were missing in the experimental design. This would ultimately provide physicians with the knowledge they need to assess whether or not a certain treatment would benefit their patient.

## **B.2. Scientific Objectives**

The specific aims of this work are as follows: (1) to determine of the binding site(s) of C-peptide to albumin and assess how/if those binding site(s) change in the presence of Zn (II) (2) to assess the relationship between ATP production and secondary structure through the synthesis of albumin mutants and (3) to understand the dynamic changes to the local solvent environment of azidohomoalanine-labeled albumin in the presence of C-peptide, Zn (II), and C-peptide- Zn (II) to complement conformational changes revealed in (2).

## **B.3. Previous Work**

In the literature, the importance of all three components (C-peptide, Zn (II), and albumin) in increasing ATP released by erythrocytes is well-documented.<sup>16,17</sup> By using 3D-printed microfluidics, Liu et. al determined the amount of ATP released when erythrocytes were incubated with solely HSA was  $194.9 \pm 19.7$  nM. There was a significant increase in ATP released in the presence of C-peptide, Zn (II), and albumin ( $319.8 \pm 15.2$  nM). In an albumin-free system, an increase in ATP could not be detected, even in the presence

of both C-peptide and Zn (II). Using isothermal titration calorimetry (ITC) this study also confirmed that human serum albumin (HSA) can bind both C-peptide and Zn (II) with binding constants of  $5.08 \pm 0.98 \times 10^7 \text{ M}^{-1}$  for Zn (II) and  $2.66 \pm 0.25 \times 10^5 \text{ M}^{-1}$  for C-peptide.<sup>16</sup>

Fundamental studies assessing Zn (II) binding to C-peptide have also been done.<sup>14,18</sup> C-peptide contains 31 amino acid residues. Of those amino acids, there are five negatively charged residues; these residues are highlighted in Figure B.2. In the work of Keltner et. al, the acidic residues were mutated with alanine (A; uncharged) to assess whether a single acidic residue was crucial to Zn (II) binding and subsequent ATP production.<sup>18</sup> The mutants assessed were E1A, E3A, D4A, E11A, and E27A. CID-MS/MS determined that the single point mutations did not change fragmentation behavior when compared to the WT peptide. Furthermore, ESI-MS showed that the replacement of any of the acidic residues decreases the binding of Zn (II) by 50% when compared to the WT. Furthermore, there was 50% decrease of ATP released by the mutants when compared to the WT peptide. The E27A mutant showed the greatest decrease in ATP (75%) when compared to the WT. This suggests that E27 is a critical residue for Zn (II) binding to C-peptide. As mentioned, recent work has shown that the presence of Zn (II), C-peptide, and albumin is necessary for ATP release. Although this study does not assess the relevance of albumin to Zn (II) binding, they mention their erythrocyte samples were prepared in a physiological salt solution (PSS) that contained bovine serum albumin (BSA). Therefore, it is likely that albumin also played a role in the release of ATP in this study.

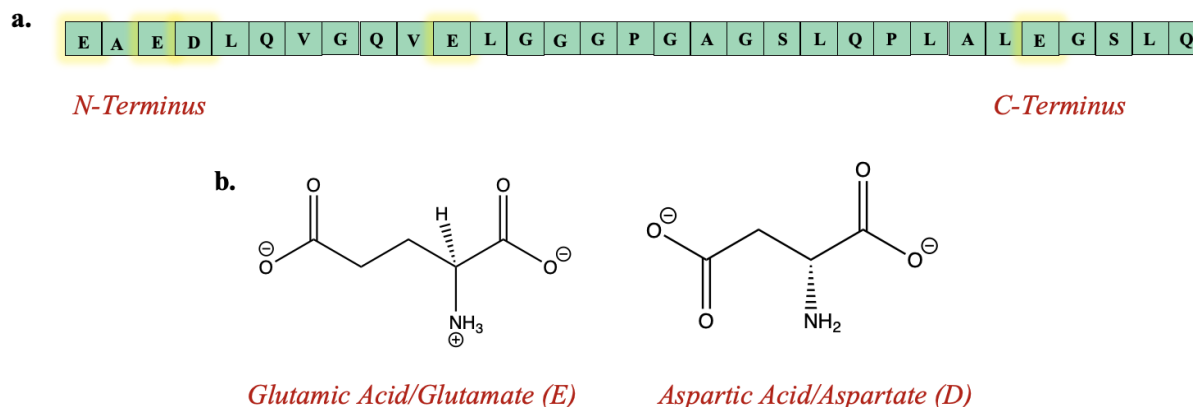


Figure B.2. **Peptide structure.** The primary structure of C-peptide is shown in (a), where the acidic residues E1, E3, D4, E11, and E27 are highlighted in yellow. The structure of E and D amino acids are presented in (b).

## B.4. Proposed Research

### B.4.1. X-ray crystallography

To begin the determination of binding sites of C-peptide and Zn (II) to human serum albumin (HSA), X-ray crystallography would be used. There are two main methods of preparing the crystals: co-crystallization and soaking.<sup>19</sup> The former method is advantageous because the protein would be exposed to the peptide before crystallization. Soaking requires the protein crystal to be immersed in a solution ( $\sim 0.1 - 1$  mM) of the ligand. Because the protein is already crystallized, it may be restricted to any conformational changes with the addition of the ligand. In the case of obtaining crystals from metal-based drugs and proteins, co-crystallization has failed. In these cases, soaking was then used. Therefore, although I would attempt co-crystallization for the system I am interested in, if it is unsuccessful, the soaking method will be used. I would start by determining binding

of solely C-peptide to HSA and then progress to adding Zn (II) to the ligand solution (in the case of soaking).

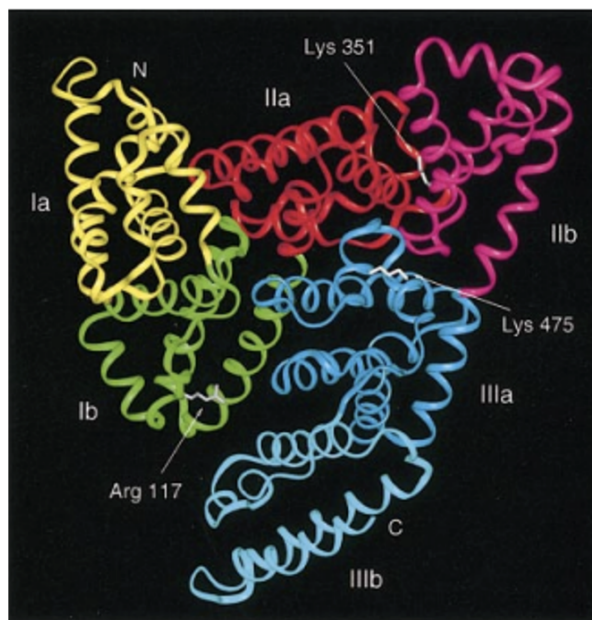


Figure B.3. **Detailed schematic of the HSA protein.** The 6 subdomains are shown above in different colors: Ia (yellow), Ib (green), IIa (red), IIb (pink), IIIa (blue), and IIIb (cyan).<sup>20</sup>

HSA has 585 amino acid residues with three domains (I, II, and III) that are further divided into “A” and “B” subdomains as Figure B.3 shows. There are three main subdomains that small molecules, drugs, dyes, and natural substances have been found to bind in HSA. This includes subdomains IIA and IIIA (Sudlow’s sites) as well as subdomain IB.<sup>21</sup> At subdomains IIA and IIIA, molecules with a peripheral negative charge often bind, with bulky compounds associated with subdomain IIA and smaller ligands associated with subdomain IIIA. Therefore, because C-peptide possesses an overall negative charge, I believe that it may bind to one or multiple of the subdomains mentioned above. The addition of Zn (II) may change this, depending on how strongly Zn (II) interacts with

the negatively charged residues of C-peptide. Furthermore, there can be multiple binding sites on HSA associated with the binding of C-peptide and Zn (II) as is the case for cisplatin binding to HSA. X-ray crystallography (soaking) revealed the binding of cisplatin to amino acid residues in subdomains IA, IIA, IIB, and IIIB.<sup>22</sup>

#### **B.4.2. Site-Directed Mutagenesis (SDM) and Expression of HSA Variants**

Depending on which amino acids were involved in C-peptide-Zn (II) binding, point mutations (single amino acid replacement) on the HSA protein would be made to assess whether a specific site was more crucial than another in (1) stabilizing protein structure and conformation and (2) increasing ATP released by erythrocytes. Moreover, trends between protein structure and ATP release can then be analyzed. Using site-directed mutagenesis (SDM), a plasmid would be generated to express the mutant protein in *P. pastoris*. The recombinant protein would then be isolated and purified by methods shown by Siemiarczuk et al.<sup>23</sup>

#### **B.4.3. Tryptophan fluorescence quenching (fluorescence spectroscopy)**

There is one tryptophan residue in HSA. This residue is present at the 214<sup>th</sup> position in subdomain IIA (one of Sudlow's sites).<sup>24</sup> When HSA is excited with 295 nm light, there is a strong fluorescence emission at 351 nm due to this tryptophan residue.<sup>25</sup> Thus, perturbations to the tryptophan environment signified by changes in fluorescence would indicate changes in protein secondary structure, substrate binding, or denaturation. Small molecules such as monoacylglycerol have been shown to primarily bind at HSA domain II, causing decreases in observed fluorescence and subsequent protein conformational changes

when using this technique. The binding of oleic acid to HSA was also assessed. Here, there was no changes to fluorescence, suggesting oleic acid binds at a different site than monoacylglycerol in the HSA protein.<sup>26</sup> Using this technique, we can confirm binding of C-peptide to HSA in domain II (if binding exists) to further corroborate data from X-ray crystallography. The fluorescence of HSA alone can be taken, then it can then be taken with various concentrations of Zn (II), C-peptide, and a combination of both. The quenching constant ( $k_q$ ,  $M^{-1}s^{-1}$ ) can then be calculated from the Stern-Volmer quenching equation to determine how the binding affinity of Zn (II), C-peptide, and C-peptide-Zn (II) compares. The equation is as follows:<sup>27-29</sup>

$$(B.4.1) \quad \frac{I_0}{I} = 1 + k_q\tau_0[Q] = 1 + K_{SV}[Q]$$

Here,  $\frac{I_0}{I}$  are the fluorescence intensities of HSA in the absence and presence of the ligand,  $[Q]$  is the ligand concentration,  $k_q$  is the quenching rate constant,  $K_{SV}$  is the Stern-Volmer quenching constant and  $\tau_0$  is the average lifetime of the molecule without the ligand. The experiments mentioned above can then be done for the specific point mutations made in domain II. This would assess whether there is one binding site that is preferred over another in the binding of C-peptide and Zn (II). These experiments would also allow us to determine whether a conformational change occurs upon C-peptide binding to HSA. Circular dichroism (CD) can then assess, in more detail, the nature of the conformational change.



#### B.4.4. Circular Dichroism (CD)

As a complement to fluorescence spectroscopy, circular dichroism (CD) can be used. The secondary structure of free HSA has been shown to be dominated by  $\alpha$ -helices.<sup>30</sup> The CD spectra in Figure fig:A1.4 shows the binding of kaempferol with HSA. HSA (without kaempferol) is shown by the first spectrum. There are two negative bands at 209 and 222 nm that are representative of  $\alpha$ -helical character. From here, the mean residue ellipticity (MRE) can be determined:<sup>29</sup>

$$(B.4.2) \quad MRE = \frac{\theta}{10rl[HSA]}$$

Here,  $\theta$  is the CD that is observed,  $l$  is the path length of the cell, and  $r$  is the number of HSA residues (585). From the MRE, we can then determine the %  $\alpha$ -helical character. At 209 nm, this is given by:<sup>29,31</sup>

$$(B.4.3) \quad \% \text{ - helix} = \frac{-MRE_{209\text{nm}} - 4000}{33000 - 4000} \times 1000$$

This relationship would allow for quantitative determination of how the  $\alpha$ -helical character changes based on C-peptide binding (in the presence of Zn (II)) to WT HSA and the mutants. From these results, %  $\alpha$ -helix can be compared for binding on the WT and mutants to determine if the removal of a specific site prohibits conformational change or allows the same conformational change, deeming binding at another site more vital to protein secondary structure. The %  $\alpha$ -helical character can then be compared to the ATP released to determine whether this conformational change is necessary for ATP release to occur.

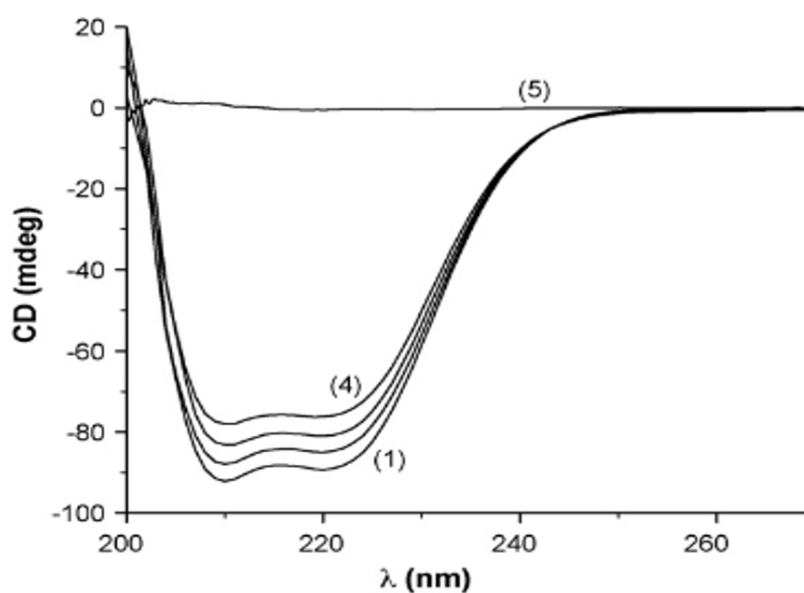


Figure B.4. CD spectra of (1) HSA ( $0.75 \times 10^{-6}$  M) (2) kaempferol-HSA with a drug/protein (d/p) ratio of 1 (3) d/p ratio of 3 (4) d/p ratio of 6 and (5) kaempferol ( $3.3 \times 10^{-6}$  M). These experiments were conducted at a pH of 7.4.<sup>31</sup>

## B.5. ATP Quantification

### B.5.1. Luciferase Assay

Erythrocytes would be prepared and incubated with WT or mutant HSA. Three different incubations would be made: Zn (II) only, C-peptide only, and C-peptide-Zn (II) for each HSA protein tested. ATP released would be determined using a luciferase assay and chemiluminescence measurement by a photomultiplier tube. In the presence of D-luciferin, ATP, O<sub>2</sub>, and magnesium, the enzyme luciferase can catalyze the oxidation of luciferin to emit light which is proportional to the amount of ATP released.<sup>32,33</sup>

The release of ATP is expected to be the highest with an incubation of C-peptide-Zn (II). Differences in ATP production of the mutant's vs. WT HSA proteins can then be compared. Some focuses would be:

- (1) Does HSA with the highest  $\alpha$ -helical character produce the most ATP?
- (2) Is there a specific amino acid mutation that is detrimental to ATP production regardless of secondary structure?
- (3) Does binding affinity (detailed by the binding constant obtained through fluorescence) relate to ATP production?

## **B.6. Complementary Solvation Environment Studies**

### **B.6.1. 2D-IR**

If successful, the first part of the study would shed light on the preferred binding site(s) of C-peptide-Zn (II) to HSA. The binding site(s) could possibly lead to a conformational change that induces an increased amount of released ATP. With this newfound information, the domain with either the most binding sites or the binding site crucial to ATP release can be isolated to study the solvent environment upon ligand binding as the hydration of proteins is necessary for proper function. Here, the non-natural amino acid azidohomoalanine (Aha) can be used as a probe and can be incorporated directly into the protein using the Met auxotrophic mutants strategy.<sup>34,35</sup> Although isotope labelling ( $^{13}\text{C}^{18}\text{O}$ ) is used widely throughout the literature,<sup>36,37</sup> it is limited when considering large proteins. The amide I vibrations of the isotope labels are expected  $\sim 1,600\text{ cm}^{-1}$  and can be hindered by some amino acid side chain vibrations.<sup>34</sup> Small peptides can be designed to reduce this interference where large proteins depend on these amino acids for proper

folding. The Aha label has an azido group that absorbs around  $2,100\text{ cm}^{-1}$ , where shifts in this frequency can be informative of the local solvent environment. The Aha label will be present near the binding site and CD will be used to ensure the presence of the label itself doesn't hinder the HSA domain's structure and stability.

In the literature, 2D-IR of the Aha labelled PDZ2 domain from human tyrosine-phosphatase 1E has been explored with the binding of a peptide and mutant peptide. This is shown in Figure B.5. The mutant peptide has an apolar azobenzene moiety attached to it. From the data, the frequency shifts in the Aha label were found to reproducibly be  $\sim 1\text{ cm}^{-1}$ . It is noted that the shift in the azido frequency is often a measure of solvation. If the frequency is red shifted (as it is for the example in Figure B.5 with the presence of both peptides), the label is less solvated. In this case, the mutated peptide is the most red shifted, this could be due to the shielding provided by the hydrophobic azobenzene moiety.<sup>38</sup> In the case of a blue shift, there would be more solvation. If a protein is being unfolded, there would be such a blue shift as there is more flexibility within the protein that could increase the number of hydrogen bonds between water molecules.

For these experiments, the HSA domain, HSA domain + Zn (II), HSA domain + C-peptide, and HSA domain + C-peptide-Zn (II) would be analyzed. If there was a decrease in  $\alpha$ -helical character (and subsequent increase in random coils) found from CD experiments, I would then expect to see a blue shifted peak doing similar experiments due to the more unfolded nature of the protein. These experiments can then be done with other domains that were involved in peptide binding in the presence of Zn (II).

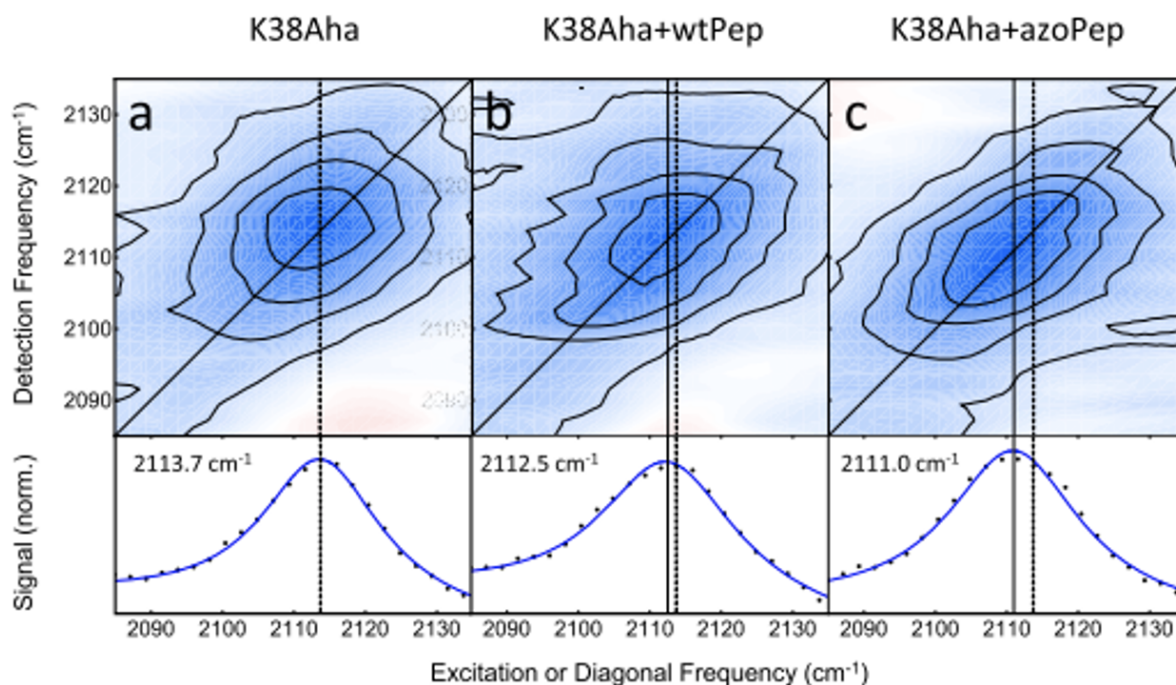


Figure B.5. The above figure shows the 2D-IR spectra of the K38Aha labeled PDZ2 domain (a) without ligand binding, (b) with binding to peptide RWAKSEAKENEQVSAV, and (c) with binding to the peptide mentioned in (b) mutated with an apolar azobenzene moiety.<sup>38</sup>

### B.6.2. Molecular Dynamics Simulations

MD simulations have often been used in conjunction with 2D-IR to provide physical insight from resulting spectra.<sup>39,40</sup> In the example mentioned in the preceding section, MD simulations further showed the reduced number of solvent contacts to the Aha label once the ligand was bound to the protein. The simulation was shown as a probability distribution in which the number of water contacts were replaced by ligand contacts once binding of the peptide occurred.<sup>38</sup> Hence, the MD simulation provided further evidence that corroborated the data presented in Figure B.5 and is necessary as 2D-IR spectra can often be difficult to interpret.

## B.7. Summary and Conclusion

The approach mentioned above utilizes X-ray crystallography to elucidate the binding sites associated with C-peptide and Zn (II) binding to the HSA protein. Site-directed mutagenesis can then be done to determine whether a particular binding site is crucial to ATP production (luciferase assay). Changes to secondary structure due to the mutations are also explored using tryptophan fluorescence spectroscopy and circular dichroism. These changes to secondary structure will also be compared to the amount of ATP released by erythrocytes as conformational changes can be necessary for protein function. Lastly, the solvent environment of the HSA domain with the most binding sites or most crucial binding site can be labeled to complement the results from the fluorescence and CD experiments.

Although the approach described here is for HSA interacting with C-peptide and Zn (II), many other proteins, peptides, and cations can be studied in this manner. Future studies could include assessing the binding of new drugs to the albumin protein as it is an abundant, negatively charged plasma protein with a large and reversible binding capability that can transport drugs throughout the body.<sup>41</sup>

### References for Appendix A

- (1) Morita, A., *Theory of Sum Frequency Generation Spectroscopy*; Springer: 2018; Vol. 35.

### References for Appendix B

- (1) Ganie, M. A.; Kotwal, S. Recent advances in management of diabetes mellitus. *J. Int. Med. Sci. Acad.* **2012**, *25*, 171–175.
- (2) Yaribeygi, H.; Maleki, M.; Sathyapalan, T.; Sahebkar, A. The effect of C-peptide on diabetic nephropathy: A review of molecular mechanisms. *Life Sci.* **2019**, *237*, 116950.
- (3) Kennedy, J. M.; Zochodne, D. W. Impaired peripheral nerve regeneration in diabetes mellitus. *J. Peripher. Nerv. Syst.* **2005**, *10*, 144–157.
- (4) Sowers, J. R.; Epstein, M.; Frohlich, E. D. Diabetes, hypertension, and cardiovascular disease: an update. *Hypertension* **2001**, *37*, 1053–1059.
- (5) Effects of Medical Therapies on Retinopathy Progression in Type 2 Diabetes. *New England Journal of Medicine* **2010**, *363*, 233–244.
- (6) Bhatt, M. P.; Lim, Y.-C.; Ha, K.-S. C-peptide replacement therapy as an emerging strategy for preventing diabetic vasculopathy. *Cardiovasc. Res.* **2014**, *104*, 234–244.
- (7) Marques, R. G.; Fontaine, M. J.; Rogers, J. C-Peptide: Much More Than a Byproduct of Insulin Biosynthesis. *Pancreas* **2004**, *29*, 231–238.
- (8) Wahren, J.; Kallas, A.; Sima, A. A. F. The Clinical Potential of C-Peptide Replacement in Type 1 Diabetes. *Diabetes* **2012**, *61*, 761–772.
- (9) Forst, T.; Hach, T.; Kunt, T.; Weber, M. M.; Pfützner, A. Molecular effects of C-Peptide in microvascular blood flow regulation. *Rev. Diabet. Stud.* **2009**, *6*, 159–167.



- (10) Kuzuya, H.; Blix, P. M.; Horwitz, D. L.; Steiner, D. F.; Rubenstein, A. H. Determination of Free and Total Insulin and C-Peptide in Insulin-treated Diabetics. *Diabetes* **1977**, *26*, 22–29.
- (11) Hills, C. E.; Brunskill, N. J.; Squires, P. E. C-Peptide as a Therapeutic Tool in Diabetic Nephropathy. *Am. J. Nephrol.* **2010**, *31*, 389–397.
- (12) Wahren, J.; Larsson, C. C-peptide: New findings and therapeutic possibilities. *Diabetes Res. Clin. Pract.* **2015**, *107*, 309–319.
- (13) Kitamura, T.; Kimura, K.; Makondo, K.; Furuya, D. T.; Suzuki, M.; Yoshida, T.; Saito, M. Proinsulin C-peptide increases nitric oxide production by enhancing mitogen-activated protein-kinase-dependent transcription of endothelial nitric oxide synthase in aortic endothelial cells of Wistar rats. *Diabetologia* **2003**, *46*, 1698–1705.
- (14) Medawala, W.; McCahill, P.; Giebink, A.; Meyer, J.; Ku, C.-J.; Spence, D. M. A Molecular Level Understanding of Zinc Activation of C-peptide and its Effects on Cellular Communication in the Bloodstream. *Rev. Diabet. Stud.* **2009**, *6*, 148–158.
- (15) Shpakov, A. O. Mechanisms of action and therapeutic potential of proinsulin C-peptide. *J. Evol. Biochem. Phys.* **2017**, *53*, 180–190.
- (16) Liu, Y.; Chen, C.; Summers, S.; Medawala, W.; Spence, D. M. C-peptide and zinc delivery to erythrocytes requires the presence of albumin: implications in diabetes explored with a 3D-printed fluidic device. *Integr. Biol.* **2015**, *7*, 534–543.
- (17) Geiger, M.; Janes, T.; Keshavarz, H.; Summers, S.; Pinger, C.; Fletcher, D.; Zinn, K.; Tennakoon, M.; Karunarathne, A.; Spence, D. A C-peptide complex with albumin

- and  $\text{Zn}^{2+}$  increases measurable GLUT1 levels in membranes of human red blood cells. *Sci. Rep.* **2020**, *10*, 17493.
- (18) Keltner, Z.; Meyer, J. A.; Johnson, E. M.; Palumbo, A. M.; Spence, D. M.; Reid, G. E. Mass spectrometric characterization and activity of zinc-activated proinsulin C-peptide and C-peptide mutants. *Analyst* **2010**, *135*, 278–288.
- (19) Maveyraud, L.; Mourey, L. Protein X-ray Crystallography and Drug Discovery. *Molecules* **2020**, *25*, 1030.
- (20) Sugio, S.; Kashima, A.; Mochizuki, S.; Noda, M.; Kobayashi, K. Crystal structure of human serum albumin at 2.5 Å resolution. *Protein Eng. Des. Sel.* **1999**, *12*, 439–446.
- (21) Zsila, F. Subdomain IB Is the Third Major Drug Binding Region of Human Serum Albumin: Toward the Three-Sites Model. *Mol. Pharmaceutics* **2013**, *10*, 1668–1682.
- (22) Ferraro, G.; Massai, L.; Messori, L.; Merlino, A. Cisplatin binding to human serum albumin: a structural study. *Chem. Commun.* **2015**, *51*, 9436–9439.
- (23) Siemiarczuk, A.; Petersen, C. E.; Ha, C.-E.; Yang, J.; Bhagavan, N. V. Analysis of Tryptophan Fluorescence Lifetimes in a Series of Human Serum Albumin Mutants with Substitutions in Subdomain 2A. *Cell Biochem. Biophys.* **2004**, *40*, 115–122.
- (24) Abou-Zied, O. K.; Al-Lawatia, N. Exploring the drug-binding site Sudlow I of human serum albumin: the role of water and Trp214 in molecular recognition and ligand binding. *Chem. Phys. Chem.* **2011**, *12*, 270–274.

- (25) Tarushi, A.; Raptopoulou, C. P.; Psycharis, V.; Terzis, A.; Psomas, G.; Kessissoglou, D. P. Zinc (II) complexes of the second-generation quinolone antibacterial drug enrofloxacin: Structure and DNA or albumin interaction. *Bioorg. Med. Chem.* **2010**, *18*, 2678–2685.
- (26) Thumser, A. E. A.; Buckland, A. G.; Wilton, D. C. Monoacylglycerol binding to human serum albumin: Evidence that monooleoylglycerol binds at the dansylsarcosine site. *J. Lipid Res.* **1998**, *39*, 1033–1038.
- (27) Cheng, W.; Ma, J.; Wang, S.; Lou, R.; Wu, S.; He, J.; Kang, H.; Liu, L.; Xiao, F. Interaction mechanism between resveratrol and ovalbumin based on fluorescence spectroscopy and molecular dynamic simulation. *LWT* **2021**, *146*, 111455.
- (28) Mirdha, L.; Chakraborty, H. Characterization of structural conformers of  $\kappa$ -casein utilizing fluorescence spectroscopy. *Int. J. Biol. Macromol.* **2019**, *131*, 89–96.
- (29) Chen, Y.-C.; Wang, H.-M.; Niu, Q.-X.; Ye, D.-Y.; Liang, G.-W. Binding between Saikosaponin C and Human Serum Albumin by Fluorescence Spectroscopy and Molecular Docking. *Molecules* **2016**, *21*, 153.
- (30) Usoltsev, D.; Sitnikova, V.; Kajava, A.; Uspenskaya, M. Systematic FTIR Spectroscopy Study of the Secondary Structure Changes in Human Serum Albumin under Various Denaturation Conditions. *Biomolecules* **2019**, *9*, DOI: 10.3390/biom9080359.
- (31) Matei, I.; Hillebrand, M. Interaction of kaempferol with human serum albumin: A fluorescence and circular dichroism study. *J. Pharm. Biomed.* **2010**, *51*, 768–773.
- (32) Lundin, A. Use of firefly luciferase in ATP-Related Assays of Biomass, Enzymes, and Metabolites. *Methods Enzymol.* **2000**, *305*, 346–370.

- (33) Lockwood, S. Y.; Erkal, J. L.; Spence, D. M. Endothelium-derived nitric oxide production is increased by ATP released from red blood cells incubated with hydroxyurea. *Nitric Oxide* **2014**, *38*, 1–7.
- (34) Bloem, R.; Koziol, K.; Waldauer, S. A.; Buchli, B.; Walser, R.; Samatanga, B.; Jelesarov, I.; Hamm, P. Ligand Binding Studied by 2D IR Spectroscopy Using the Azidohomoalanine Label. *J. Phys. Chem. B* **2012**, *116*, 13705–13712.
- (35) Taskent-Sezgin, H.; Chung, J.; Banerjee, P. S.; Nagarajan, S.; Dyer, R. B.; Carrico, I.; Raleigh, D. P. Azidohomoalanine: A Conformationally Sensitive IR Probe of Protein Folding, Protein Structure, and Electrostatics. *Angew. Chem.* **2010**, *122*, 7635–7637.
- (36) Middleton, C. T.; Woys, A. M.; Mukherjee, S. S.; Zanni, M. T. Residue-specific structural kinetics of proteins through the union of isotope labeling, mid-IR pulse shaping, and coherent 2D IR spectroscopy. *Methods* **2010**, *52*, 12–22.
- (37) Smith, A. W.; Lessing, J.; Ganim, Z.; Peng, C. S.; Tokmakoff, A.; Roy, S.; Jansen, T. L. C.; Knoester, J. Melting of a  $\beta$ -Hairpin Peptide Using Isotope-Edited 2D IR Spectroscopy and Simulations. *J. Phys. Chem. B* **2010**, *114*, 10913–10924.
- (38) Zanobini, C.; Bozovic, O.; Jankovic, B.; Koziol, K. L.; Johnson, P. J. M.; Hamm, P.; Gulzar, A.; Wolf, S.; Stock, G. Azidohomoalanine: A Minimally Invasive, Versatile, and Sensitive Infrared Label in Proteins To Study Ligand Binding. *J. Phys. Chem. B* **2018**, *122*, 10118–10125.
- (39) Kim, Y. S.; Hochstrasser, R. M. Applications of 2D IR Spectroscopy to Peptides, Proteins, and Hydrogen-Bond Dynamics. *J. Phys. Chem. B* **2009**, *113*, 8231–8251.

- (40) Lee, M. W.; Carr, J. K.; Göllner, M.; Hamm, P.; Meuwly, M. 2D IR spectra of cyanide in water investigated by molecular dynamics simulations. *J. Chem. Phys.* **2013**, *139*, 054506.
- (41) Kratz, F. A clinical update of using albumin as a drug vehicle — A commentary. *J. Control. Release* **2014**, *190*, 331–336.

# NAOMI DALCHAND

6118 N. Winthrop Ave., Apt. 2E, Chicago, IL, 60660

Telephone: (347) 445-2954 ◊ naomidalchand2021@u.northwestern.edu

## EDUCATION

---

### Northwestern University

*Evanston, IL*

Ph.D. Candidate, Chemistry

*July 2021*

Thesis: Probing the Hydrogen-Bonding Network at Soft matter and Metal/Metal:Oxide Interfaces Using Nonlinear Spectroscopy

### Barnard College

*New York, NY*

B.A. Biochemistry (ACS-Certified, Honors)

*May 2016*

Senior Honors Thesis: Electrochemical Activity of Variant Cytochrome  $c_{522}$  from *Collinia psychrerythraea*

## RESEARCH EXPERIENCE

---

### Northwestern University

2016 – Present

*Advisor: Prof. Franz M. Geiger*

*Evanston, IL*

- Advanced fundamental understanding of biocidal processes and compounds with applications in surface coatings and pharmaceutical development using nonlinear optical spectroscopy.
- Led collaboration with the Center for Sustainable Nanotechnology (CSN) to understand and aid in the development of more sustainable nanomaterials by studying coating material, i.e., polycations.
- Elucidated the structure of interfacial water over novel energy conversion devices through imaging and spectroscopic techniques to inform on the mechanism underlying electrical current production.
- Progressed my writing and communication skills through a science writing course at the Medill School of Journalism and through editing theses, manuscripts, and grant proposals for the lab.
- **Knowledgeable on the following techniques:** Contact Angle Goniometry, Optical Microscopy, Raman Microscopy, Scanning Electron Microscopy (SEM), Fourier-Transform Infrared Spectroscopy (FTIR), and Vibrational Spectroscopy.

### Barnard College

2014 – 2016

*Advisors: Prof. John S. Magyar and Prof. Marisa C. Buzzeo*

*New York, NY*

Established a project that interfaced both physical and bioinorganic chemistry and became the only co-advised student in the department Initiated studies that focused on analyzing the physiology of a critical hydrocarbon-degrading microorganism that aided in the clean-up of the 2010 Deepwater Horizon oil spill.

## LEADERSHIP

---

- **Northwestern University Building on Diversity (NU BonD)** 2019 – Present  
*Board Member*
  - Constructed an inclusive community within the Northwestern Dept. of Chemistry by creating events/safe spaces to discuss literature, research, and current events pertaining to racial/gender biases and inequalities in higher educations.
  - Developed a travel grant in order to support underrepresented minorities in presenting their research at conferences.

**Center for Integration of Research, Teaching, and Learning (CIRTL)** 2019 – 2020

*MOOC-Centered Learning Community (MCLC) Peer Facilitator*

- Led weekly discussions for 10 graduate students enrolled in an online course about educational ideologies and useful teaching practices within STEM fields.
- Created worksheets, activities, and discussion topics that focused on relevant topics such as active learning, student motivations, and inclusivity in undergraduate classrooms.

**Center for Sustainable Nanotechnology (CSN)** 2018 – 2019

*Professional Development Committee Chair*

- Spearheaded monthly virtual meetings with 6 committee members from different institutions across the U.S. to promote community and collaboration among peers interested in becoming better mentors and technical writers.
- Designed webinar presentation content with speakers to ensure each addressed scientifically and professional relevant subject matter.

## ACTIVITIES AND SERVICE

---

**Mentorship Opportunities for Research Engagement (MORE)** 2019 – 2020

*Volunteer*

- Mentored high school students in biweekly one-on-one advising sessions for the design and implementation of their science research projects.
- Taught mentees in experimental techniques and skills useful to both biology and chemistry such as UV-visible spectroscopy, buffer calibration, and data analysis.

**Museum of Science and Engineering**

2019 – 2020

*Black Creativity Showcase Volunteer*

- Demonstrated and explained chemistry experiments to ~200 underrepresented middle and high school students to inspire underrepresented minorities to get involved in STEM.
- Planned 4 Northwestern graduate student demonstrations including one that assessed the effect of particle size (surface area) on the rate of a reaction using water and Alka-Seltzer tablets.

**Barnard College**

2014 and 2016

*Higher Education Opportunities Programs (HEOP) Summer Session*

- Led weekly review session for ~20 prospective undergraduate students to prepare them for upcoming exams.
- Coached students on study strategies, time management, and research opportunities available at Barnard.

**SELECTED PUBLICATIONS**

---

*6 publications (2 as first author) | 94 citations | h-index: 5 | Google Scholar: Naomi Dalchand*

1. "Electrostatics, Hydrogen Bonding, and Molecular Structure at Polycation and Peptide: Lipid Membrane Interfaces," **Dalchand, N.**; Cui, Q.; Geiger, F. M., *ACS Appl. Mater. Interfaces* **2019**, *12*, 21149–21158.
2. "Perturbation of Hydrogen-Bonded Networks over Supported Lipid Bilayers by Poly (allylamine hydrochloride)," **Dalchand, N.**; Doğangün, M.; Ohno, P.E.; Ma, E.; Martinson, A. B.; Geiger, F. M., *J. Phys. Chem. B* **2019**, *123*, 4251–4257.
3. "Interfacial electrostatics of poly (vinylamine hydrochloride), poly (diallyldimethylammonium chloride), poly-1-lysine, and poly-1-arginine interacting with lipid bilayers," McGeachy, A.; **Dalchand, N.**; Caudill, E.; Li, T.; Doğangün, M.; Olenick, L. L.; Chang, H.; Pederson, J.; Geiger, F. M., *Phys. Chem. Chem. Phys.* **2018**, *20*, 10846–10856.

**SELECTED PRESENTATIONS**

---

1. **Dalchand, N.**; Cui, Q.; Geiger, F. M., "Charge and Structure Quantification of Peptides at Aqueous Interfaces," 258<sup>th</sup> American Chemical Society National Meeting, San Diego, CA, August 2019, oral.



2. Li, T.; **Dalchand, N.**; Dođangün, M.; McGeachy, A. C.; Olenick, L. L.; Geiger, F. M., "Lipid Bilayers Responses to Critical Polycation Concentrations by Vibrational Sum Frequency Generation Spectroscopy," 45<sup>th</sup> NOBCCChE National Conferences, Orlando, FL, September 2018, oral.
3. **Dalchand, N.**; Montero, K.; Salerno, S.; Buzzeo, M. C.; Magyar, J. S.; "Essential cation-*pi* interaction in a psychrophilic electron transfer protein," 251<sup>th</sup> American Chemical Society National Meeting, San Diego, CA, March 2016, poster.

## AWARDS AND RECOGNITIONS

---

NOBCCChE Advancing Science Conference Grant (2018)

NSF Graduate Research Fellowship Program (2018)

L. Carroll King Award for Excellence in 100-Level Teaching (2017)

Excellence in Research Award (2016)

Travel Award Recipient for the ACS Division of Inorganic Chemistry (2015)

Junior Marshall for the Barnard College and Columbia University Commencement (2015)